FRACTURE CLOSURE STRESS EFFECTS ON MULTI-PHASE FLOW AND PRODUCTION IN HYDRAULICALLY-FRACTURED SHALE OIL WELLS

A Thesis

by

MATTHEW KELLY

Submitted to the Office of Graduate and Professional Studies of
Texas A&M University
in partial fulfillment of the requirements for the degree of

MASTER OF SCIENCE

Chair of Committee,	I. Yucel Akkutlu
Committee Members,	Thomas A. Blasingame
	Mukul Bhatia
Head of Department,	Jeff Spath

August 2022

Major Subject: Petroleum Engineering

ABSTRACT

Gas and oil production performance in shale oil wells is fundamentally different from the conventional reservoirs. The difference is more pronounced in the producing gas-oil-ratio (GOR) trends. In the conventional case, when flow occurs in a permeable reservoir and in radial geometry, the GOR is a function of average reservoir pressure: when the pore pressure is high enough, the produced GOR stays constant and equal to the solution gas-oil ratio of the reservoir oil; when the pressure in the system is reduced below the bubble point pressure of the reservoir oil, gas phase appears in the reservoir and causes increase in gas saturation. Increase in the gas saturation beyond critical gas saturation leads to flow of gas and, hence, an increase in the producing GOR. A well with fracture, on the other hand, experiences a different transient flow behavior. In horizontal shale wells with multi-stage hydraulic fractures, in particular due to ultra-low permeability of the rock matrix, the dynamic GOR behavior will have an extended time. Further some of the producing shale oil wells have GOR remaining flat, regardless of rate of the depletion. Although the literature has already attributed the peculiar GOR trends of the unconventional oil wells to several factors, it is still an unclear area with further debate. In this thesis I considered single-well production – in the absence of neighboring well interference-and analyze the effects of stresses on the flow and production. Using reservoir flow simulation modeling approach, I show that the permeability reduction caused by hydraulic fracture closure and pore volume change due to stresses reduce the gas saturation inside the fracture and in the matrix near the fractures, hence, producing GOR stays relatively low. The higher the fracture closure and the pore compressibility, the lower the gas saturation, and lower the gas released to the wellbore. Flow, on the other hand, becomes stress-sensitive because of the stress-dependency of the permeability field. As the reservoir is depleted,

the reservoir experiences larger effective stress, which, in turn, reduces the permeability of the matrix and the permeability of the fractures. Because the in-situ stresses could be anisotropic, I also investigated the impact of stress anisotropy on the producing GOR.

The more dependent the permeability is on the stress of the system, the flatter the GOR curve is. When hydraulic fractures are considered to be initially at infinite-conductivity flow, then pore compressibility in the matrix is the reason for GOR flatness, but if the flow is controlled by the finite-conductivity of the fractures, then the reduction in the fracture's permeability caused by effective stress is the reason for GOR flatness. When the matrix permeability is in the micro-Darcy range, the stress effect on the permeability leads to a lower GOR. The stress anisotropic study showed that the difference in the overburden stress and the minimum horizontal stress did not have a large impact on the GOR. The stress anisotropy study did find that the stress dependency in the hydraulic fractures contributes more to the GOR trend than the stress dependency in the matrix. The stress effects on the shale oil reservoir systems can have large implications on the drawdown strategies for the operators.

DEDICATION

To my mother, who has pushed and supported me for my entire life, and without her, I would not be where I am today.

ACKNOWLEDGEMENTS

I want to give a tremendous amount of thanks to Dr. Akkutlu, for carrying me on his back throughout this degree

I want to give thanks to Dr. Mike King and Ching-Hsien Liu for their help during the development of the Eclipse model.

Special thanks to Ivan Aldana for his help on working with the NaSh simulation model.

I want to give my gratitude towards Dr. Edward Lee, and Dr. Abigail Songok for allowing me to be a chemistry teaching-assistant.

CONTRIBUTORS AND FUNDING SOURCES

Contributors

This work was supported by a thesis committee consisting of Professor I. Yucel Akkutlu and Thomas A. Blasingame of the Department of Petroleum Engineering and Professor Mukul Bhatia of the Department of Geology.

Funding Sources

This thesis was funded by the Chevron fellowship, and by the Graduate Teaching assistantship in the Chemistry Department at Texas A&M University.

NOMENCLATURE

GOR	Gas oil ratio of the production fluid, MSCF/STB
P_{wf}	Flowing bottom hole pressure
P_i	Initial reservoir pore pressure
S_{gc}	Minimum amount of gas saturation needed for movement
P_b	Bubble point pressure of the reservoir oil, psi
BHP	Flowing bottom hole pressure
P_{ave}	Average reservoir pore pressure
Cp	Coefficient of isothermal pore compressibility
V_p	Pore volume
k	Matrix permeability
k_o	Matrix permeability at zero effective stress
p_{conf}	The confinement pressure
p	Pore pressure
P_1	Effective stress at zero matrix permeability
m	Strength of the pore to hold the aperture
α	Biot's coefficient
k_{fo}	Hydraulic fracture permeability at zero effective stress
$\sigma_{h,min}$	Minimum horizontal stress
∏	Effective stress to close a propped fracture
d_p	Diameter of proppant
η	quality of proppant placement
$h_{0.Frac}$	initial pore height from the fracture-wall asperities at zero effective stress

E	Youngs modulus of the matrix
E_p	Young's modulus of the proppants
Er	Young's modulus of the hydraulic fracture walls
P_{Seal}	Pressure to seal a fracture with no proppants
M	Strength of the hydraulic fracture to hold the aperture when propped
η_A	quality of proppant placement in terms of areal placement
η_H	quality of proppant placement in terms of vertical placement
ζ	Shape factor determined by the proppants contribution to the fracture asperity
S_{wc}	critical water saturation, fraction
S_{oc}	Critical oil saturation, fraction
S_{gi}	Initial gas saturation, fraction
S_{wi}	Initial or connate water saturation, fraction
Soi	Initial oil saturation, S_{oi}
D	Darcy unit equal to 0.987 □m^2
F_{cD}	Dimensionless fracture conductivity
R_s	Solution GOR of the oil
σ_{ob}	Overburden stress
C_r	Compressibility of rock

TABLE OF CONTENTS

LIST OF FIGURES

LIST OF TABLES

1 . INTRODUCTION

1.1 Overview

Producing gas-oil ratio (GOR) of a well is the volume ratio of the produced oil and gas rates. Rates are measured in stock tank barrel per day for oil and standard cubic foot per day for gas. Forecasting the producing GOR is a fundamental part of understanding the petroleum production systems. It is important because the trends could affect the type of production equipment needed and it also could be a deciding factor during the economic analysis.

In conventional forecasting models, GOR is a function of the reservoir pressure. The pressure is the primary factor that controls the fluid properties in the reservoir. The oil properties that are influenced by the pressure are the oil density and formation volume factor, deviation factor of its gas from the ideal gas behavior, and the viscosity. These quantities are influenced significantly in particular when the pressure during the production drops down to the bubble point pressure of the oil and when a gas phase appears in the formation. Gas phase is less viscous and more compressible compared to the oil phase. During the depletion, as the reservoir pressure continues to go down, the gas saturation builds up and, when the critical gas saturation is reached, the gas flows. Consequently, a dramatic increase is observed in the producing GOR trends. Therefore, in the conventional reservoirs, the pressure depletion and gas evolution have characteristic signature: constant GOR at pressures above the bubble point pressure; followed by rapidly increasing GOR at lower reservoir pressure. In essence, the GOR trend is controlled by the ability of the oil to yield gas, more precisely by the thermodynamics of the reservoir oil: composition, pressure and temperature.

In unconventional wells, however this trend in GOR is not seen. Instead, the GOR remains low and constant for long periods of production time, even when the formation is depleted below

the bubble point pressure. Below the differences in GOR trends of the unconventional oil wells are discussed.

1.2 Literature on Shale Oil Wells GOR Trends

In the literature, there are several field studies on the unconventional oil well GOR trends. The most notable observation from different publications is that a much longer production time is observed when the producing GOR stays constant, and when it does start to increase, the increase is not as large an increase as in the conventional oil wells case. It seems that the hydraulic fractures as the new production system component controls the release of gas. This GOR trend is seen in the Bakken (Hough 2011), Eagle Ford (Tran 2011; Khoshghadam 2017), Woodford (Jones 2017), In **Figure 1**, a well is shown with a constant-GOR production period of 1 year.

Another observed trend is an increase in the producing GOR, which begins early and continues at a constant rate, **Figure 2**. Unlike the previous case, this time the well did not experience any controlled GOR behavior. The authors argue that the well has a dense hydraulic fracture network; consequently, the reservoir pressure between the fractures drops below the bubble point pressure and the critical gas saturation is reached relatively early.

In addition, it may be argued that the hydraulic fracture conductivity could vary and the fractures with lower conductivity would influence the time dependence of the GOR trend. Finally, interference of the neighboring wells could impact the production performance of the well such that GOR could be influenced in a complex fashion. Several wells are shown in **Figure 3**. Note that these wells have highly variable tubing head pressure, which also includes the effects of the

multi-phase wellbore flow. In **Figures 3a-3b** we observe constant GOR with small oscillations, in **Figure 3c** we observe a constant GOR with noise.

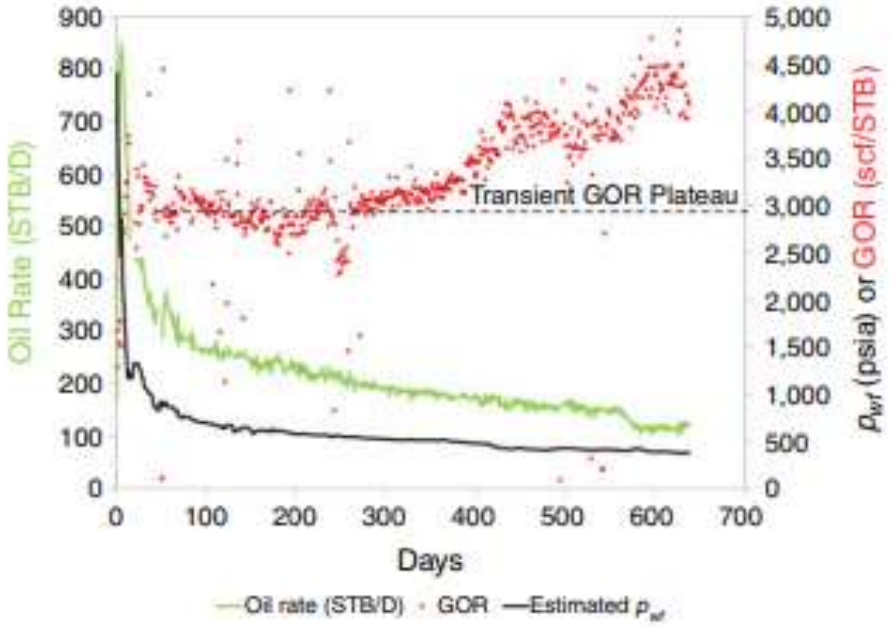

Figure 1. a Springer shale well. Reprinted from Jones Jr. 2017.

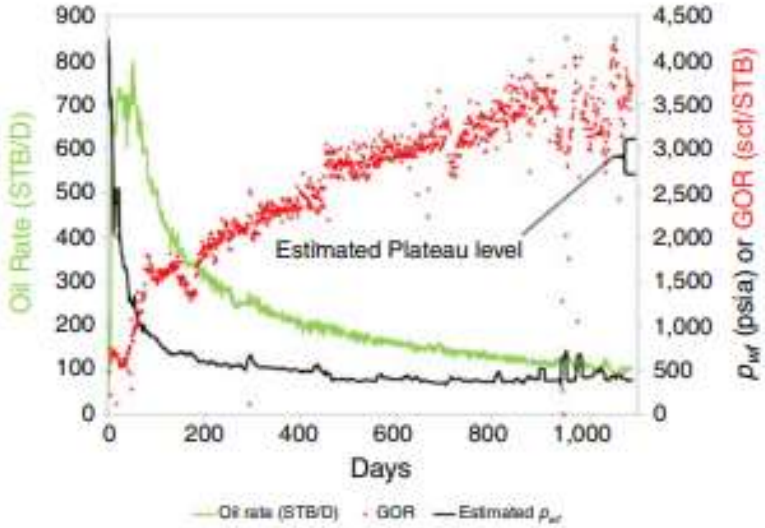

Figure 2. a Woodford well that doesn't have an extended period of time of flat GOR. Reprinted from Jones Jr. 2017.

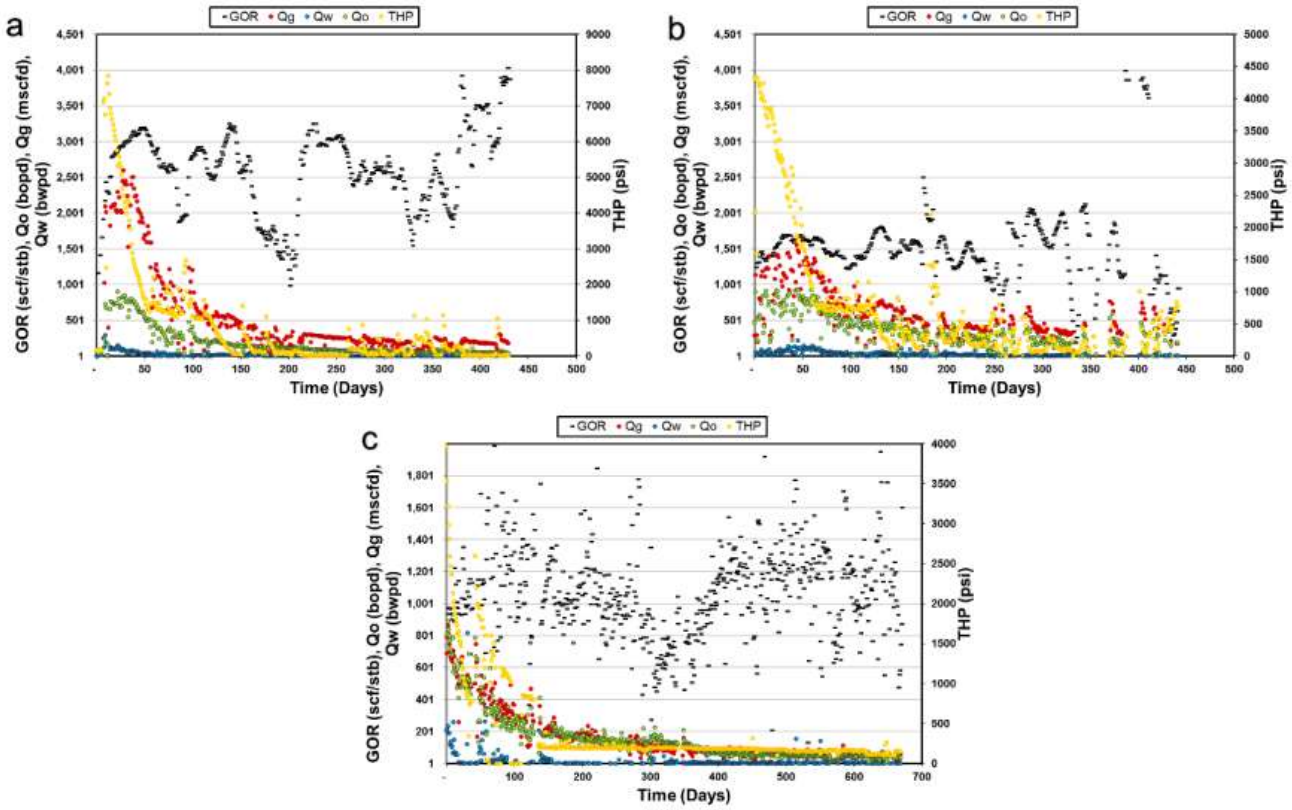

Figure 3. Three shale wells studied. Reprinted from Khoshghadam et al. 2017.

It is difficult to see clear trends with real production data due to the variability of the tubing head pressure, workovers, and the nature of the hydraulic fractures. Nevertheless, Jones (2017) has mapped out in **Figure 4**, several ideal GOR trends based on values of the bottom-hole flowing pressure (BHP or P_{wf}).

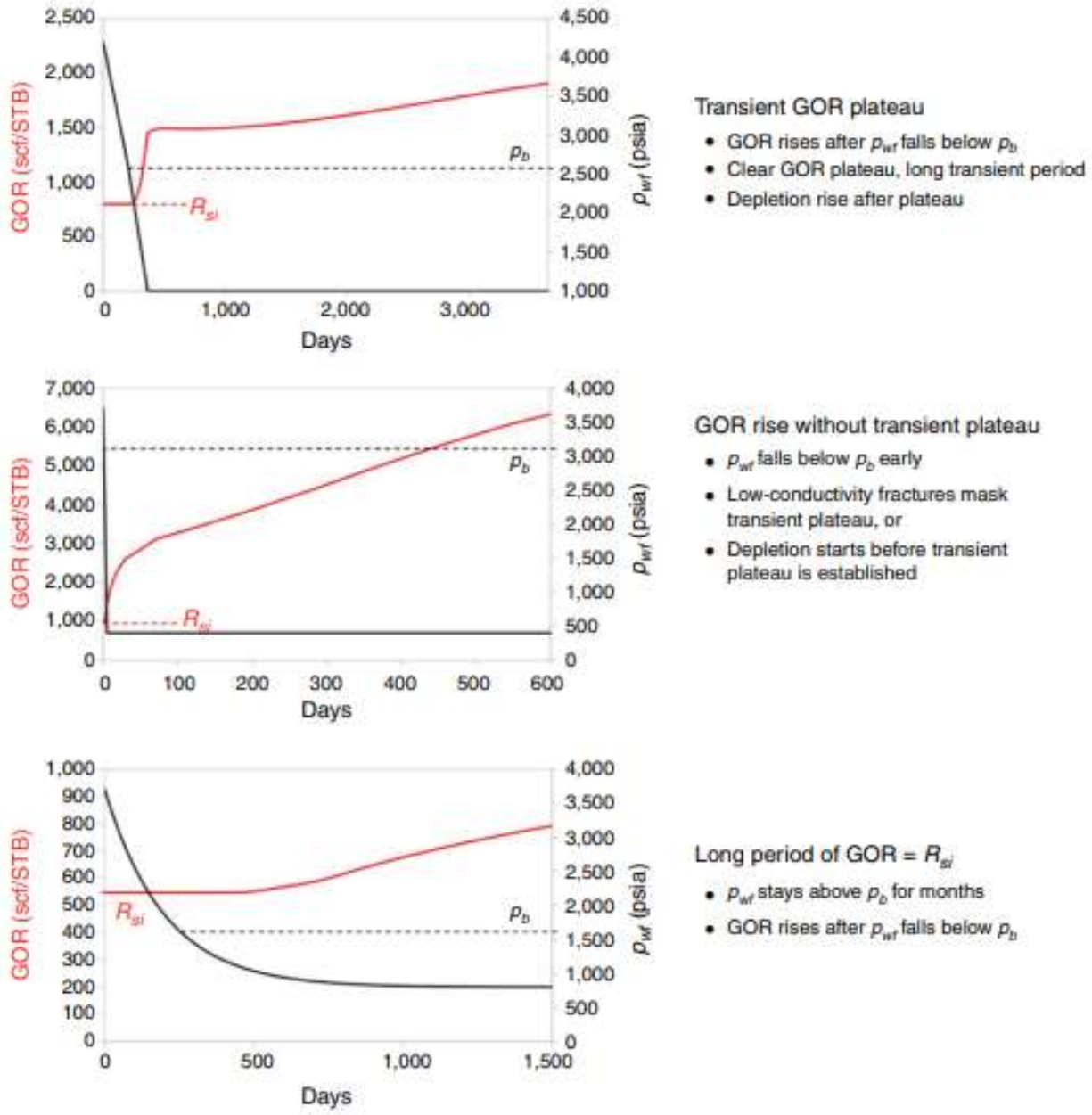

Figure 4. Ideal simulated models. Reprinted from Jones 2017.

In **Figure 4 (top)** the ideal shale oil well producing GOR trend is shown. The hydraulic fractures have developed production with negligible fracture interference. In essence each fracture tapping into its own oil in its own drainage volume. The production trend of this well could be

captured using a model with simple planar fracture. This is the trend that will be seen in most wells with sufficient hydraulic fracture separation. The value of the GOR is relatively constant. In **Figure 4 (middle)**, a trend develops caused by early pressure depletion to below bubble point pressure. In **Figure 4 (bottom)** shows a production scenario when the bottomhole pressure stays above the bubble point pressure for an extended time This may be due to hydraulic fracture behavior or due to an operation such as artificial lifting.

The literature contains discussion on several reasons why the producing GOR in unconventional reservoirs behaves in a constant manner under bubble point pressure. In Jones (2012), the author argues that GOR is influenced by the transient flow regime of a fractured horizontal well because linear flow compared to radial flow has a much higher GOR. The GOR is dependent on the P_{wf}, and when the P_i and the S_{gc} is higher, the lower the GOR value. Pradhan (2020) suggested that the GOR is affected by the nano-confinement effect in the matrix. The bubble point pressure of the oil in nanoporous shale is suppressed due to oil changing composition under nano-confinement Khoshghadam (2017), discussed how the matrix properties and fluid properties could affect the GOR, including the stress-dependent permeability effects on the GOR trend. Khoshghadam's model was changing the stress effect based on the pore size, while in my model I changed it based on if the cell is dominated by hydraulic fractures or not.

In unconventional models, the GOR is a function of the flowing bottom-hole pressure of the well P_{wf}, not the average reservoir pressure, and it is not solely affected by the fluid properties, but also the reservoir properties. The reservoir properties that affect the GOR include: fracture geometry, fracture length, the distance between fractures both from the same well and of different wells, the matrix pore size distribution, and the currently studied effects of rock compaction and stress-dependent permeability. The GOR is dependent on the flow regimes and ideal models have

been reflecting this (Jones Jr., 2017). According to Jones (2017), there are four stages that form the framework of GOR forecasting. These stages are shown in in **Figure 5** on a log-log diagnostic plot.

The first stage is when the producing GOR is equal to the initial solution gas-oil-ratio of the oil (R_{Soi}). Because P_{wf} is above the bubble point, the pressure in the matrix is high enough to maintain the oil as unsaturated oil. No gas is released in the matrix, consequently, the produced gas is equal to the initial solution gas. The second stage develops when P_{wf} drops below the bubble point, when the gas evolves and, when the gas phase in the matrix reaches to its critical gas saturation, the gas flows in the matrix. Typically the gas phase has higher mobility and, hence, its flow takes place at rates higher than the oil or water phases. Consequently, the GOR sharply increases. The third stage in **Figure 4** is flat GOR stage. The authors argue this behavior is associated with linear flow because the production trends have the characteristic ½ slope. In this thesis I will further delve into the reservoir physics that leads to this flat-GOR behavior further. Finally, the fourth stage develops with continuous rise in GOR. This increase in GOR is not bounded by the size of the drainage volume (in my case, the computational box of the simulation). Indeed, after the pressure transient reaches to the outer boundaries, the production reaches to the limits of the well's drainage volume. The size of this volume tells us the maximum amount of gas that can be produced. During the production, when this maximum amount is reached, GOR shows a peak followed by a rapid decline. I would call this late-time period the 5^{th} stage.

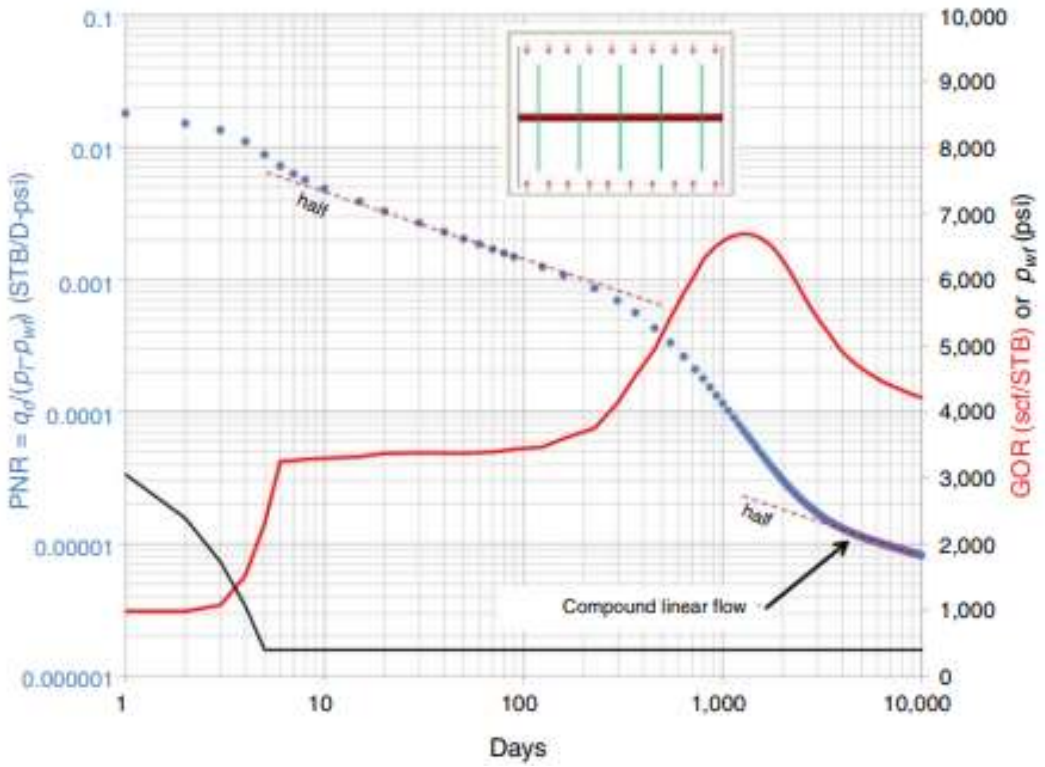

Figure 5. Unbounded unconventional reservoir with infinite conductivity fractures. Reprinted from Jones 2017.

It is important to note that the five stages with their signatures may not always develop for every unconventional well and additional factors could come in to play. It is, therefore, important to study these stages carefully and any other factor needs to be identified as part of the effort to understand the individual well performance.

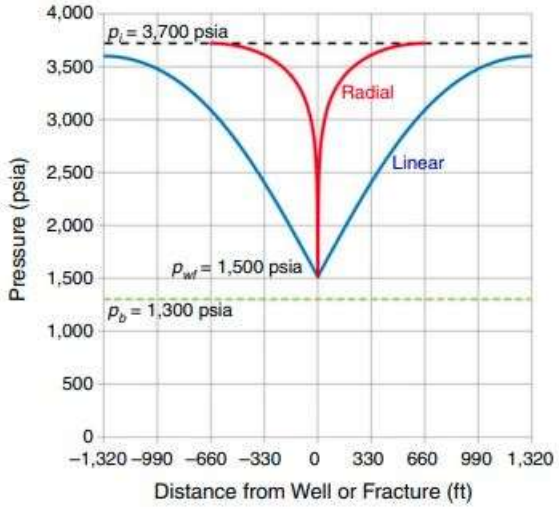

Figure 6. Pressure gradient of the same rock properties, differing only if it is Radial and Linear flow. Reprinted from Jones 2017

Earlier I argued that the producing GOR of an unconventional well is determined by the P_{wf}. Accordingly, the lower the P_{wf}, the higher the GOR level. Whitson and Sunjerga (2012) argued that magnitude of the initial reservoir pressure P_i could also have effect on the GOR. The higher the pressure above the bubble point a reservoir initially is, the lower the GOR. Conversely, the lower the P_{wf}, the higher the GOR. This deviates from conventional reservoirs, where the GOR is seen as a function of average pressure, and therefore when the matrix permeability becomes low enough there is a switch to GOR being a function of P_i minus P_{wf} (Whitson 2015). In essence, a large pressure gradient of linear flow near fracture has an added impact on the transport rate of the gas and hence GOR, which could be different from the much lower pressure gradient of radial flow near a conventional well (Jones 2017).

In **Figure 6**, two model pressure distributions of radial and linear flow are shown. In the case of radial flow regime, there is exponential gradient; whereas the linear flow case has a much stronger and wider gradient. This means that for the same production conditions, linear flow will

have a larger pressure drop that extends further. For the radial flow pressure gradient, changing the P_{wf} or the P_i will not dramatically change the pressure throughout the radius of investigation. In the linear flow model, the initial pressure and the P_{wf} are dominating this gradient, and that changing the either of them has a larger impact on the pressure throughout the reservoir than the radial flow case. If the P_{wf} is increased to 2,000 psi, the pressure at the 10 feet from the well will be increased by an entire 500 psi for the linear flow, but the increase will be much less than 500 for the radial flow. The transition from P_{wf} to P_i is much sharper in linear flow, forming a large constant zone of gas saturation that is the driving force of the GOR value.

The bubble point pressure is suppressed by the capillary pressure effects and mid-confined nanopores (Pradhan, 2020), (Khoshghadam, 2015). The nano-pores of shale lead to a nano-confinement effect that changes the fluid composition along with its PVT and in-situ transport properties. **Figure 7** shows a fluid phase envelop for multi-component oil that has gone through compositional adjustment and shift in critical point such that it is acting as a gas in nanopores.

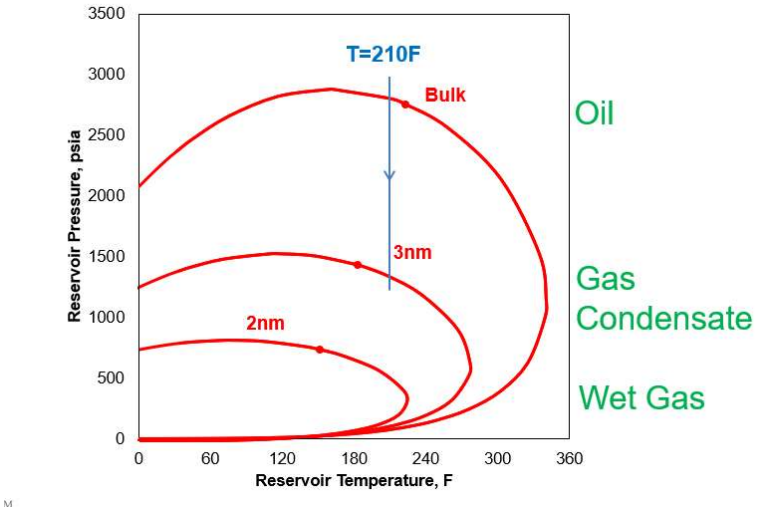

Figure 7. Pressure vs temperature, phase behavior with nano-confinement effects. Reprinted from Didar and Akkutlu (2013).

The nano-Darcy range permeability is the driving force of the GOR flatness, and stress dependency will lead to even more flatness, where the different pore sizes are affected differently from the stress. Rock compaction has a significant effect in the unconventional reservoirs because it affects the rock properties such as porosity and pore connectivity, pore pressure profile and gas saturation (Khoshghadam, 2015). Rock compaction has been documented to change the saturation in the reservoirs (Oppert and Carley 2021). In Oppert's study, it was a conventional reservoir in the Gulf of Mexico with high levels of compaction, where the compaction changed the water oil contact line. This effect of compaction re-arranging the fluid in the reservoir is important to reflect on. In Makinde's paper (2017), it was investigated if the rock compressibility had a major effect on the GOR, their range of compressibility investigated was $C_r = 2E^{-6}$ to $8E^{-6}$ 1/psi and did see that there was a small suppression of GOR when increased; however, Makinde (2017) concluded that it was not significant. Their study on compaction showed that compaction had a strong effect on suppressing GOR and increasing oil production.

1.3 Purpose of Study

The main goal of this study is to provide a greater understanding of the unconventional wells producing GOR. For the purpose I use a reservoir flow simulator and test all the potential parameters that could possibly affect the GOR. Usage of reservoir flow simulator is not a new approach to study shale GOR. Makinde (2017) used reservoir simulation to investigate the effect of drainage volume, and fluid properties on the GOR of horizontal production well with multi-stage fractures. In my study the parameters were studied individually, one parameter at a time, to help identify the largest contributors to the forecasting data. The parameters I investigated are the pore volume compressibility coefficient, stress dependency of the permeability of the matrix and

of the hydraulic fractures, the anisotropic stress field effects on permeability, and the dimensionless fracture conductivity. The simulation set up is included in Chapter 2, and the results are discussed in Chapter 3.

2. FLOW SIMULATION MODELS AND PROCEDURE

The data necessary for the investigation were collected using two reservoir flow simulation models: Eclipse 100 and NaSh. Eclipse was the model developed first and used for a large portion of the study; I used NaSh while I was investigating the fracture closure as a function of minimum horizontal stress, i.e., the effect of anisotropic stress field on the producing GOR. Eclipse is widely known and often used in the industry, whereas NaSh is an in-house compositional reservoir flow simulator with application into production from unconventional oil and gas reservoirs.

I have developed a three-dimensional oil reservoir model with the following dimensions: Length= 1,942.8 ft; Width=1,040 ft; Height= 98.4 ft. The model contains a horizontal well 1,016 ft long and located at the center of the model. The well connects to ten vertical fractures with uniform dimensions: Length=52 ft; Fracture spacing= 114.3 ft.

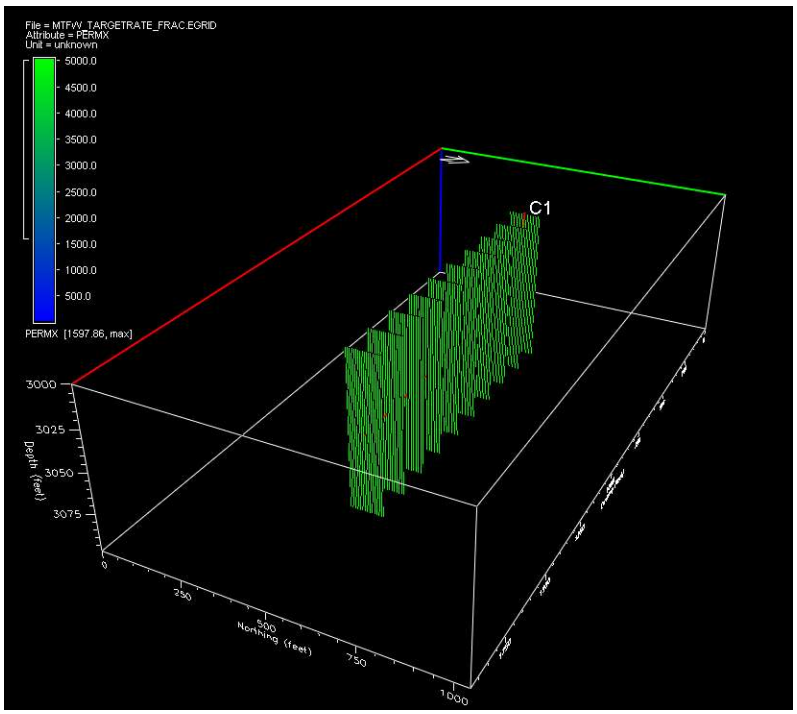

Figure 8. The reservoir, well, and the 10 hydraulic fractures. Top angle view

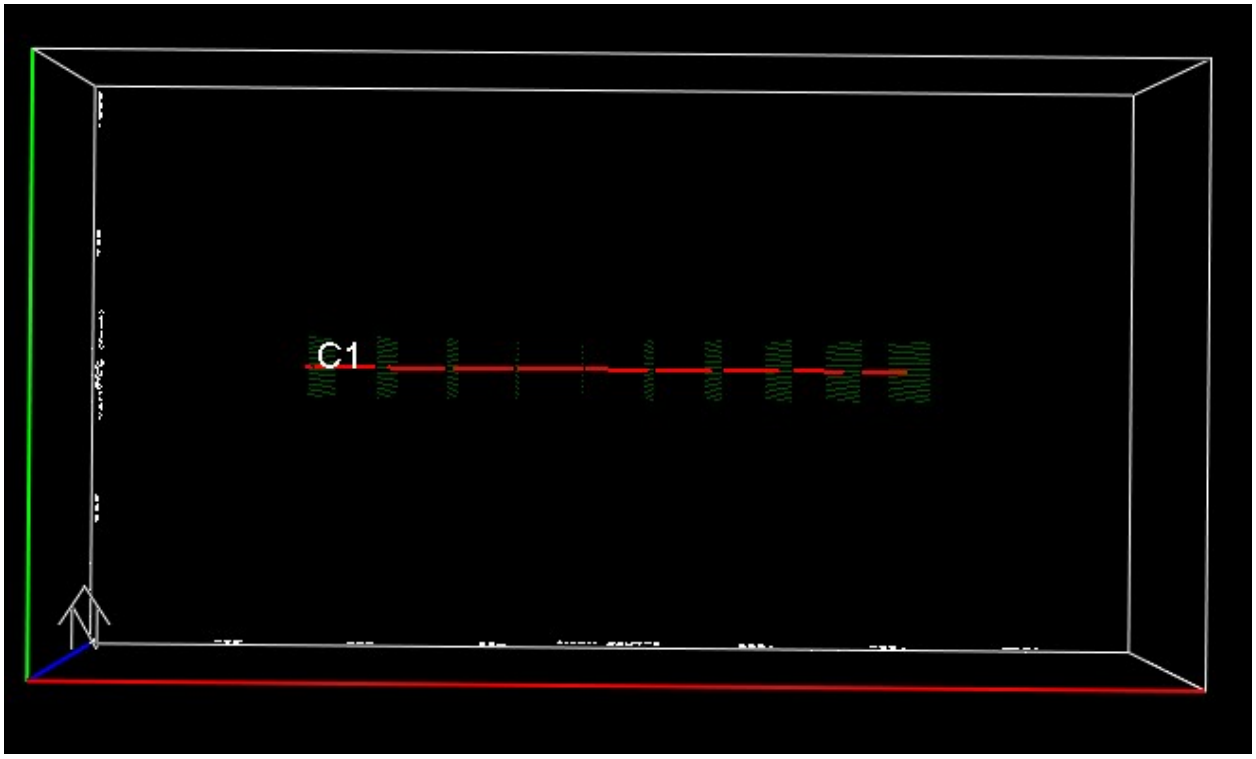

Figure 9. The reservoir, well, and the 10 hydraulic fractures. top down view

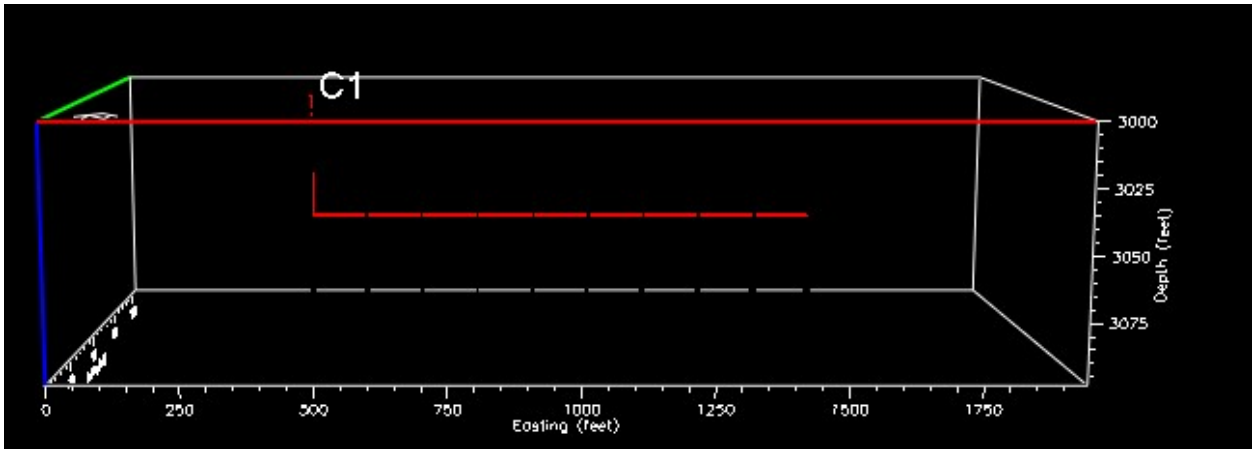

Figure 10. The reservoir, well, and the 10 hydraulic fractures. Side View

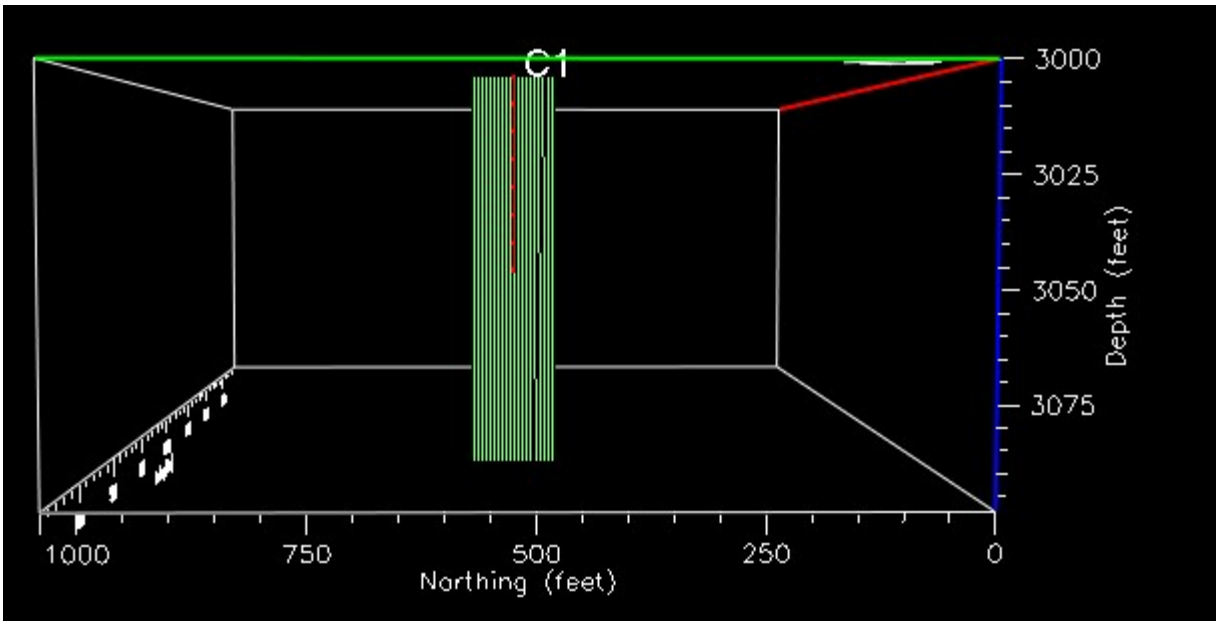

Figure 11. The reservoir, well, and the 10 hydraulic fractures. Front view

The simulation considers presence of oil, water in the formation initially. Gas phase appears during the production, and three-phase flow calculations are performed. Table 1 shows the initial saturations of the phases and their critical saturation values necessary for their flow. Notice that the initial gas saturation is at the critical gas saturation, which is indicating that, during the production at $P=P_b$ any release of gas bubbles from the oil phase is enough to make the gas a mobile phase. Consequently, we should observe a change in the produced GOR at the well head.

The porosity and permeability fields used in the Eclipse model considers single (unipore) porosity and permeability fields with the values of permeability significantly larger in the locations of the hydraulic fractures. In addition, I considered that both the porosity and permeability fields could change during the production as the pore pressure is reduced. The change in porosity is calculated using a constant coefficient of isothermal pore compressibility, c_p, whereas the permeability change uses another rule based on a mechanistic formulation developed by Gangi using the concept of bed of nails (Gangi, 1978). Although we used the same model for both fractures and the matrix, the values of the Gangi parameters are different for fractures because the

Table 1. Eclipse Model

Initial matrix porosity	0.12	
Initial fracture porosity	0.12	
Pore compressibility, c_p	1.00E-05	1/psi
Fracture compressibility, c_{pf}	1.00E-05	1/psi
S_{gi}	0.1	
S_{oi}	0.6	
Swi	0.3	
S_{gc}	0.1	
S_{wc}	0.1	
S_{oc}	0.1	
Initial matrix permeability, k	0.05	mD
Initial fracture permeability, k_f	5,000	mD

fractures are propped and have additional resistance to the closure stress. I will discuss the permeability changes as a function of stress below further.

NaSh simulation model, on the other hand, considers the same reservoir block, with the same well and fractures, but the fractures are introduced into the model as discrete features. Hence, I consider dual (matrix/fracture) porosity and permeability nature of the unconventional wells using the NaSh model. The petrophysical parameters and their values are the same as listed in **Table 1**.

The relativity permeability of a fluid phase is calculated with the three key parameters in Eclipse: SOF3, SWFN, and SGFN. The water relative permeability is a function purely of the water saturation in the computation cell, and the gas relative permeability is also a function purely of the gas saturation. The oil relative permeability is found by interpolating the oil-gas, and the oil-water relative permeability curves. The curves are tabulated below, where the values are linearly interpolated.

Table 2. Relative permeability of oil saturation curve data, for Keyword SOF3

Saturation of oil	relative permeability of oil, when there is only oil and water	relative permeability of oil, when there is only oil, gas, and connate water
0.1	0	0
0.8	1	1

Table 3. Relative permeability of water saturation curve data, for Keyword SWFN

Saturation of water	Relative permeability of water	water oil capillary pressure (psi)
0.1	0	2
0.8	1	0

Table 4. Relative permeability of gas saturation curve data, for Keyword SGFN

Saturation of gas	Relative permeability of gas	Oil gas capillary pressure (psi)
0.1	0	2
0.8	1	0

I would like to mention that flow during the simulations develops in two-dimensional (areal) fashion --even though our model is three-dimensional-- because no vertical flow is considered. This is common practice in unconventional reservoir engineering because the unconventional rocks such as shale is widely known as highly laminated mud rocks and this lamination allows development of the flow only along the bedding planes. Hence the vertical shale permeability is safely considered zero. The flow in fractures could be vertical due to the presence of multiple phases under the influence of the gravity, but during previous investigations in our group using NaSh, it was found that the vertical flow in fractures is not likely to change the nature of production rates significantly. In the fractures fluid flows linearly towards the well location.

2.1 Stress-dependent Pore Compressibility Considerations

Although a universal correlation does not exist, it is clear that rocks experience pore volume compressibility changes as a function of the stress, **Figure 12**. The stress applied in the laboratory conditions is typically the difference in confining pressure and pore pressure. When the two values are close to each other the effective stress is low, and as the difference builds up, the stress becomes larger. During production the difference builds up due to pore pressure decline.

It is also important to point out the pore compressibility could change as a function of stress. It may even change non-linearly. We observe this change for various unconventional rock samples, **Figure 13**. What seems to be the case, however, is that the compressibility changes significantly during the early production times when the effective stress near the fractures is still low, whereas the change is almost negligible at large stresses. The values measured in the laboratory are in the range 10^{-4} to 10^{-6} psi^{-1}. Using Barnett, Woodford, Haynesville, Eagle Ford and Wolf Camp samples, Bachir Mahomad (2014) measured in the laboratory pore compressibility values that vary from $1.8x10^{-4}$ down to 2.010^{-6} psi^{-1}. This highly compressible and stress-dependent behavior in the unconventional rocks during early production can be explained by the presence of micro-cracks in the formation (see **Figure 14**). The variability in pore compressibility could lead to change in pore volume and hence in pore-pressure and saturation fields near the hydraulic fractures.

During production, when the pore pressure is high, the cracks are open and interconnected; hence, they ready to deliver the fluids they store. When the pore pressure starts to decrease during initial production, when the production rates are high, the pore volume decreases at a fast rate. When the pore pressure has decreased a significant amount, later in production, the rate of closure slows down.

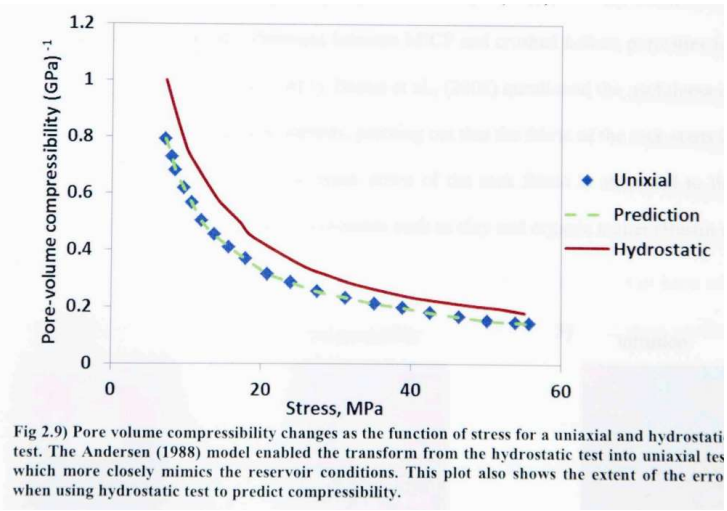

Fig 2.9) Pore volume compressibility changes as the function of stress for a uniaxial and hydrostati test. The Andersen (1988) model enabled the transform from the hydrostatic test into uniaxial tes which more closely mimics the reservoir conditions. This plot also shows the extent of the erro when using hydrostatic test to predict compressibility.

Figure 12. Pore volume compressibility as a function of stress. Reprinted from Anderson 1988

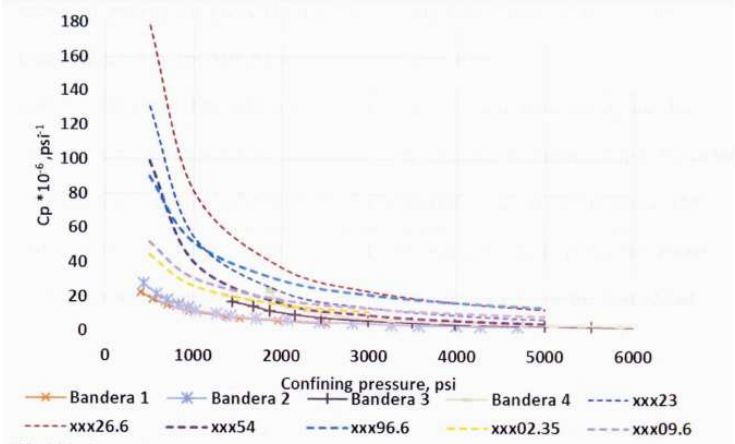

Fig 4.24: Comparison between MICP pore volume compressibility and published data on pore volume compressibility by Zimmerman (1984). The shale samples exhibit higher compressibility values compare to the published sandstones compressibility even at higher pressure where the difference is larger than 30 %

Figure 13. Left: Pore volume compressibility of various unconventional rocks as a function of the stress. Reprinted from Bachir Mahomad 2014.

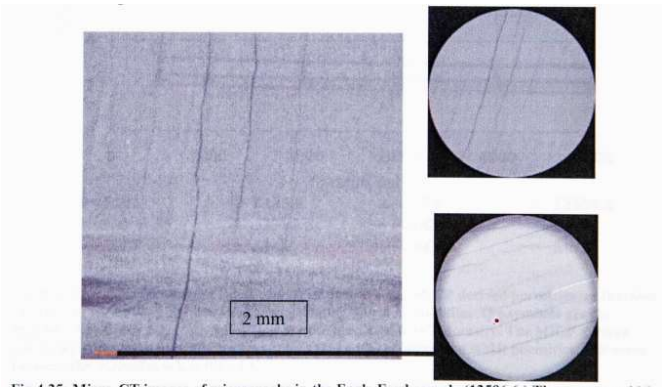

Fig 4.25: Micro-CT images of microcracks in the Eagle Ford sample (12596.6.) The average width of the imaged fracture is around 60 µm.

Figure 14. Presence of micro-cracks in unconventional formations. Reprinted from Bachir Mahomad, 2014.

2.2 Stress-dependent Permeability Considerations

Much like the pore volume change due to stress, the presence of micro-cracks in the unconventional rocks also cause the matrix permeability change. Consequently, both the pore compressibility and permeability in shale differ from its sandstone counterparts. Several models exist in the literature describing stress-sensitive permeability. The model used to understand shale permeability in this thesis is the Gangi's bed of nails model. Most of the shale formations we target for production are source rocks where petroleum is generated over geological time scale, and during the process of diagenesis, and catagenesis, the biomass is converted first into solid kerogen and then the kerogen is converted into petroleum fluids oil and natural gas. During this process a critical point in time arrives when the pore pressure associated with the generated fluids reaches a limit in mechanical strength of the rock and cracks will start to form. These cracks are not only important for the expulsion of the hydrocarbon fluids but also important to transport during our production using the hydraulically-fractured wells. They control the permeability of the formation. During the production, when the effective stress builds up in the formation near the hydraulic fractures, these cracks and small fractures will close on themselves and some of them will lose

their interconnectivity. Consequently, the formation loses its permeability. This has a large impact on the producing GOR.

Gangi's model considers the micro-cracks in the matrix are full of fictitious vertical rods of varying lengths (namely, bed of nails), when exposed to closure stress, they resist to close depending on the mechanical strength of the nails. As the micro-cracks start to close, the rate of closure slows down. The permeability modeled by eqn. 1, i.e., Gangi's permeability model, which is a power law model.

$$k = k_0 \left[1 - \left(\frac{p_{conf} - \alpha p}{p_1}\right)^m\right]^3 \quad \text{..... (1)}$$

Here, k_0 is the permeability at zero effective stress. p_{conf} is the confining pressure which is often taken to be the overburden pressure. The p_1 is the stress at zero permeability. m is the resistance of the cracks to closure. I take the differential pressure (confining pressure minus the pore pressure) is the effective stress the system is experiencing. The higher the effective stress the lower the permeability. Khoshghadam (2015) does not use this exact model, but they also use a power law model.

The Gangi's mechanistic permeability model was originally developed for split core plugs under confining pressure in the laboratory, but it also approximates the hydraulically made fractures, where the parameters have to be tuned to reflect the difference of resistance to closing and the effect of overburden stress, see **Figure 15**.

The Gangi's model can also be used for the description of the stress-dependence of the hydraulic fracture permeability, however, I should note that the key parameters k_0, m, and P_1

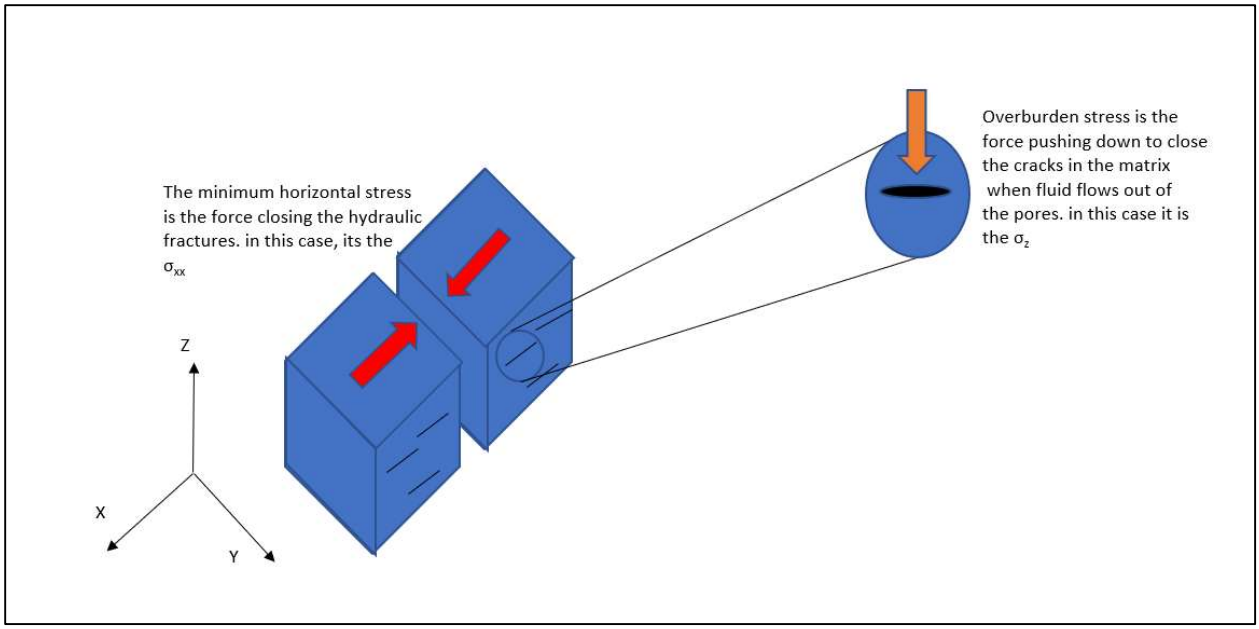

Figure 15. the direction of confining stress on both hydraulic and natural fractures in shale systems.

should be significantly different for the hydraulic fractures. Kim and Akkutlu (2019) considered the application of the model to the hydraulic fractures defining new parameters:

$$k_f = k_{f0}\left[1 - \left(\frac{\sigma_{h,min} - \alpha}{\Pi}\right)^M\right]^3 \quad \text{..... (2)}$$

The hydraulic fracture permeability model still follows the power law trend: large reduction in permeability in the beginning of production and more resistance to closure as the pressure decreases. The function of the closure is different, however. The effective stress applied to the fracture is based on the minimum horizontal stress subtracted against the pore pressure. If the fracture is not exposed to any stress, then the equation turns into:

$$k_{f0} = k_0\left(1 + \frac{.78 d_p \eta}{h_{0.Frac}}\right)^3$$

where k_0 is the permeability at zero effective stress in the absence of proppants; the d_p is the diameter of the proppant; η is the quality of proppant placement; the $h_{0.Frac}$ is the initial pore height from the fracture-wall asperities of the sample at zero effective stress.

The fracture closure stress is different from the micro-cracks in the matrix since the fracture is propped open. The equation for this is as follows:

$$\Pi = \frac{P_{Seal} E_p (D + d_p \eta_A)\left(\frac{M}{m}\right)}{E_r d_p \eta_A + E_p D}\left(1 + \frac{.78\eta}{h_{0.Frac}}\right) \quad \ldots\ldots\ldots\ldots\ldots\ldots\ldots\ldots\ldots\ldots\ldots\ldots \text{(4)}$$

M exponent from equation 5 is the resistance of the fracture to close if the fracture is propped open.

$$M = m(1 - \eta_A) + \eta_A \left[m \left(\frac{h_{0.Frac}}{h_{0.Frac} + .78 d_p} \right) + \zeta \left(\frac{h_{0.Frac}}{h_{0.Frac} + .78 d_p} \right) \right] \quad \ldots\ldots\ldots\ldots\ldots\ldots \text{(5)}$$

These parameters are the differentiation of the fracture permeability multiplier and matrix permeability multiplier.

2.2 Eclipse Flow Simulation Model with a Uniform Permeability Field

Eclipse is a commercial software and was used as the main tool for this study due to the wide accessibility that software has in the industry. The Eclipse trials are isotropic property trials to prove the concept. The first set of trials were run with constant permeability and using conventional compressibility values. The key parameter ROCKTAB was used to make the fluid transmissibility (which is a function of the permeability) an explicit and stress-dependent quantity. Transmissibility multiplier, porosity, and pore compressibility factors affect both matrix and fracture cells the same.

The transmissibility multiplier and the pore volume for the stress dependent trials are tables that were calculated in excel. The transmissibility multiplier was generated using different

parameters for Gangi's equation and the pore volume was generated by using different compressibility constants. An example of this table is Table 5 below:

Table 5. An example Rocktab table input

Pressure	Porosity Multiplier	Permeability multiplier
5000	0.96	0.034547746
5200	0.962	0.038381246
5400	0.964	0.042538618
5600	0.966	0.047041932
5800	0.968	0.051914877
6000	0.97	0.057182939
6200	0.972	0.0628736
6400	0.974	0.069016571
6600	0.976	0.075644052
6800	0.978	0.082791047
7000	0.98	0.090495721
7200	0.982	0.098799824
7400	0.984	0.107749194
7600	0.986	0.117394349
7800	0.988	0.127791204
8000	0.99	0.139001932
8200	0.992	0.151096015
8400	0.994	0.164151538
8600	0.996	0.178256798
8800	0.998	0.193512327
9000	1	0.21003347

The parameters for the porosity multiplier is a c_p = 1.0E-5 psi^{-1}. The pore volume is assumed to be at a base value at the initial pressure of 9,000 psi. The permeability multiplier was tabulated using the following Gangi parameters, m =.6, P_{max} = 13500, P_{con} = 12000, α = 1. The table signifies that in each cell, the pore pressure is used to find the pore volume multiplier, and the permeability multiplier of the cell. An example of this would be if a cell was at 6,000 psi, then the porosity and the permeability of the cell would be multiplied by .97 and .051914877. Tabulation of the stress-dependent quantities is not necessary for the NaSh simulation model because the simulation computes these quantities dynamically for both the matrix and the fractures based on the Gangi's rule. Further details of the used NaSh simulation model is below.

2.3 NaSh Flow Simulation Model with Embedded Fractures and Anisotropic Stress Field

The NaSh trials were run to test the anisotropic stress case, i.e., the differences between the matrix stress field and the hydraulic fracture stress field kept different and the difference varying as part of the study. The flow simulator uses a dual porosity-permeability with the following parameters: overburden stress, M of the fracture, m of the matrix, P of the fracture, the p_1 of the matrix, k_{f0} of the fracture, k_0 of the matrix, the pore compressibility of the fracture, and the pore compressibility of the matrix. The confinement stress was the σ_{ob} for the matrix cells, and the fracture closure stress $\sigma_{h,min}$ for the fracture cells.

The stress field of shale is not isotropic. The vertical stress and the horizontal stress can be much different. The force acting on a fracture/crack in the perpendicular direction of the propagation of the fracture is what governs the closure of the fracture. The overburden stress is the confinement pressure of the matrix, because of how the cracks in the matrix form horizontally meaning that overburden stress is the force acting on it in a perpendicular fashion. While for the hydraulic fractures propagate against the matrix by opening in a vertical fashion because the minimum horizontal stress is less than the vertical stress, and fracture propagation goes in the path of least resistance; the least horizontal stress is the force that acts perpendicular to the fractures.

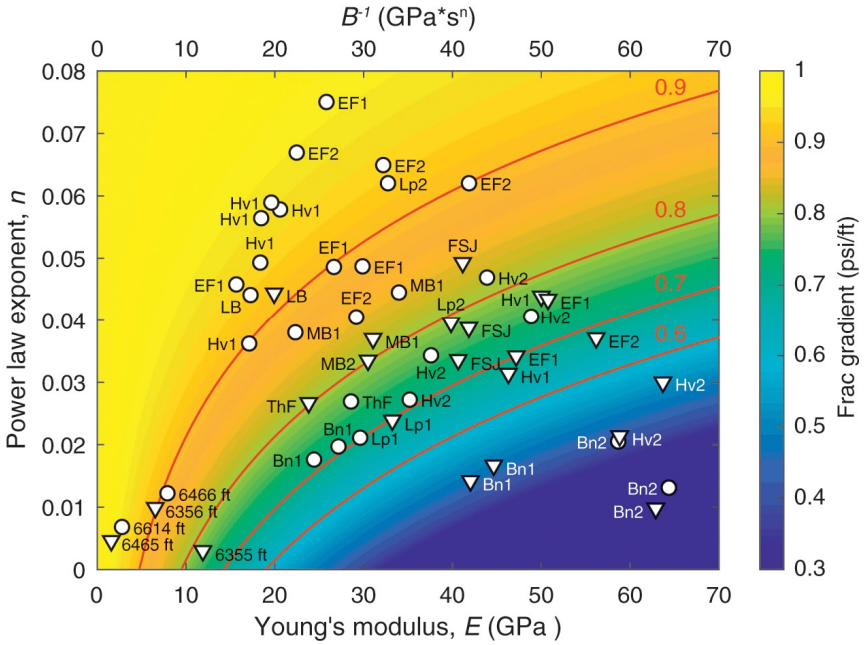

Figure 16. Power Law exponent vs Youngs modulus, distribution of the Fracture gradient which is the minimum value of the $\sigma_{h,min}$. Reprinted from Zoback 2019.

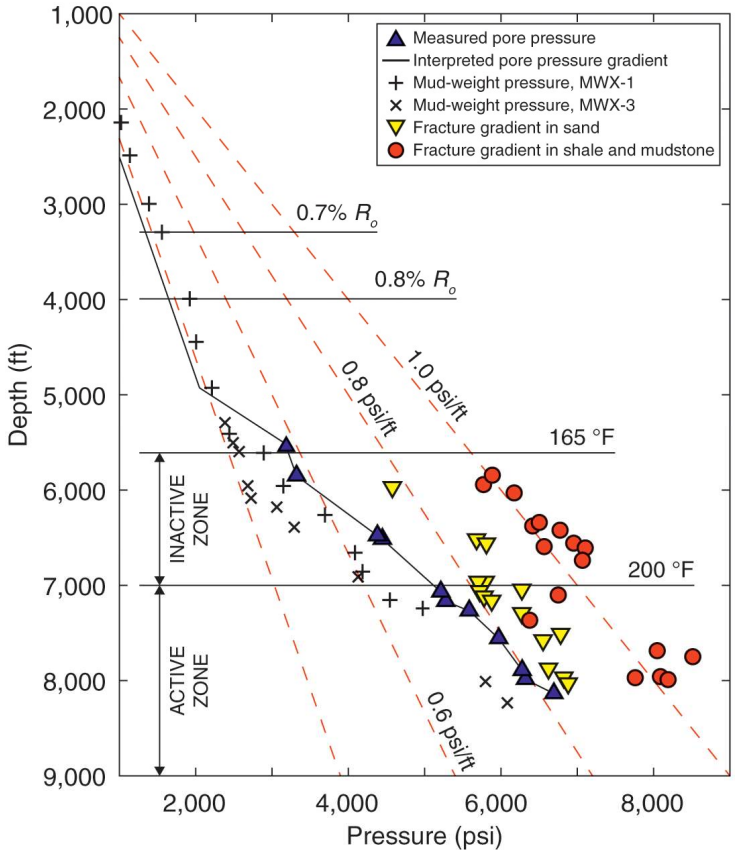

Figure 17. Depth vs pressure. In an over pressured system, shale's approaches $\sigma_{h,min}$ vertical stress. Reprinted from Zoback 2019

The overburden stress has well-documented estimates, and the minimum horizontal stress is derived from the overburden stress by accounting for the young's modulus and the lithology of the region. See **Figures 16 and 17** from Zoback (2019) The lower bound of the minimum horizontal stress is the frictional faulting equilibrium, which has a similar stress gradient as the vertical stress. A normal gradient of overburden stress is 1 psi/depth while the lowest minimum horizontal stress that can be expected is 0.6 psi/ft.

A 0.6 psi/ft gradient is much lower than what would be expected. Especially in a shale system that is over pressured. In a strike-slip fault structure, this is an expected graph of the

gradients according to Ankush (2022), where all the $\sigma_{h,min}$ for this particular reservoir scheme are between the normal faulting frictional bound, and the vertical stress gradient.

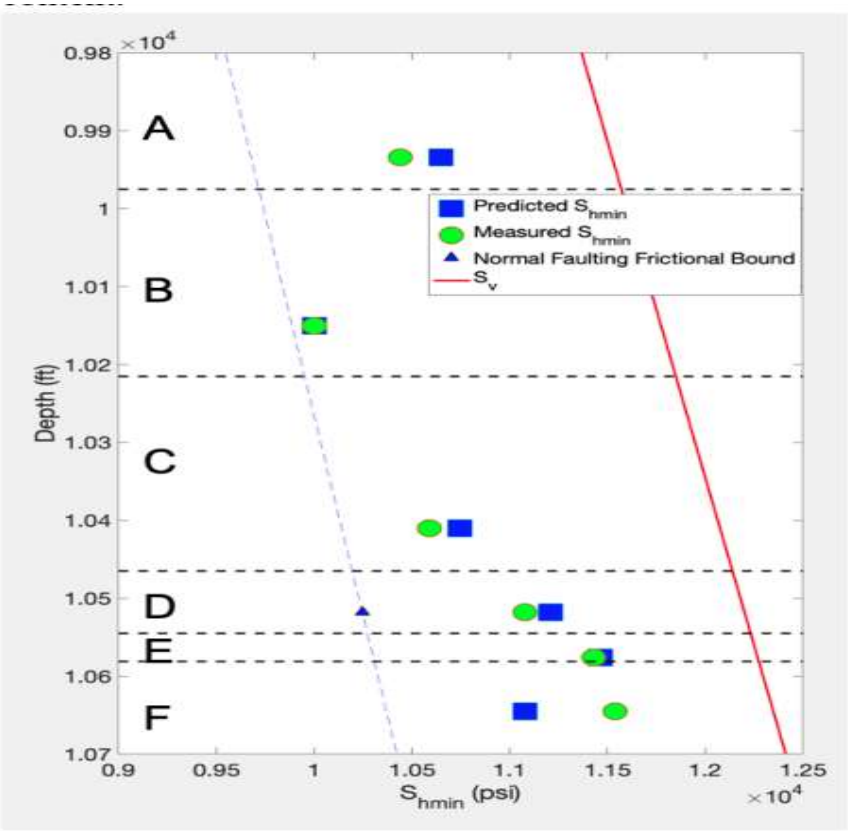

Figure 18. Graph of possible stress values for the normal stress and the minimum horizontal stress. Reprinted from Ankush 2022.

For the anisotropic trial, **Figure 18** above is used to show what the maximum effect of the anisotropic stress field has on the GOR. The depth of the reservoir is was set to 10,300 ft so that it has a overburden pressure of 12,000 psi, and the $\sigma_{h,min}$ is taken equal to 10,000 psi.

3. RESULTS AND DISCUSSION

I shall begin this chapter by reviewing the prototypical production trends I observe in my simulations for the conventional and unconventional cases. Later I will carry the discussion more in depth on the observations related to effects of a specific parameter.

3.1 Prototypical GOR Trends of Production wells

To understand the GOR trend of hydraulically-fractured low-permeability reservoirs, it must be first compared to a conventional hydraulically-fractured reservoirs. What I mean by the conventional reservoir is the reservoir with relatively high matrix permeability. I consider 50md for the simulation of the conventional case. Its producing gas-oil ratio trend is shown in **Figure 19** for nearly 3 years of production. The same figure also includes the GOR trends of the tight matrix with 0.05 md (or 50 micro-Darcy), and ultra-tight matrix with 0.0005 mD (or 500 nano-Darcy) permeability cases. The other simulation model parameters are deliberately kept the same as discussed in Chapter 2 for simplicity in analysis: production with constant fracture permeability (5,000 md), low pore volume compressibility coefficient 1.0×10^{-5} psi^{-1}, and same fluid parameters; the only parameter that is changed at each run is the matrix permeability.

I observe that the GOR range of the conventional case, goes from 0 to 20 MSCF/STB, while both the tight matrix and ultra-tight matrix cases have GOR staying low and between 10 and 15 MSCF/STB, **Figure 19**. This is already an indication that tight rocks with micro-Darcy and nano-Darcy range matrix permeability behave uniquely different than the conventional reservoirs. Hence, the flat GOR trend observed in shale wells discussed in Chapter 1 can solely be attributed

to the low permeability of the rock matrix; further I argue that all the other matrix-related effects listed in the

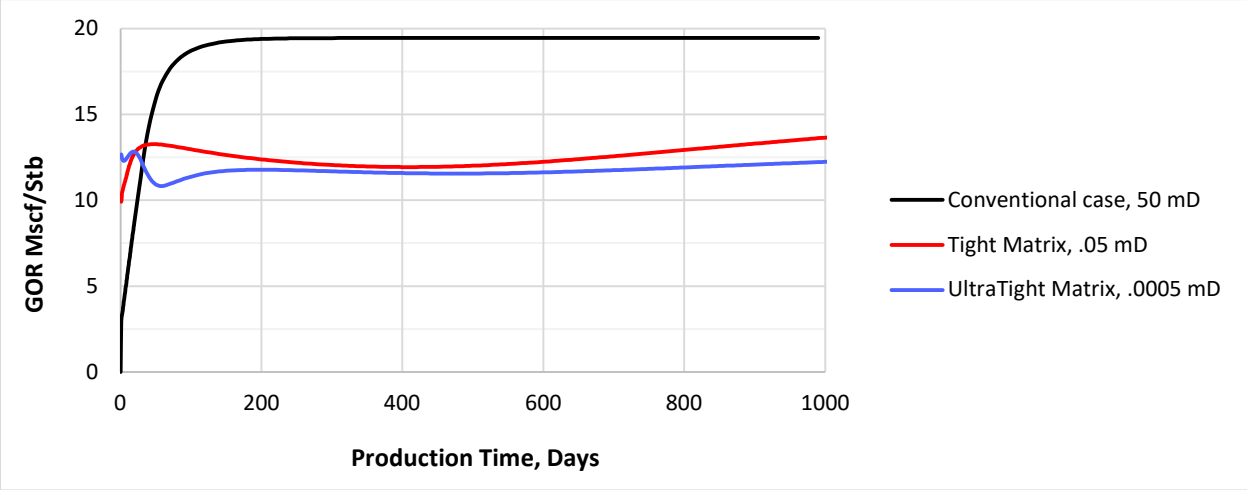

Figure 19. Dynamical GOR trends with different matrix permeabilities

literature are secondary effects on the magnitude and shape of the GOR. These matrix effects only play a supporting role, not the main role on the GOR control.

3.1.1 Conventional oil reservoirs

Investigating the conventional model is the priority because conventional reservoirs have been studied for well over a hundred years, and the difference between the tight rock and the conventional rock cannot be understood well without knowing the conventional model response. Conventional matrix of my model follows a conventional production trend: when the pressure goes below bubble point, there is an increase on GOR and the GOR stays high until the whole reservoir domain is depleted and the drainage volume can no longer supply the gas at the same rate. The sharpest increase in GOR occurs during the hydraulic fractures depletion which is only for the first couple of days.

A snapshot of the pressure and gas saturation profiles in the reservoir are laid out. I do not see too much concentrated depletion around the fractures. This is because the permeability in the reservoir is so high that fluid flow in the reservoir is not localized at any one

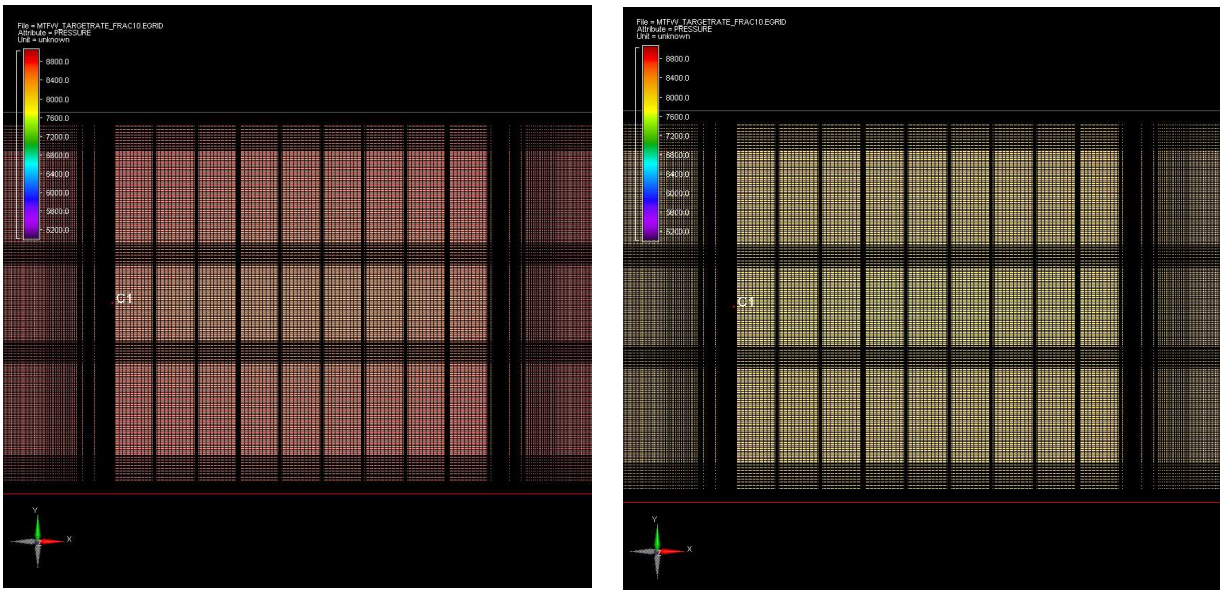

Figure 20. Pressure profile, conventional model. 6 days of production (LEFT) 10 days of Production (RIGHT)

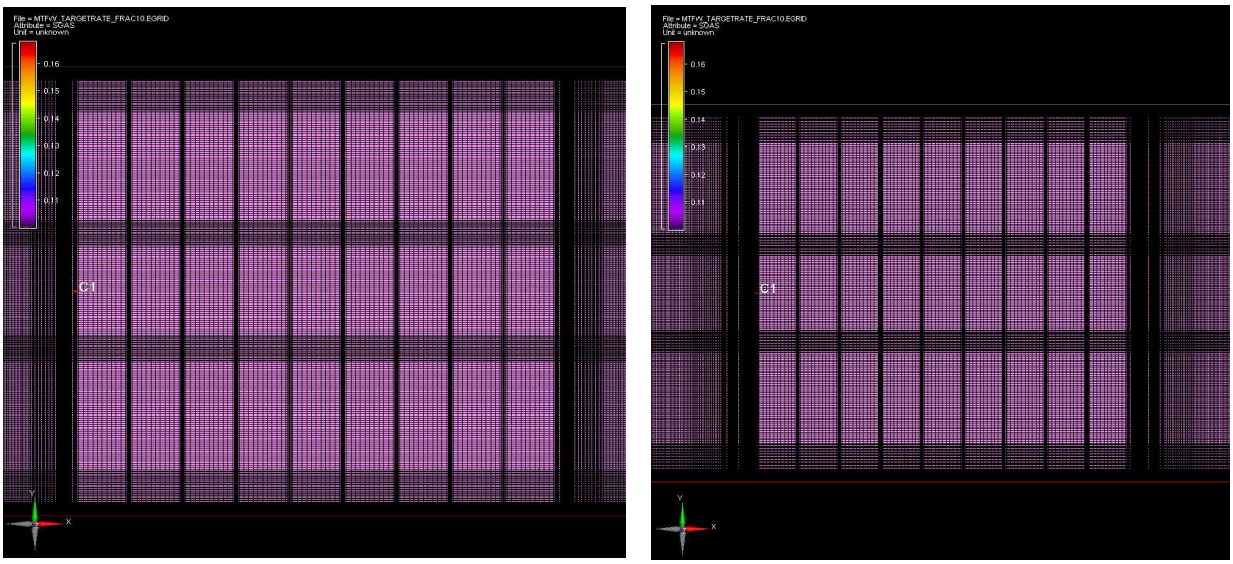

Figure 21. Gas saturation map of the conventional model at 6 days of production (LEFT) 10 days of Production (RIGHT)

point in the reservoir, **Figures 20 and 21**. After 6 days of production, the transient has already reached pseudo-radial flow because the entire well and the fractures are acting collectively as a singular unit. This reflects the radial pressure profile of **Figure 6**.

Figure 20 shows after 10 days of production the pressure propagation reaches the boundry. This will be contrasted with the tight and ultra-tight reservoir models in the next section, where the tight models take years to reach the boundary of the reservoir. There is a trend of the pressure having a gentle gradient in throughout the propagation. The gas saturation has increased throughout the reservoir by a small amount, because the p_{wf} is below bubble point. Between days 7, and 10 the entire field has a uniform pressure drop from 8600 to 7600.

3.1.2 Tight oil reservoirs with micro-Darcy Permeability

The tight matrix case, and the ultra-tight matrix behavior are similar because they experience flow completely dependent on the fractures which causes the flow in the system to go through a sequence of linear and boundary influenced flow, while the conventional case does not follow this flow regime because

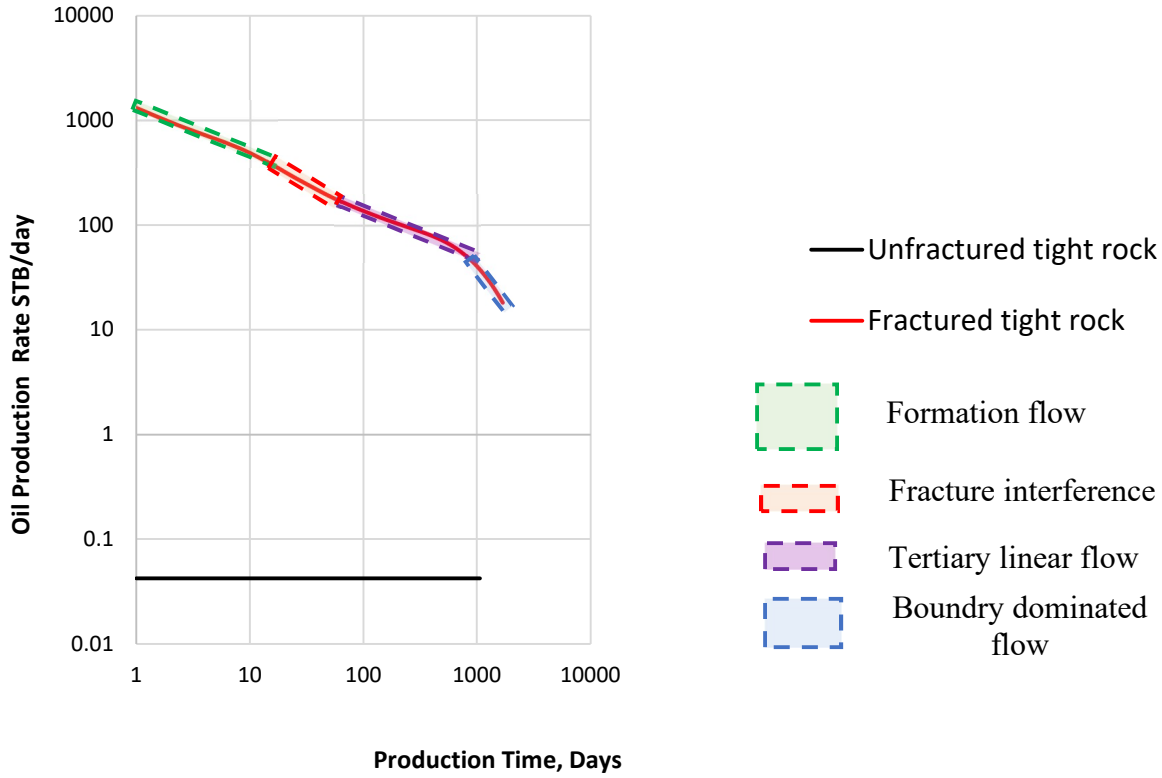

Figure 22. Oil production rate vs time using fractured and unfractured well for the tight rock models.

the matrix permeability is high enough to be produced from directly. In these tight reservoirs the presence of fractures changes the transient nature of the flow significantly. We see that the unfractured well experiences radial flow as a flat line but the fractured well shows several trends developing in the production line, **Figure 22**. Without the fractures, the production is so low, and this indicates to us the reason why these tight formations cannot be exploited economically without the hydraulic fracturing. With the fractured well with infinite conductivity hydraulic fractures the following flow regimes are identified in **Figure 22**: the green boxes are the formation linear flow; The red box is the boundary-influenced flow caused by fracture interference; and the blue box is

the tertiary linear flow, which develops parallel to the fractures, after the fracture linear flow and formation linear flow regimes, hence the name tertiary. Note that, because the fractures have infinite conductivity the fracture linear flow and bilinear flow regimes develop so fast and do not appear in Figure 22. The formation linear flow is the flow in between the fractures perpendicular to the fractures, and can be observed in **Figure 22** with the characteristic slope between ½. The boundary influenced flow is the flow when the low-pressure waves moving away from the individual fractures meet each other, or when the fracture interference begins, and it can be seen in **Figure 22**, when the rate partially starts to form into unit slope at 10 days of production, but never actually reaches unit slope. The tertiary linear flow is flow when the low-pressure wave starts to propagate outwards as a singular unit and can be seen in **Figure 22** at day 80 when the slope goes back to ½ slope. The outer boundary influenced flow happens when the pressure propagation of the well hits another wells pressure propagation. In my study, this develops when the low pressure wave reaches the outer boundary of the reservoir model. It is seen in **Figure 22**, at the end of production when the rate goes to being unit slope. All these flow regimes will be studied on the pressure profile maps from **Figures 27-47**. Note however that not all flow regimes can be seen in all the cases.

Now let us discuss the GOR trends in tight rocks with and without fractures. **Figures 23**, shows the GOR of the tight rock model with and without fractures. Without the fractures, the production is so low that there is no opportunity for gas to form or for any meaningful transport of fluid to happen. Without the fractures, the GOR stays at the solution gas-oil ratio of the oil. The observed GOR difference between the fractured model and the unfractured model is caused by the additional pressure drop in the fractures that forms gas inside

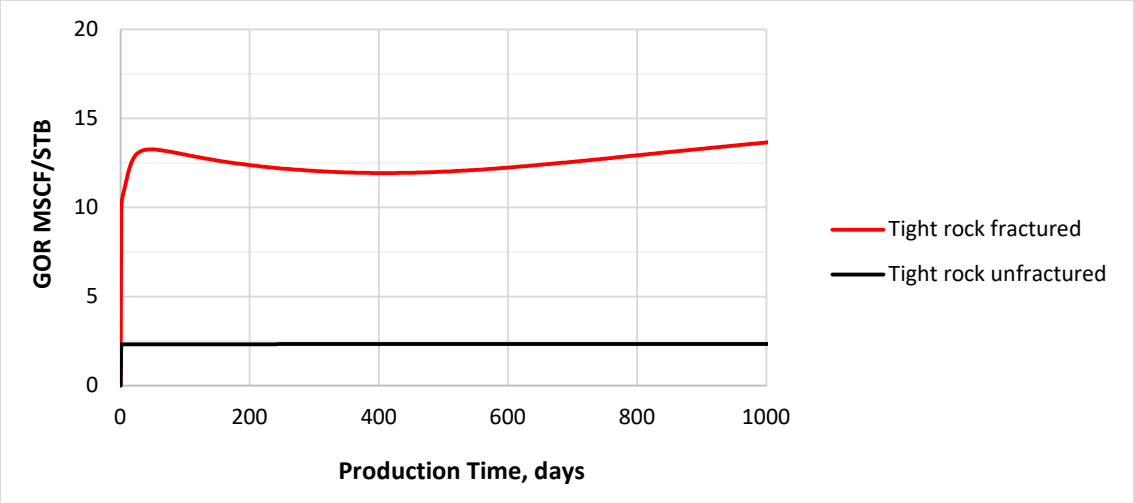

Figure 23. GOR vs time using fractured and unfractured well in tight rock models

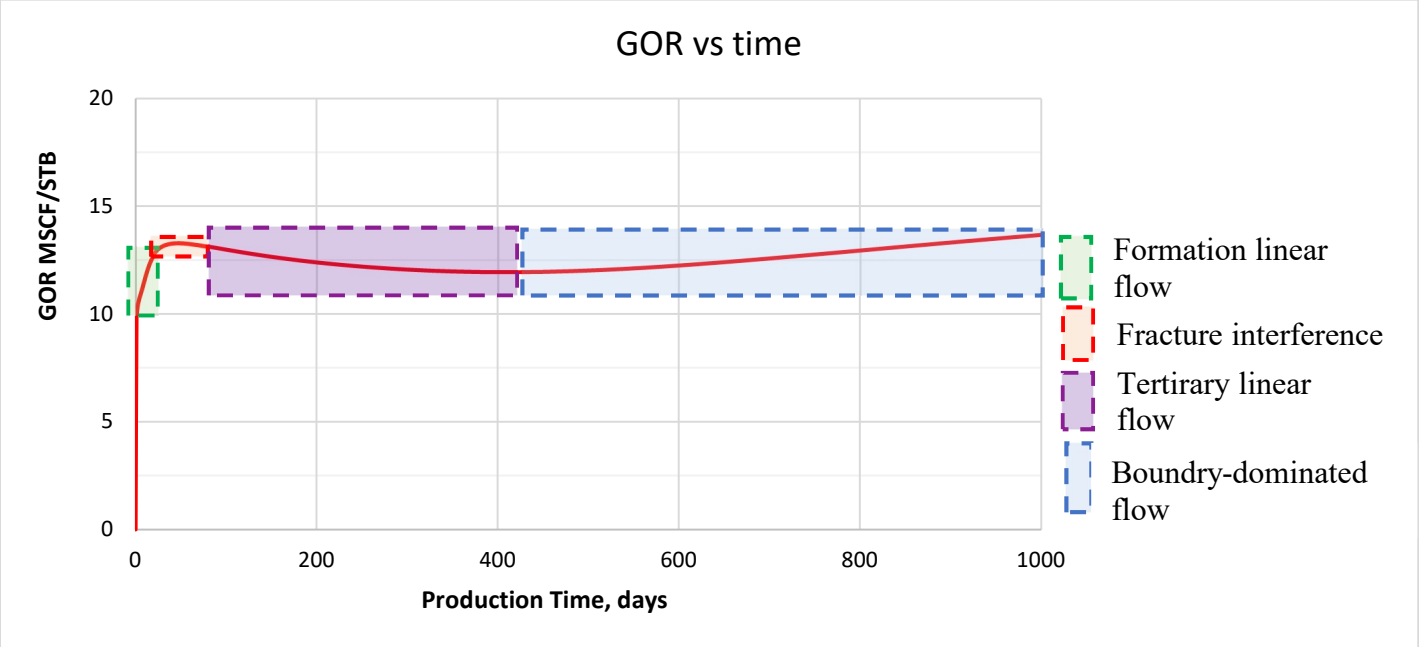

Figure 24. GOR trend of Tight matrix model with the critical areas highlighted

the fractures. The fast pressure depletion occurs inside the fractures, and it slowly spreads throughout the reservoir. This spreading creates a constant gas saturation region near the hydraulic fractures. This is explored more in the saturation and pressure maps where this pressure propagation scheme is seen clearly.

I have broken up the trend into several stages of production the well goes through, **Figure 24**. These stages can be used to identify the flow regimes easily. As production happens, the total flow rate decreases, however as different stages of production happen, the rate of decline changes. When the GOR goes down then the gas rate is decreasing faster than the oil rate, while if the GOR goes up that means the oil rate is dropping faster than the gas rate is.

Linear fracture flow and bilinear flow develop over minutes for the chosen fracture permeability value, so it would not be seen as the smallest time step is 1 day. The first stage of production in my simulations is the formation linear flow and the fracture depletion. The depletion of water in the fractures causes the GOR to increase, while the formation linear flow usually pulls that high GOR down. So, this discussion shows that, if both the formation linear flow and the fracture depletion are taking place simultaneously, then the fracture depletion will override the flat GOR trend during that initial production. The fracture depletion is then the determining factor on what the GOR value will be: if the BHP is lowered further, the observed GOR plateau will go up higher; if the BHP is increased, the plateau will go lower. The second stage is the boundary-influenced flow due to fracture interference. The boundaries of a low-pressure wave initiated by the production from one fracture are the low pressure waves of the neighboring hydraulic fractures. When this happens, the fracture interference develops on the production of the hydraulic fracture and the oil and gas production rates are both decreasing at the same rate. The third stage is the pseudo radial flow, where the well and its hydraulic fractures act as one large-diameter well experiencing radial flow. The fourth –and final-- stage is the boundary influence due to the outer boundary of the simulation box.

To help visualize the flow regimes better, several profiles of pressure and gas saturation are mapped out at critical time intervals to see what is happening in the reservoir during the

pressure transient and how it compares to the GOR trend. **Figures 25-34** are of the pressure and gas saturation profile.

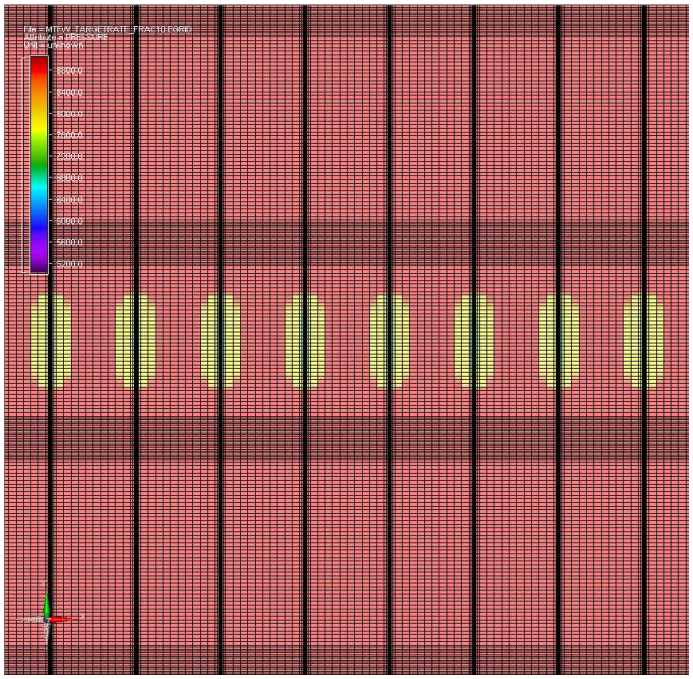

Figure 25. Pressure profile of tight oil case at 24 hours of production

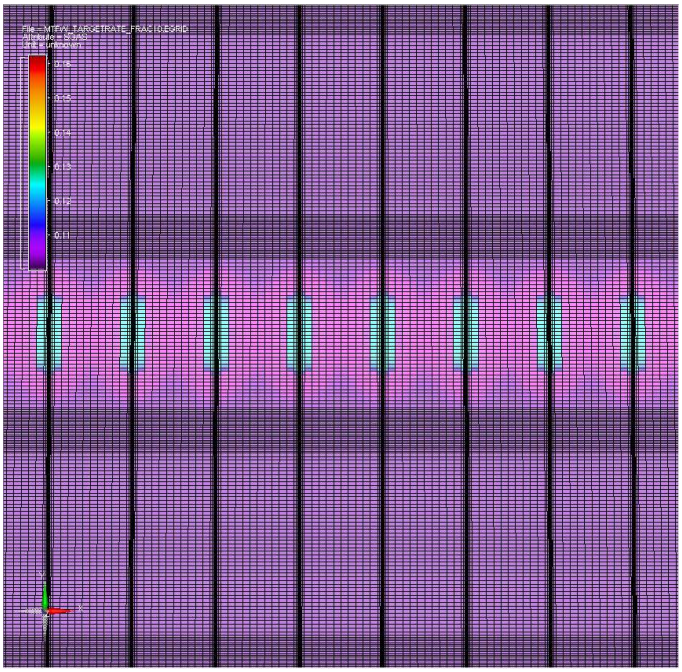

Figure 26. gas saturation profile of tight oil case at 24 hours of production

Figures 25 and 26 show the pressure profile and gas saturations of the tight rock case at 24 hours of production. Now comparing this to conventional model (previously shown in **Figures 20-21**), the pressure and the gas saturation profiles occur in very localized manner and the changes appear sharp. After 24 hours of production, the fractures have gone through major depletion, in **Figure 25**, the fractures pressure has dropped from 9000 psi to 6600 psi. The pressure profile shows that depletion has already begun in the area surrounding the fractures, and that a low-pressure wave is propagating mostly in a linear way perpendicular to the fractures. The fluid flow in the reservoir is highly localized around the fractures, which is a sharp contrast with the conventional reservoir where the pressure propagation was gradual. This follows with **Figure 6** where the pressure propagation is gradual for radial flow, while in the linear flow pressure profile there is a low-pressure zone for an extended period of time and then a sharp increase. The fracture is still depressurizing, and this can be seen from the change in the pressure profile, **Figure 25** and **27**, where the pressure drops in the fracture from 6600 psi to 5300 psi. The pressure propagation is almost exclusively between the fractures which is why it is linear flow.

The gas saturation profile from **Figure 27** shows the location of the gas saturation profile does not match the pressure profile one-to-one, because the gas saturation is expanding with a phase-changing front that is propagating faster than the pressure wave. There is already contact between the gas saturation fronts.

Figures 27 and 28 show the pressure profile and gas saturation at 16 days of production. At 16 days of production, the GOR trend starts to flatten out. In the pressure profile map at 16 days of production there are 4 pressures, **Figure 27**: the initial pressure of 9000 psi which is the area not yet affected and shown in red; the initial pressure propagation, in this case 7850 psi shown in

yellow; the intermediate pressure propagation front, in this case 6700 psi shown in light blue color; concluding with the last pressure propagation front, that is 5300 psi in this case shown in purple color. The gas saturation map in **Figure 28** shows similarities and differences from the pressure map. The similarity is that there are also four zones with characteristic gas saturation values; however, the gas saturation map is already starting to propagate out of the well as a singular unit instead of as individual fractures.

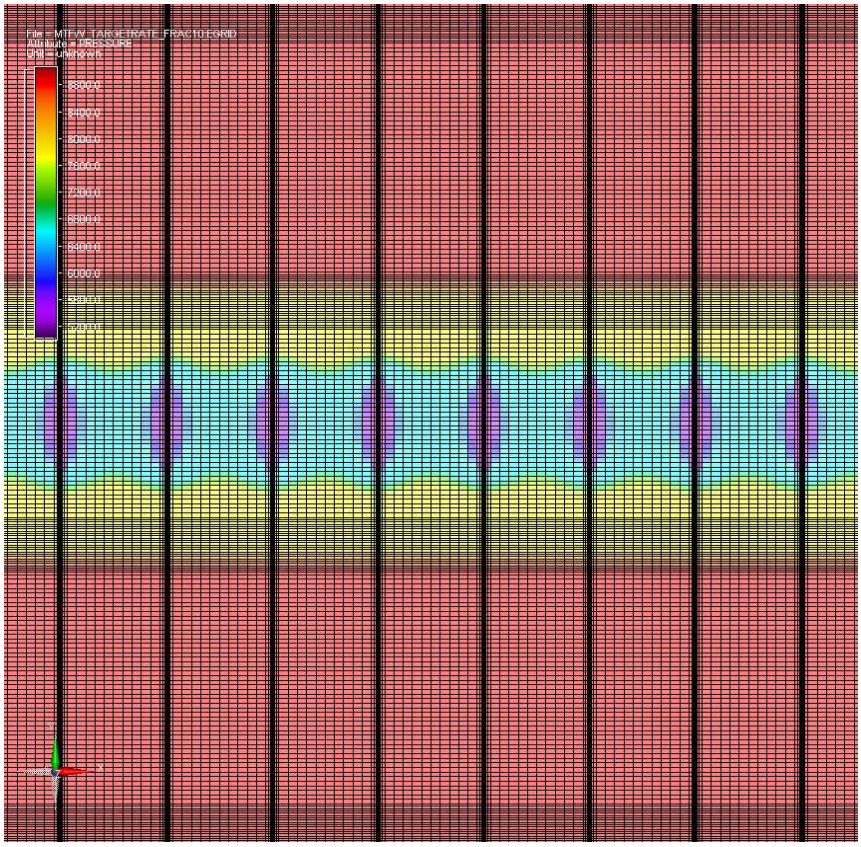

Figure 27. Pressure profile of tight-oil model at 16 days of production

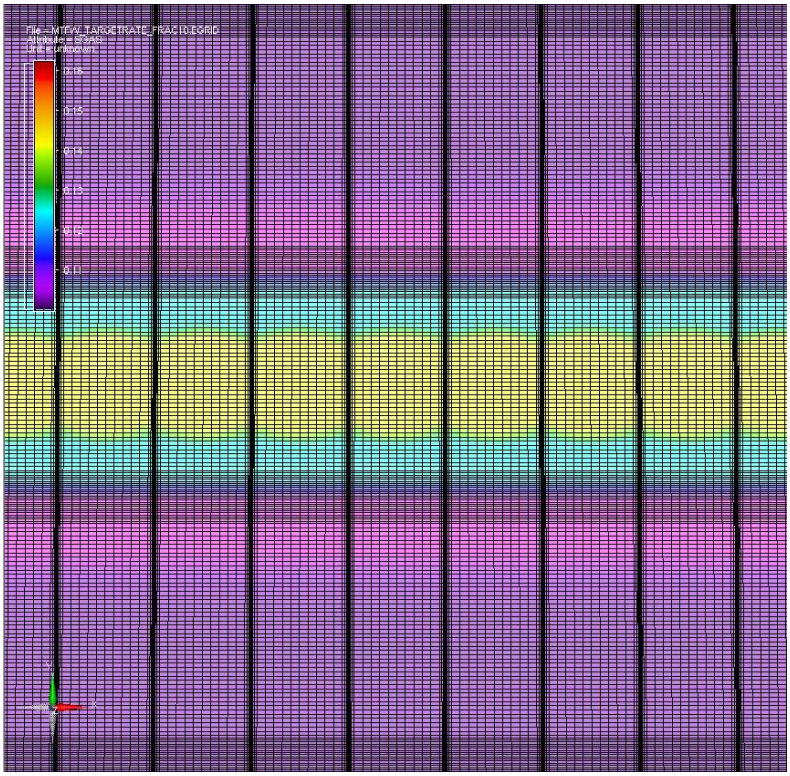

Figure 28. Gas saturation profile of tight-oil model at 16 days of production

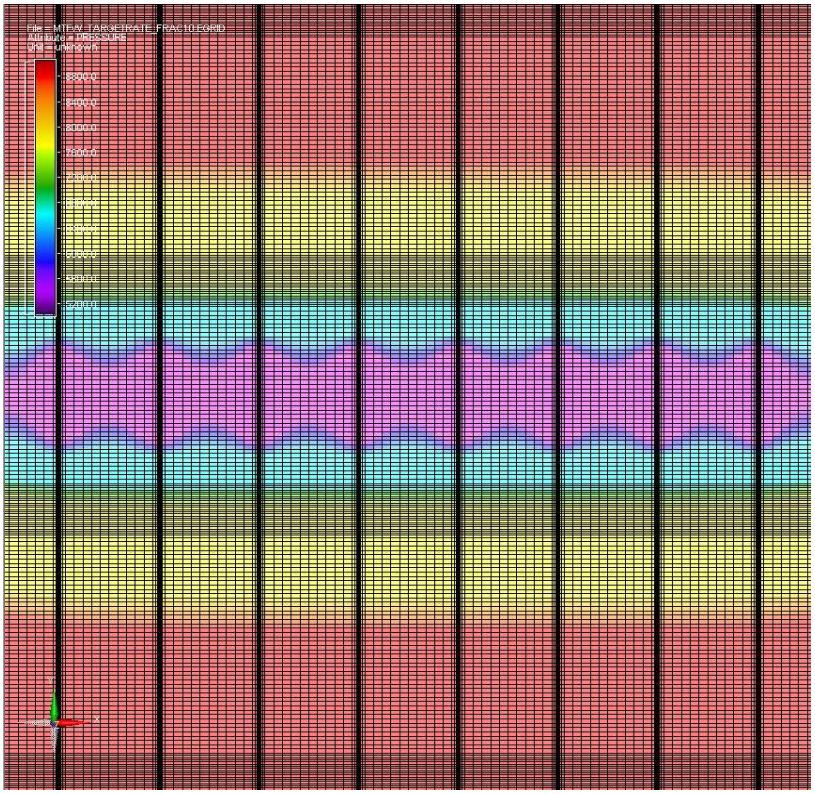

Figure 29. Pressure profile of tight-oil model at 57 days of production

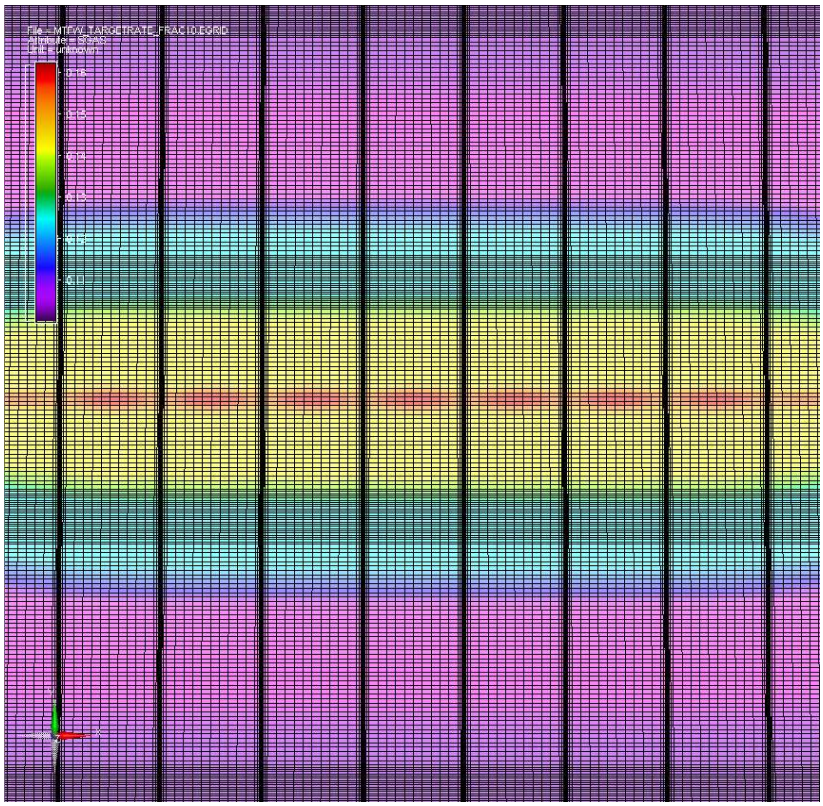

Figure 30. gas saturation profile of tight-oil model at 57 days of production

Figures 29 and 30, show the pressure and gas saturation maps at 57 days of production. After about 2 months of production, the low-pressure wave propagation has completed in a way where the fractures are fully communicating with each other, and functionally the fluid flow should be boundary influenced from the fracture interference. This is not true boundary dominated flow, in the production rate **Figure 22**, the trend goes from ½ slope to unit slope temporarily but will transition back to linear flow. At this point, if the well was bounded by the reservoir, or by another well close by, this would be the final stage of fluid flow, but since it is unbounded the well will transition to a pseudo radial flow. In the fractures, the gas saturation has reached its maximum value, and is spreading around the well bore. This contrasts with the pressure propagation which has not experienced a new front.

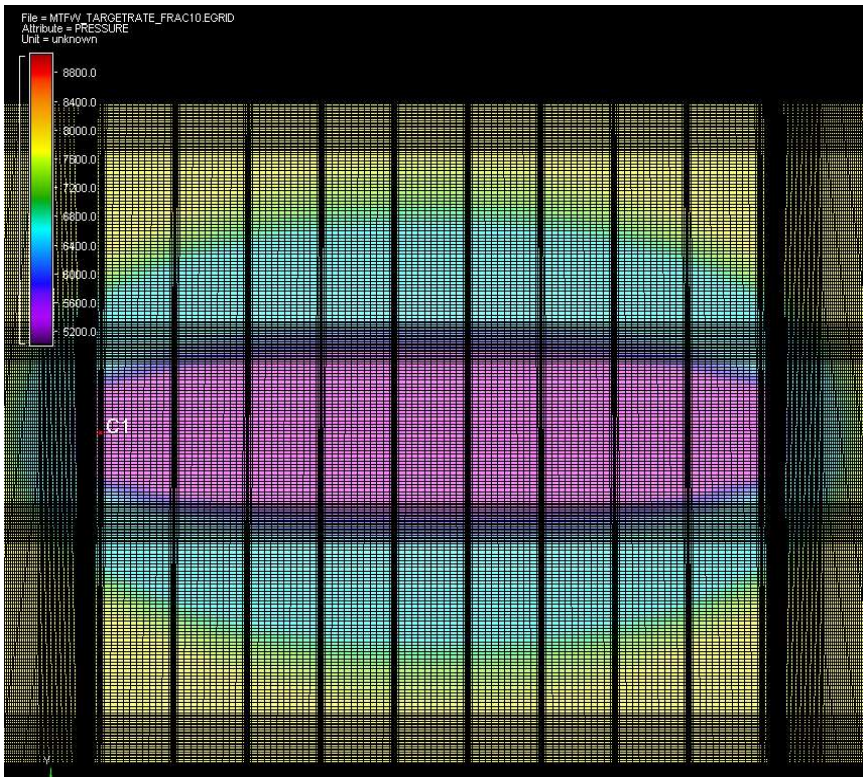

Figure 31.Pressure profile of tight-oil model at 1 year of production

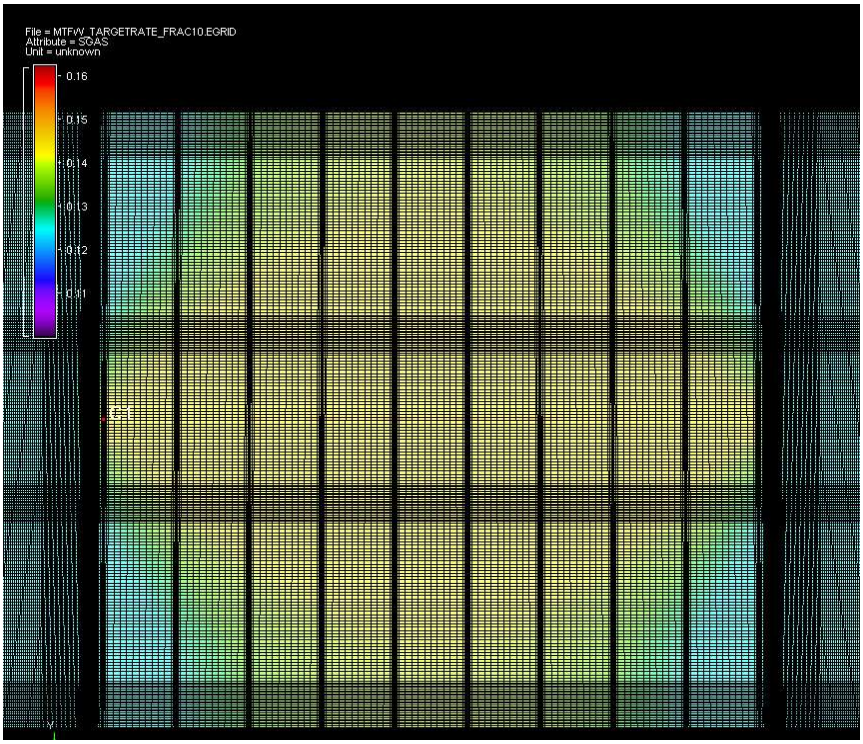

Figure 32. gas saturation profile of tight-oil model at 1 year of production

Figures 31 and 32, show the pressure profile and gas saturation map at 1 year of production. By one year of production the pressure is propagating pseudo-radial, and the GOR is slightly decreasing because of it. The first pressure propagation front has reached the edge of the reservoir which will lead to the GOR to start increasing. The gas saturation map no longer has the maximum gas saturation zone, which likely means that exsolution gas has been compressed back into the oil. The gas saturation propagation has already reached the edge of the reservoir.

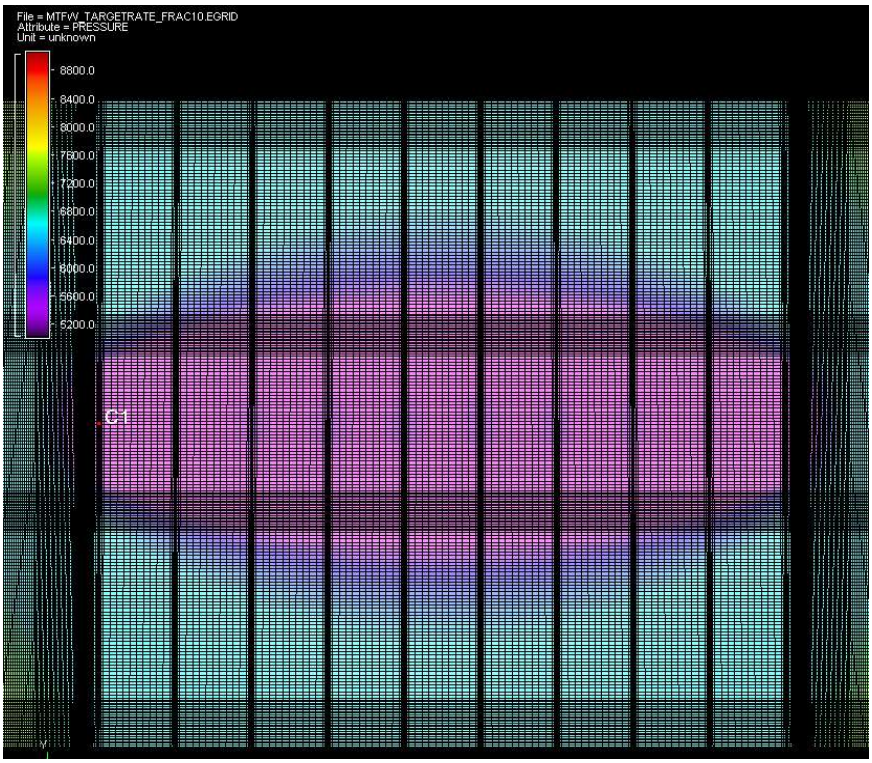

Figure 33. Pressure profile of tight-oil model at 2 year of production

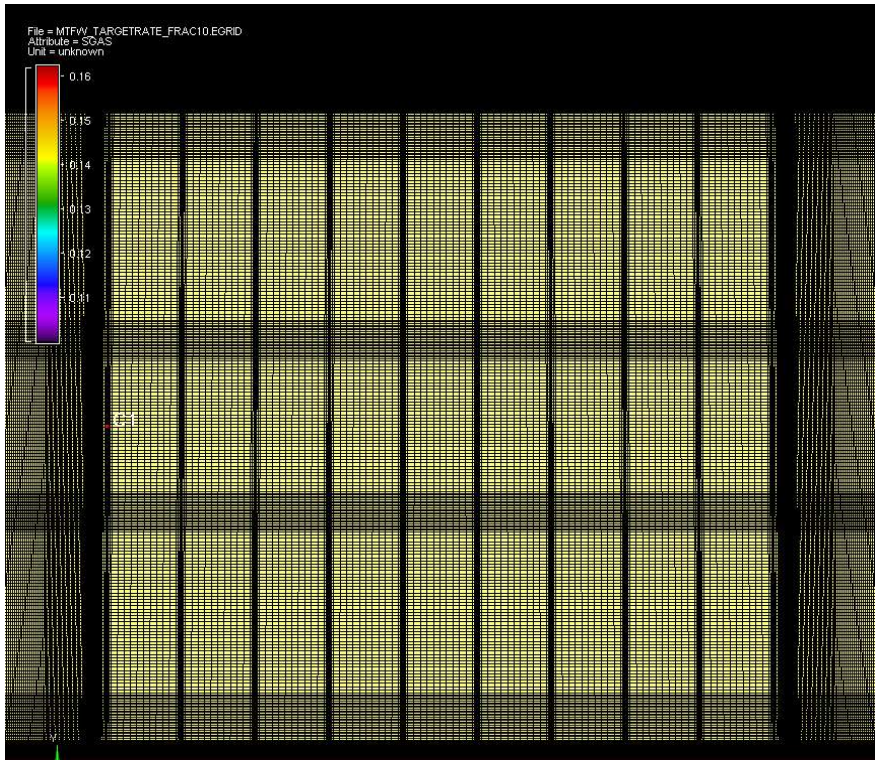

Figure 34. Gas saturation profile of tight-oil model at 2 year of production

Figures 33 and 34, show the pressure profile and gas saturation map at 2 year of production. After 2 years of production, the gas saturation of the reservoir is uniform around the well to the boundary of the reservoir. There are still two pressure zones; the final pressure zone will continue to pseudo radially propagate until it reaches the end of the reservoir, at which point the production will cease. The system has reached its max gas saturation, and unless the drawdown is increased then this is the final stage of production.

3.1.3 Ultra-tight oil reservoirs with nano-Darcy Permeability

I have so far explored how production trends develop for the wells producing from conventional, and tight rock cases, both with hydraulic fractures. Now I would like to delve into production trends in ultra-tight rock. I would like to understand differences in GOR trends between the reservoir matrix having micro-Darcy and nano-Darcy permeability. Ultra-tight shale is usually specified as a shale with a permeability of less than 1 micro-Darcy or 1000 nano-Darcy. This low-quality reservoir rock is a major part of unconventional development and being able to profitably extract from these plays is unlikely currently but may become a necessity in future.

The GOR trend of the ultra-tight model is shown below in **Figure 35**. The nano-Darcy permeability leads to a production trend where the fracture depletion and the primary linear flow develops within a large period. Previously in the tight matrix case, it took less than a month for the

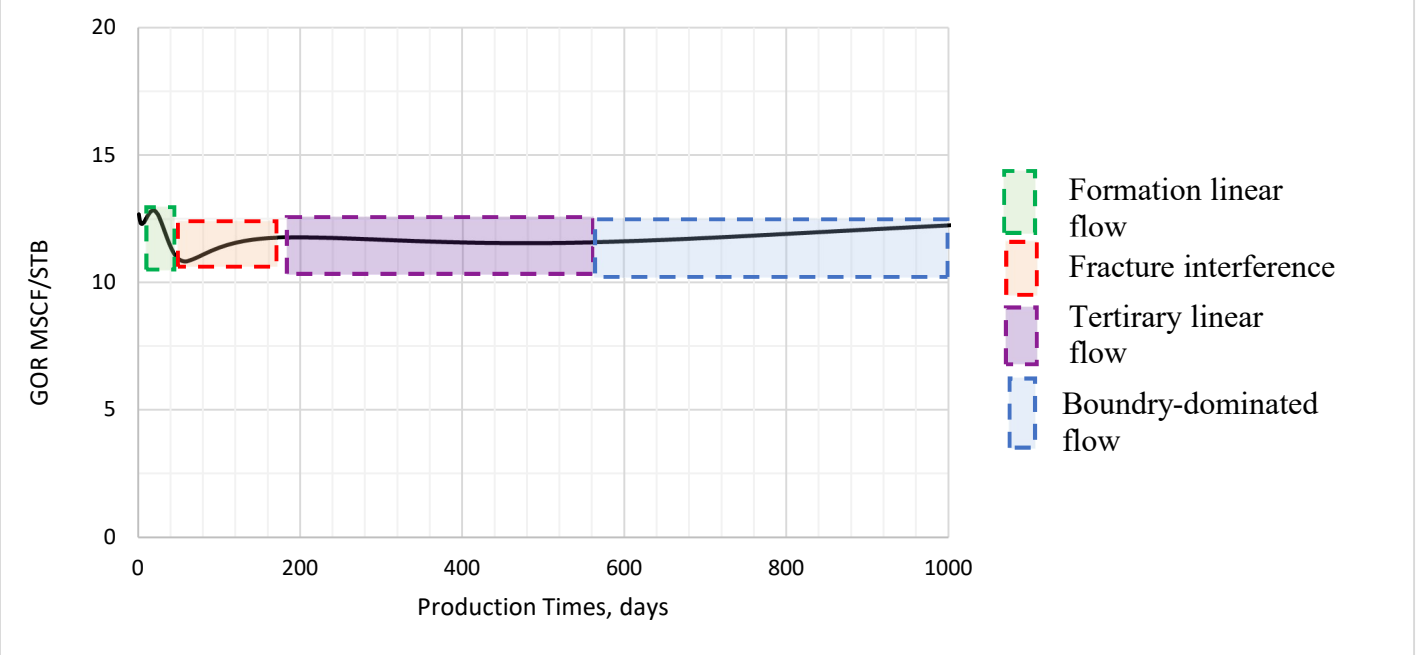

Figure 35. GOR versus production time of ultra-tight case with 500 nano-Darcy matrix permeability

fractures at large distances to interfere, however in the ultra-tight case now it takes 200 days. The initial peak seen in the first week of production is the fracture depletion, which is already a deviation from the tight case which experienced 24 hours for the depletion. This initial transition might have more to do with gridding of the transition from smaller fracture cells to the larger matrix cells. The flattening out period at 2 months production is from the fluid flow being entirely formation linear flow. This will all be explored through pressure profile and gas saturation maps in **Figures 36-43**.

Figures 36 and 37 are the pressure and gas saturation maps at 1 day of production. After one day of production, the ultra-tight case has propagated into the matrix significantly less than the tight case. The pressure propagation is so slow that it is required for a close up shot on the fracture to even see the pressure propagation. The fracture depletion for the ultra-tight case takes a significant amount of time to complete and should not be ignored during the analysis. The initial propagation front has just barely reached the cells adjacent to the fracture.

Figures 38 and 39 are of the pressure and gas saturation maps at 60 days of production. By 60 days of production, the GOR has reached its minimum. However, the fractures interference has not started yet, so the flow is in formation linear flow but has not experience any boundary effect yet. The gas saturation map however is beginning to start to reach the other fractures, which is why the GOR will start to increase again.

Figures 40 through 41 are a series of pressure and gas saturation maps at 200 days of production. After 200 days of production, the low-pressure waves have finally met at the midpoint in between the other fractures. This gravely differs from the tight case, because in the ultra-tight case it has taken 200 days to reach boundary influenced flow, while in the tight case, it started to transition away from boundary influenced flow at 60 days of production. The difference in rock

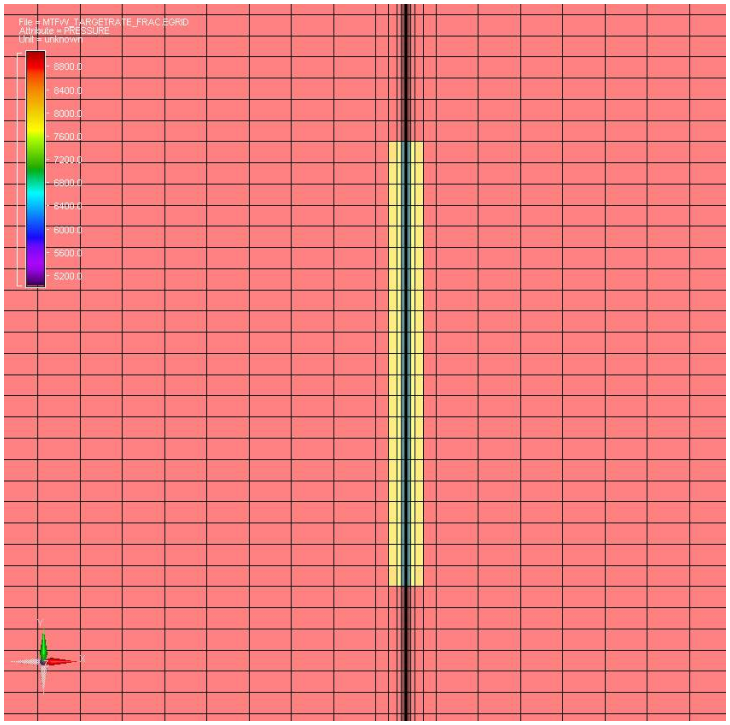

Figure 36. Ultra-tight pressure map, 1 day of production. Close up on the fracture

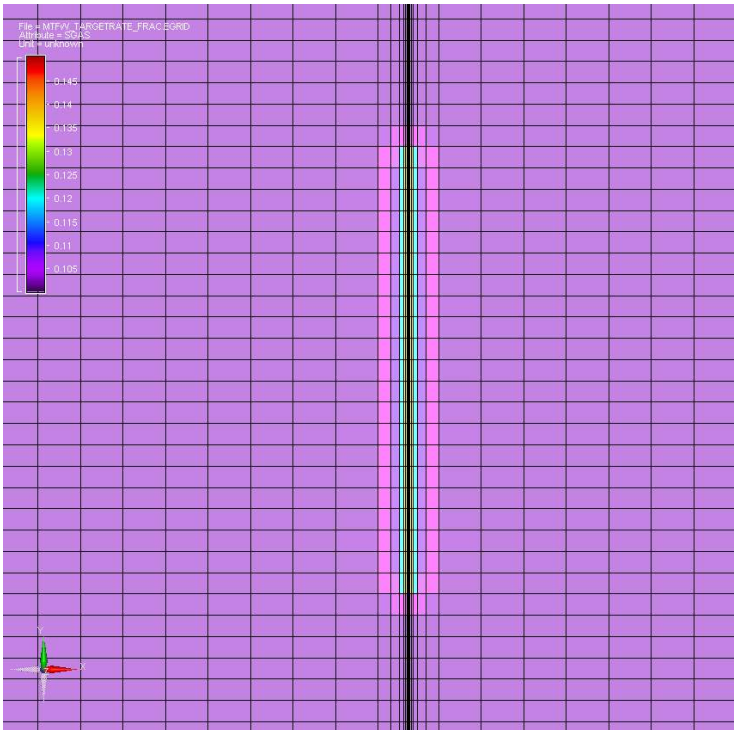

Figure 37. Ultra-tight case gas saturation map, 1 day of production. Close up on the fracture

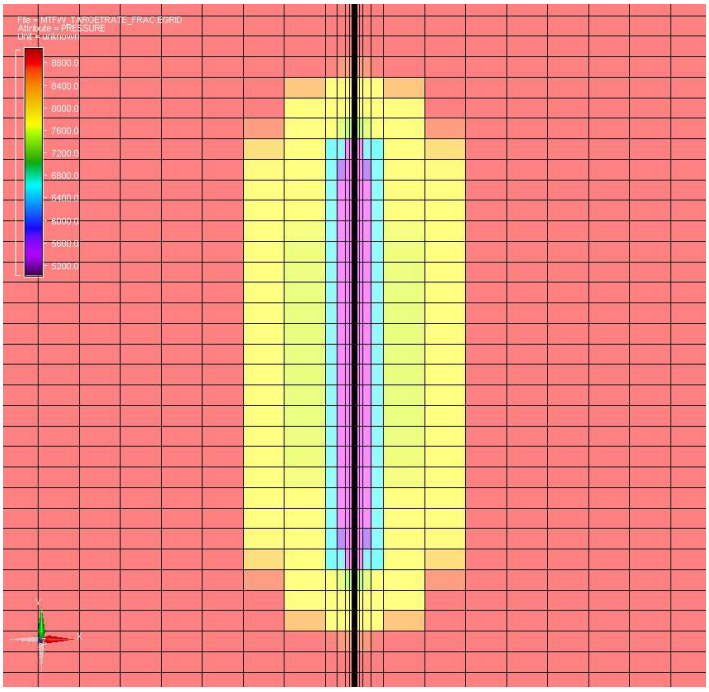

Figure 38. 60 days of production, ultra-tight case, pressure profile.

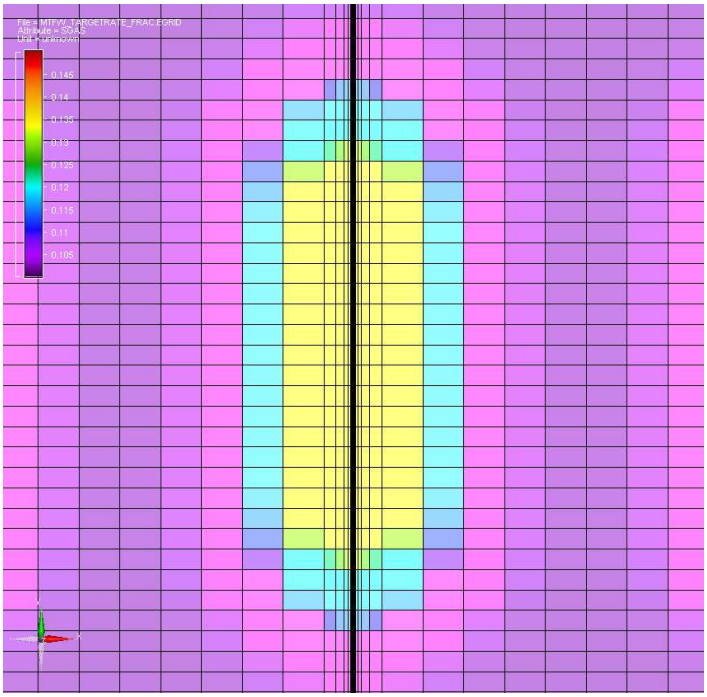

Figure 39. 60 days of production, ultra-tight case, gas saturation profile.

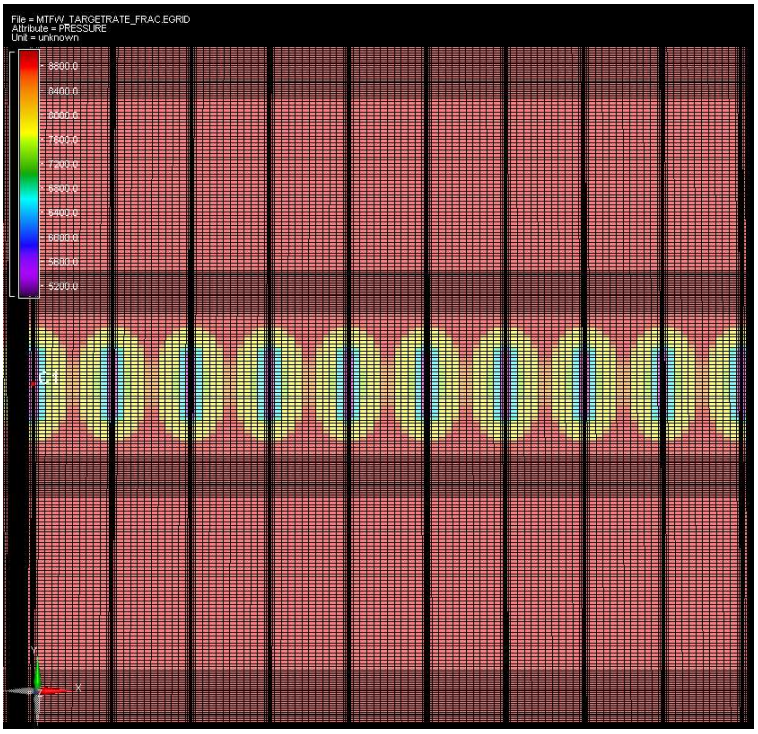

Figure 40. Pressure profile of ultra-tight case at 200 days of production

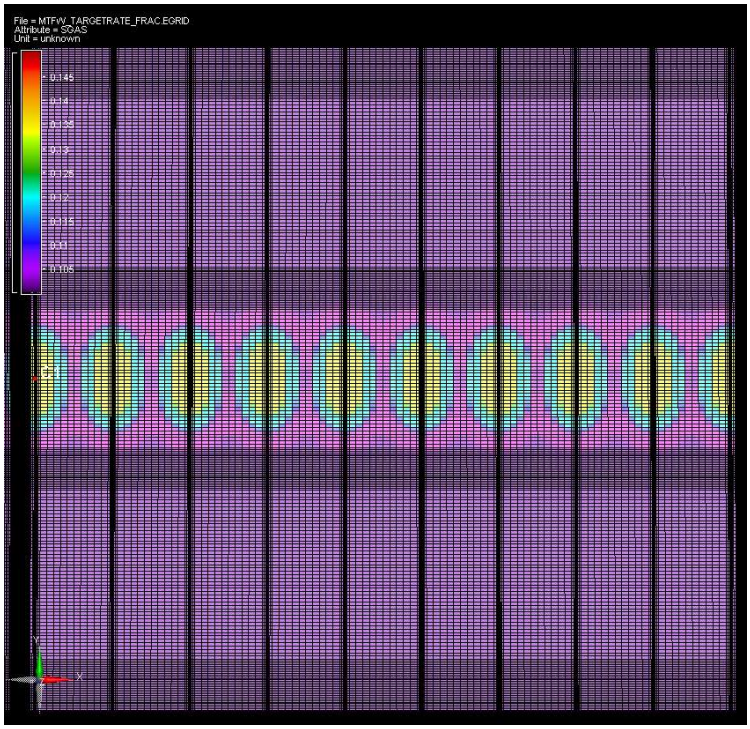

Figure 41. Gas saturation profile of ultra-tight case at 200 days of production

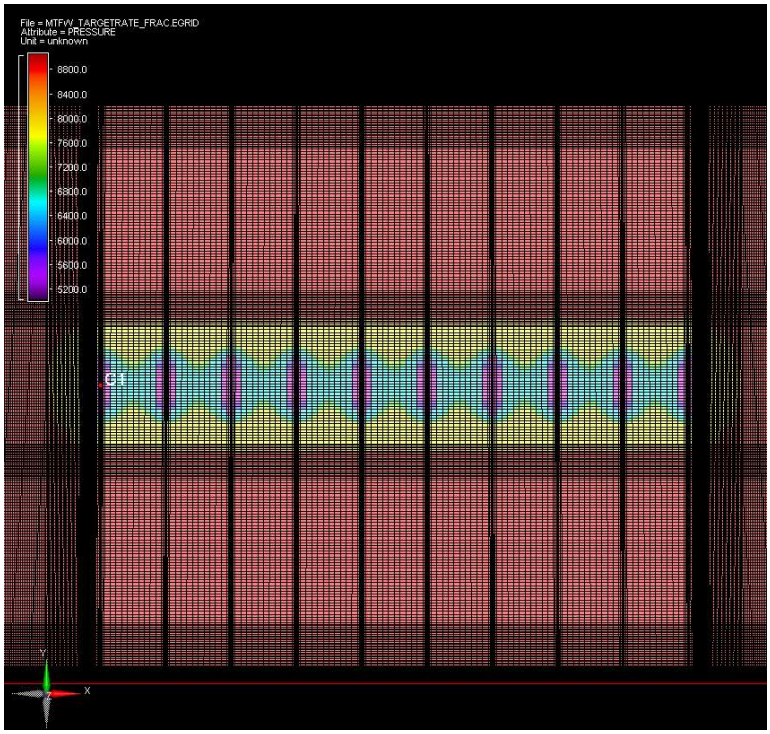

Figure 42. Pressure profile of ultra-tight case at 2 years of production

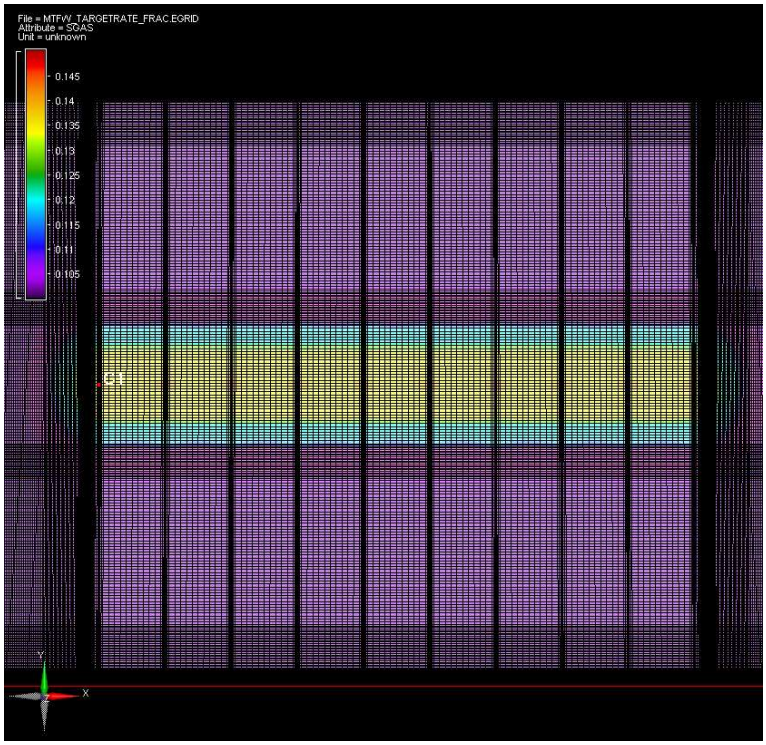

Figure 43. Gas saturation profile of ultra-tight case at 2 years of production

quality shows that large differences exist in the timing of fluid flow regimes and propagation fronts movement. Due to the extended period of time it takes for the ultra-tight rock compared to the tight rock, if the rock being produced from is closer to being ultra-tight, the fracture spacing and well packing should also be tighter to maximize the areal coverage.

Figures 42 and 43 are a series of pressure and gas saturation maps at 2 years of production. There are still pressure fronts propagating between fractures but the gas saturation field has started to move outside of the fracture zone and show pseudo radially trends.

3.1.4 GOR trends and their meaning

Between the tight rock model and the ultra-tight rock model, certain differences in GOR trends appear due to changing flow regime and the to the interaction of the fractures and with the matrix. Firstly, there is an increase in the GOR at the beginning. The fracture depletion causes solution gas to come out of the oil phase in the fractures and increase the producing GOR to increase. During the fracture depletion, the fractures and the immediate surrounding matrix are at the P_{wf} value, which leads to a zone of free gas appearing, and this zone of free gas is the driving force of the producing GOR. Consequently, the initial GOR trends with the unconventional wells in ultra-tight formations are functions of the applied P_{wf}. Following the fracture depletion, the formation linear flow in between fractures causes the GOR to slightly decrease. This slight decrease will be flattened out later by the fracture's interference, when the low-pressure waves of the nearby hydraulic fractures collide and create a boundary-influenced flow conditions in between the fractures. Eventually the well will start to propagate as a singular unit in a pseudo-radial fashion, and the GOR will start to decrease again. Then when the reservoir boundary is reached by

the pressure wave, the GOR will start to increase slowly. These processes develop extremely slow in the ultra-tight case, and in a real well, the actual GOR will look perfectly flat.

3.2 Dimensionless fracture conductivity effects on GOR

The previous analysis done was done on planar fractures with permeability of 5 Darcy. This permeability is high enough to be considered infinite conductivity. In **Figure 4**, Jones models show the difference between high conductivity wells and low conductivity wells. The analysis done in this paper is for high conductivity and wells, and therefore it needs to be determined at what permeability ranges is it the classification of high conductivity valid. Several trials were taken place, with constant permeability, and low compressibility with different fracture permeability to see the effect of dimensionless fracture conductivity (F_{cD}).

$$F_{cD} = \frac{k_f * width\ of\ the\ fracture}{k_m * Length\ of\ the\ fracture}$$

There are differing cut off points for when the F_{cD} is considered to be infinite conductivity, where the cutoff point is usually drawn somewhere between 30 to 100 F_{cD}. The trial results are shown in **Figure 44**.

Table 6 Dimensionless fracture conductivity trials, with their fracture permeability, and their calculated FcD

Kf	FcD
50000	381.025
5000	38.1025
500	3.81025
50	0.381025
5	0.038102

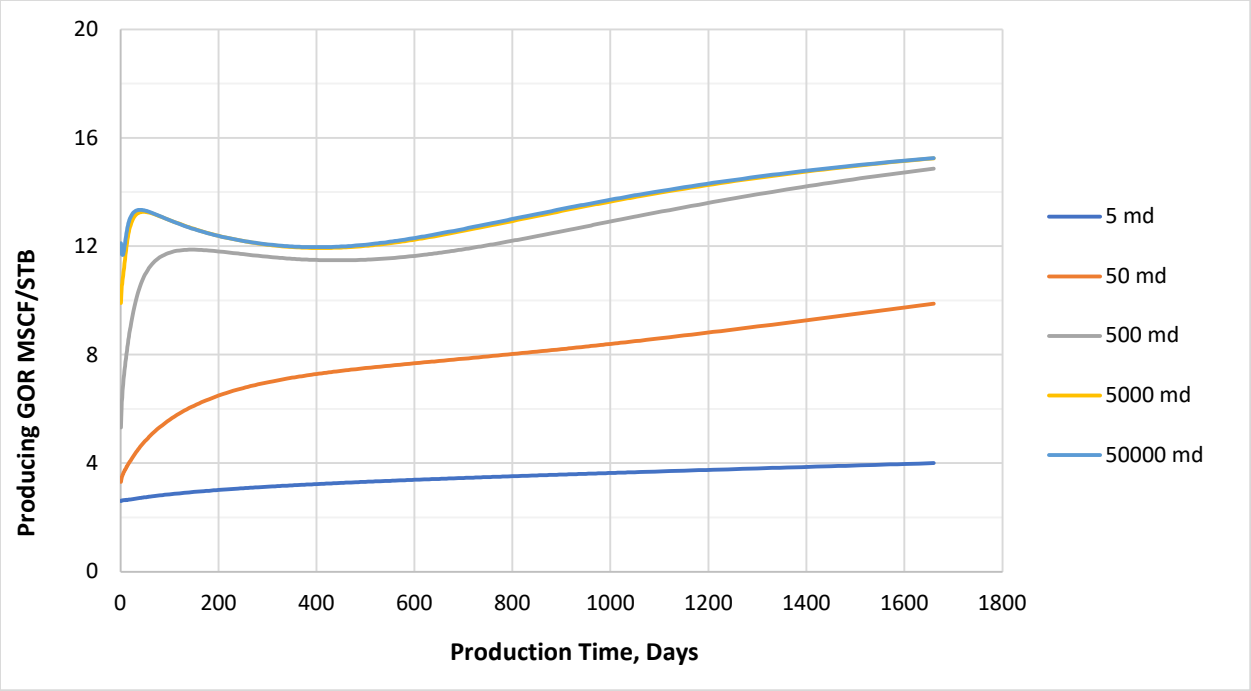

Figure 44. Dimensionless fracture conductivity trials forecasting, GOR vs days

Both 5,000 md and 50,000 md have the exact same GOR trend, which is a good indication that in terms of GOR forecasting, 38 F_{cD} can be considered infinite conductivity. The trials of 500, 5,000, and 50,000 md all follow the typical case of a sharp increase in GOR followed by an extended plateau period.

The 50 md trial has very low conductivity so there does not appear to be a plateau; Jones called this an ascending plateau. This means that between a F_{cD} of 0.3 and 3, the GOR trend will shift from having a plateau to not having one. The difference between a F_{cD} of 3 from .3 is much larger than a F_{cD} of 30 to 3. Fine tuning the fracture permeability is difficult once the cutoff is met.

When the permeability of the fracture is 5 md, the GOR is completely flat just above R_s, this is caused by fracture failing to produce anything significant from the reservoir.

The difference in the GOR trend between a well with infinite conductive flow and finite conductive flow will be discussed further in section 3.4.

3.3 Isotropic Stress-dependent Permeability Effects on GOR

Now it is time to see the change of the fluid transport associated with the permeability reduction associated with pressure depletion causing the system to experience stress.

The permeability of the system and its stress dependency has a major effect on the GOR. In order to test this relationship, the dimensionless fracture conductivity was kept constant at 38.1 and a multiplier was applied to the matrix transmissibility. This means that all the trials done in this section start off with infinite conductivity. For the first round of trials, the multiplier was held constant for the duration of the simulation run, but for the second round of simulations, the permeability was kept stress-dependent.

For the constant permeability trials, the original fracture permeability and the matrix permeability of 5000 md, and 0.05 md respectively, are multiplied. So, if the multiplier is 0.54, then the permeability values will be 2700 md for the fracture and 0.027 md for the matrix. The results of the constant permeability trials are shown in **Figure 45**.

The point of having these constant permeability trials, is to have a frame of reference for the stress sensitive trials. These constant permeability trials should give me a snapshot on the particular multiplier's effect on the GOR trend. The smaller the multiplier, the longer it takes for the production to reach the next stage of production of GOR. The lower the multiplier, the more reduction in the permeability. The multipliers of 0.039, and 0.027 have a flat period in the beginning lasting several hundred days before going to the 13.5 MSCF/STB. This can help explain the phenomenon in **Figure 1**, where there is a flat period, and then it starts to increase a few hundred days in.

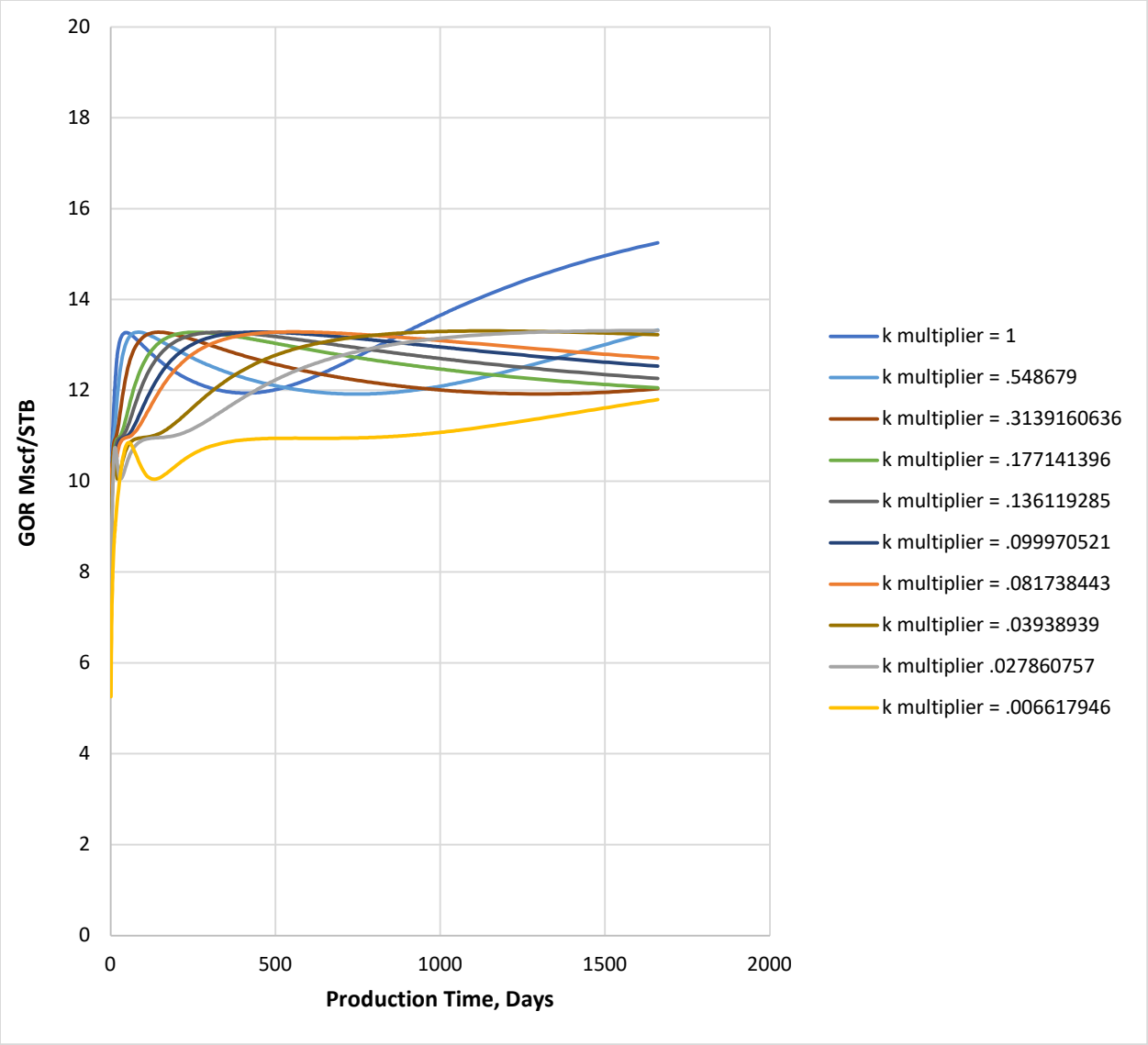

Figure 45. Constant permeability trials, isotropic case. Tight rock

The transmissibility multiplier of 0.0066 is the only multiplier that did not have an initial peak of 13.5 MSCF/STB when fracture interference developed. This means, when put under enough stress, the gas loses its mobility. If shale has a low resistance to closure, and is already under a lot of stress then the gas mobility of the system will not increase. The trend to look for is that the lower the multiplier, the flatter the GOR can be expected at any moment.

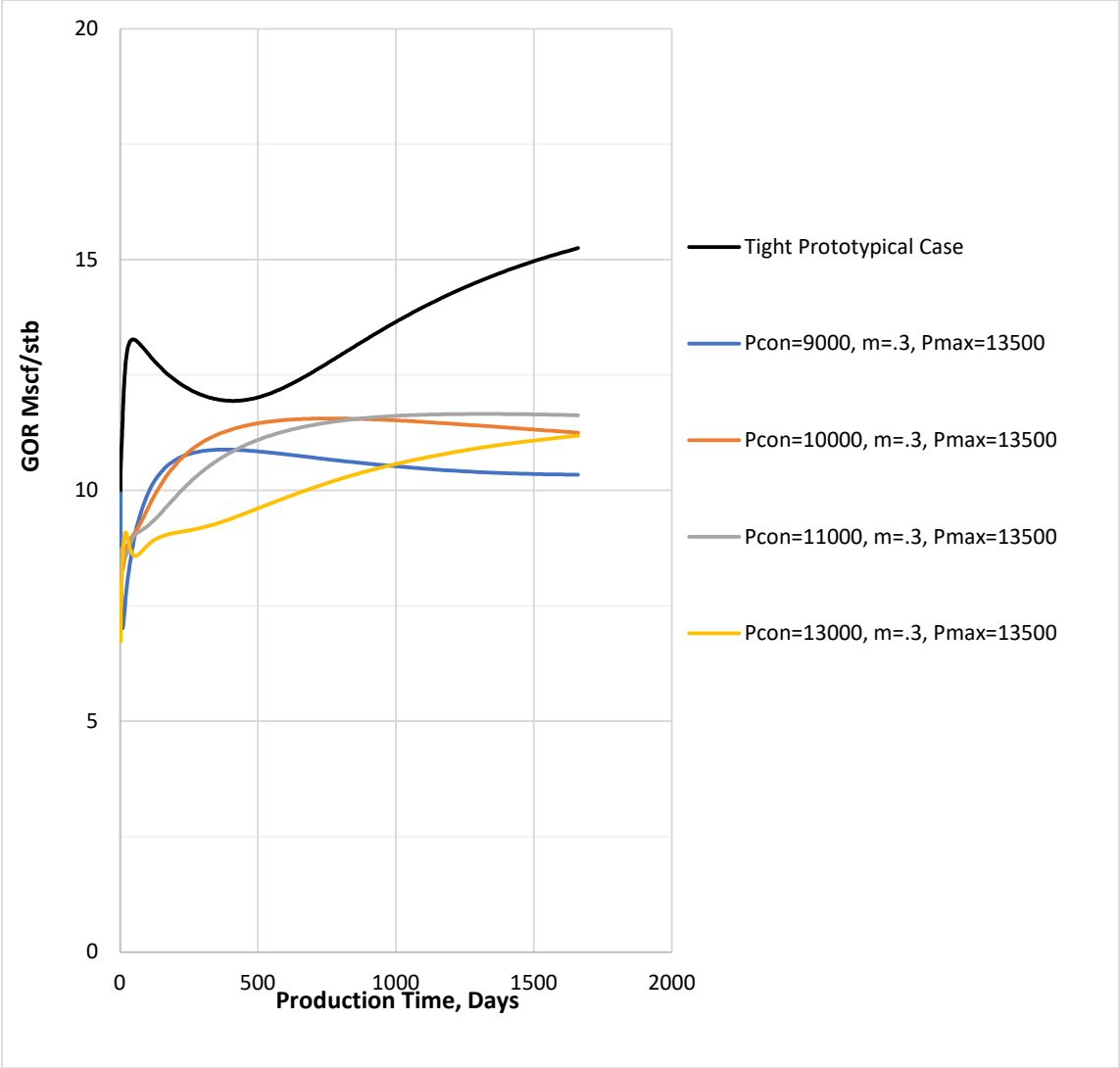

Figure 46. Dynamic permeability trials, isotropic case. Tight rock

The isotropic permeability trials were run with the transmissibility multiplier being stress-dependent, where the multiplier followed Gangi's equation. The results of some those trials are shown in **Figure 46**.

The dynamic permeability trials were compared to the constant permeability tight rock model. The permeability model used the following Gangi parameters, m=0.3, P_{max} =13500, and P_{con} ranging

from 9000 to 13000. These are all acceptable parameters for shale according to Wasaki and Akkutlu (2015). The stress dependence of the permeability has closed the fractures and cracks enough that none of the models reach the initial peak of 13.5 MSCF/STB. The GOR has quantitatively been lowered by the permeability reduction, for example at day 100 of production the GOR is 8.8 MSCF/STB, when the confining pressure is 13,000 psi, while the prototypical tight case is 12.96 MSCF/STB. This is a 32% reduction in the GOR caused solely by the permeability stress dependency. Stress is causing damage in the fractures which is preventing the gas from mobilizing like it does tight prototypical case.

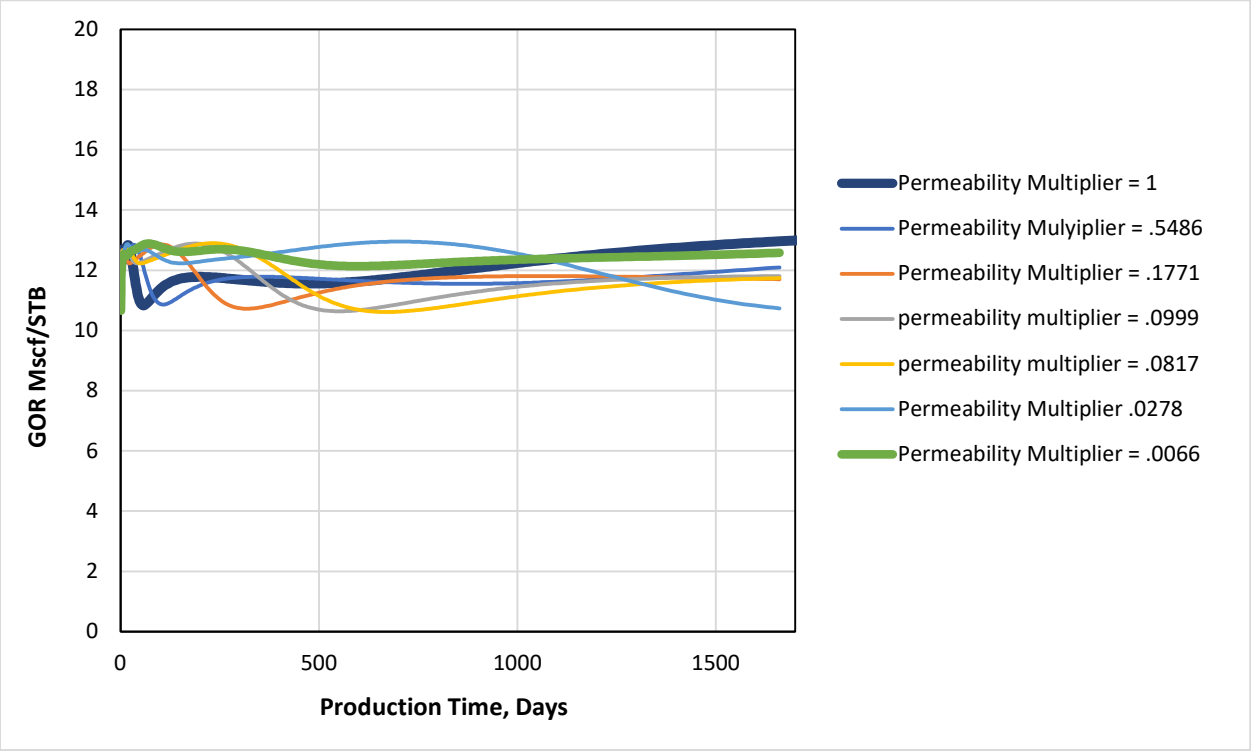

Figure 47. Constant permeability multiplier trials for the Ultratight reservoir

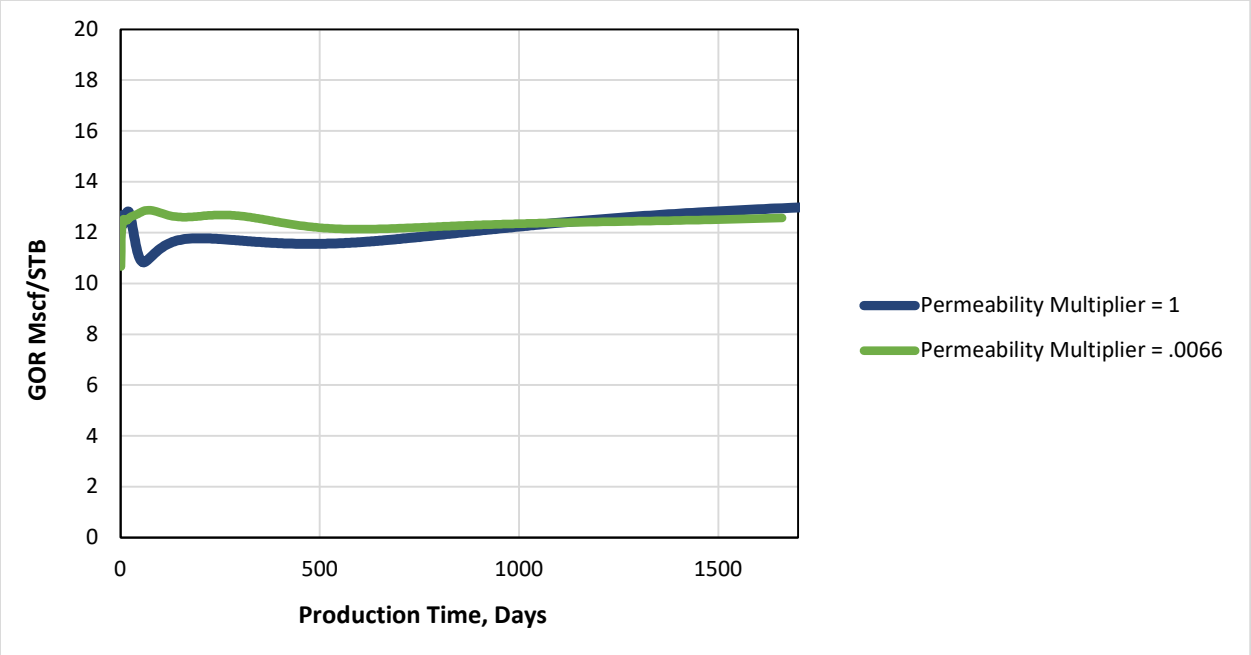

Figure 48. Constant permeability multiplier trials for Ultratight reservoir, only the extreme multipliers of 1 and .0066.

In the ultra-tight cases, the smaller the permeability multiplier does not lead to a more suppressed GOR, **Figure 47**. Instead, what seems to be the case is that the lower the permeability multiplier, the flatter the forecasting says the GOR will be. This is an indication that there is a limit to how much stress will affect the GOR through the permeability, and the higher the initial permeability, the more vulnerable it is to the stress affects.

3.4 Anisotropic Stress-dependent permeability effects on GOR

Now that it is shown that stress dependence of the permeability has the ability to affect the GOR trend, it is now important to measure the impact of the stress effect on the matrix and hydraulic permeability individually to see which contributes more. This is important to study as seen in Kim and Akkutlu (2019), the permeability properties of the matrix and fracture cells are significantly different from each other. The hydraulic fractures are propped, and their confinement

pressure is based on the $\sigma_{h,min}$. This leads to the Gangi equation parameters to be significantly different. An example of optimized parameters is in **Table 7**. Part of this analysis will be comparing the GOR trends when the flow is initially at infinite conductivity, FcD is 38, and when it is initially finite, FcD is .38.

In order to test this, these parameters were used in a series of trials where in the first trial both cell type were run stress dependent, then in the second trial, both cell types were run as independent of stress, and the final two trials were run where only one cell type was run constant and the other stress dependent.

Table 7. Gangi parameters for fracture and matrix parameters.

Parameter	Value	Unit
Matrix porosity	0.12	fraction
Fracture porosity	0.667	fraction
Fracture permeability parameter k_{f0}	5.0 or .05	D
Fracture permeability parameter, □	13500	psi
Fracture permeability parameter, M	0.277	-
Biot coefficient, α	1.0	-
Matrix permeability parameter, k_{m0}	5.00E-05	D
Matrix permeability parameter, p_1	27,927	psi
Matrix permeability parameter, m	0.118	-
Overburden stress, σ_{ob}	12,000	psi
Minimum horizontal stress $\sigma_{h,min}$	10,000	psi

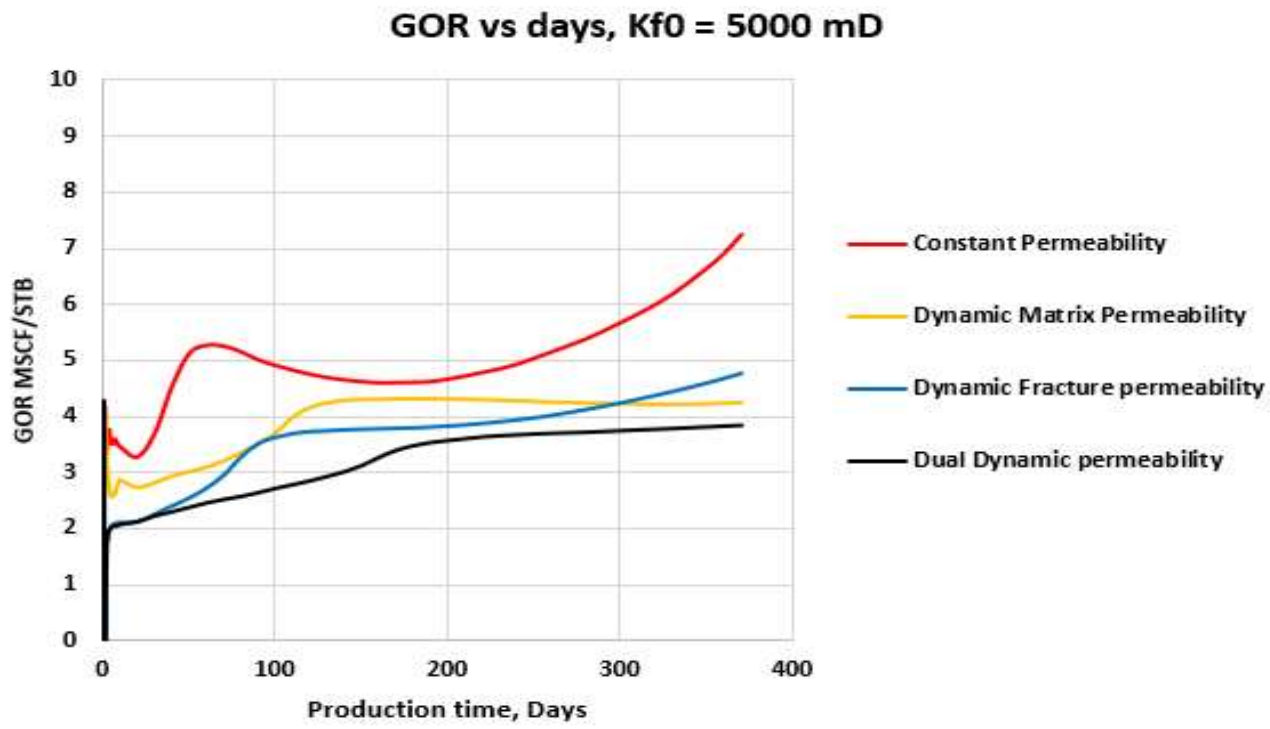

Figure 49. GOR vs time, anisotropic Stress-dependent permeability trials when flow is infinite conductivity

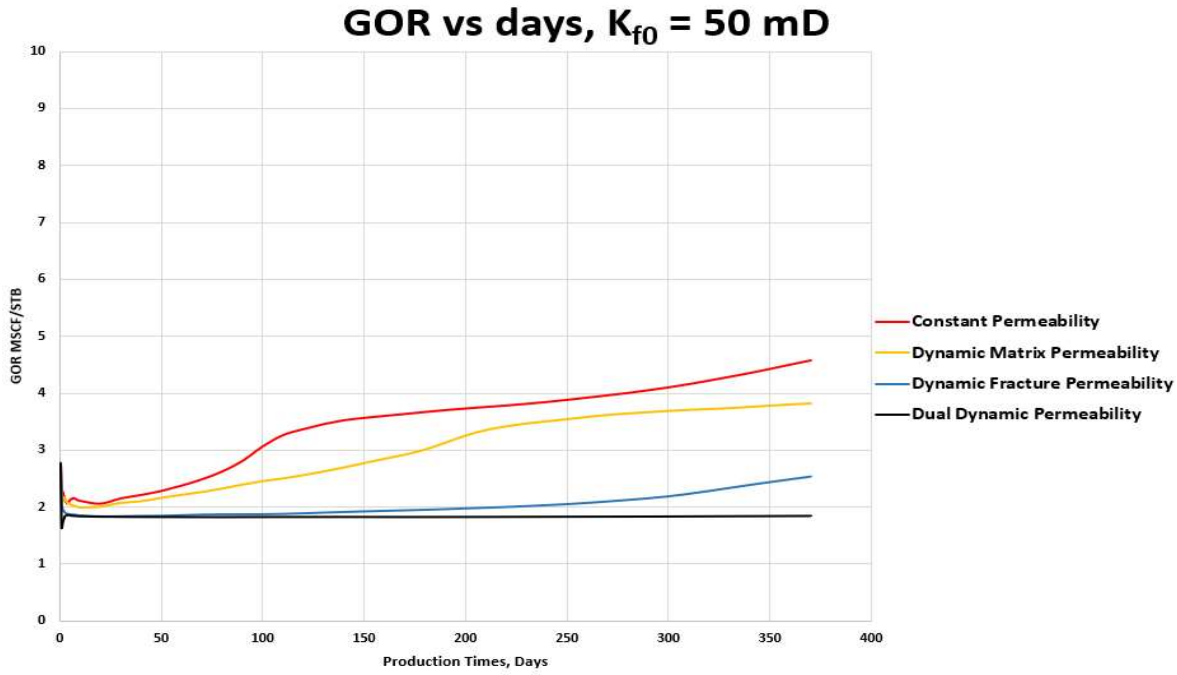

Figure 50. GOR vs time, anisotropic Stress-dependent permeability trials when flow is finite conductivity

The GOR forecasting of the four trials run for the anisotropic Gangi parameters are compared for the infinite conductivity and finite conductivity models, **Figures 49 and 50**. In this dual permeability and porosity system, the fluid flow is controlled by both the matrix and the fractures because all the fluid is stored in the matrix and needs to be transported to the fracture to get to the wellbore. In this fluid transportation system, both the matrix and the fracture need to be open to flow and if one starts to fail then there will not be fluid flow. This does not mean that both parameters have equal contribution of the flow. The simulation was run for 1 year because that is when most of the production happens.

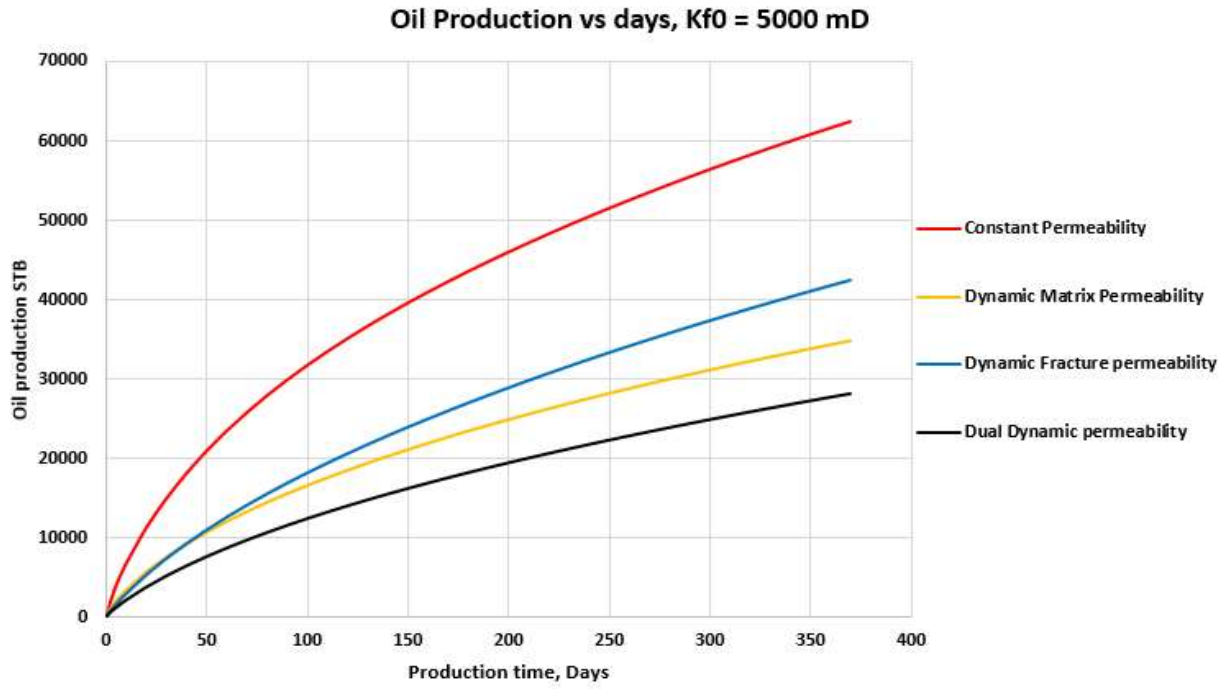

Figure 51. Oil production, anisotropic study, infinite conductivity

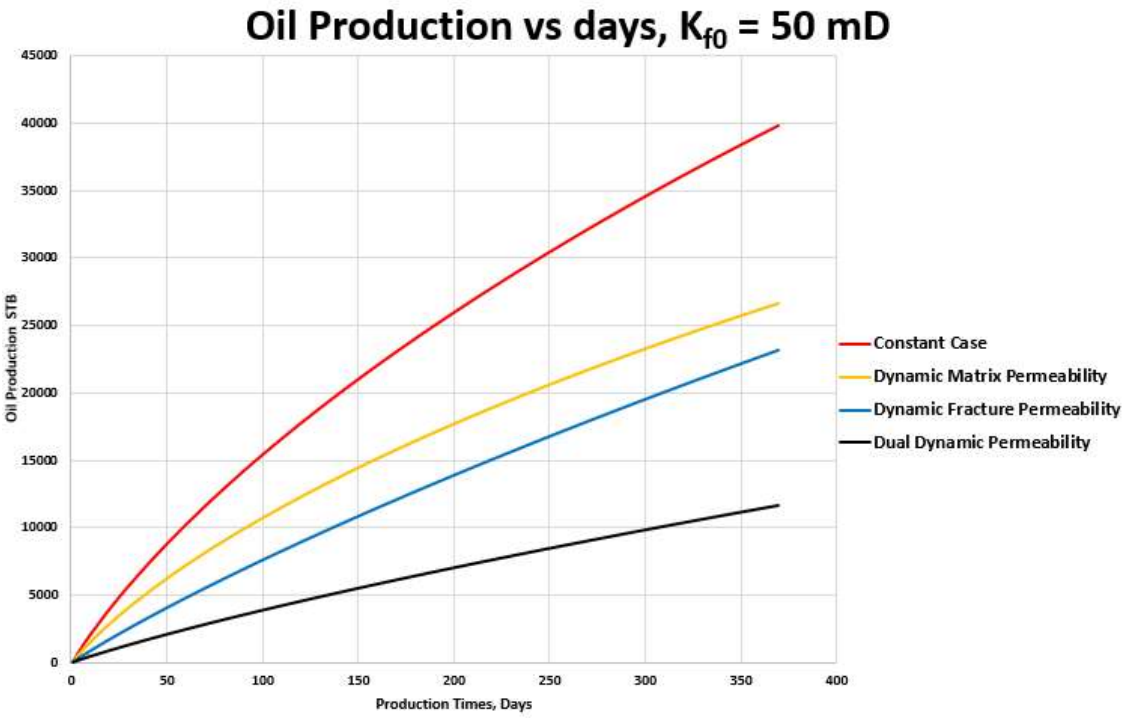

Figure 52. Oil production, anisotropic study, finite conductivity

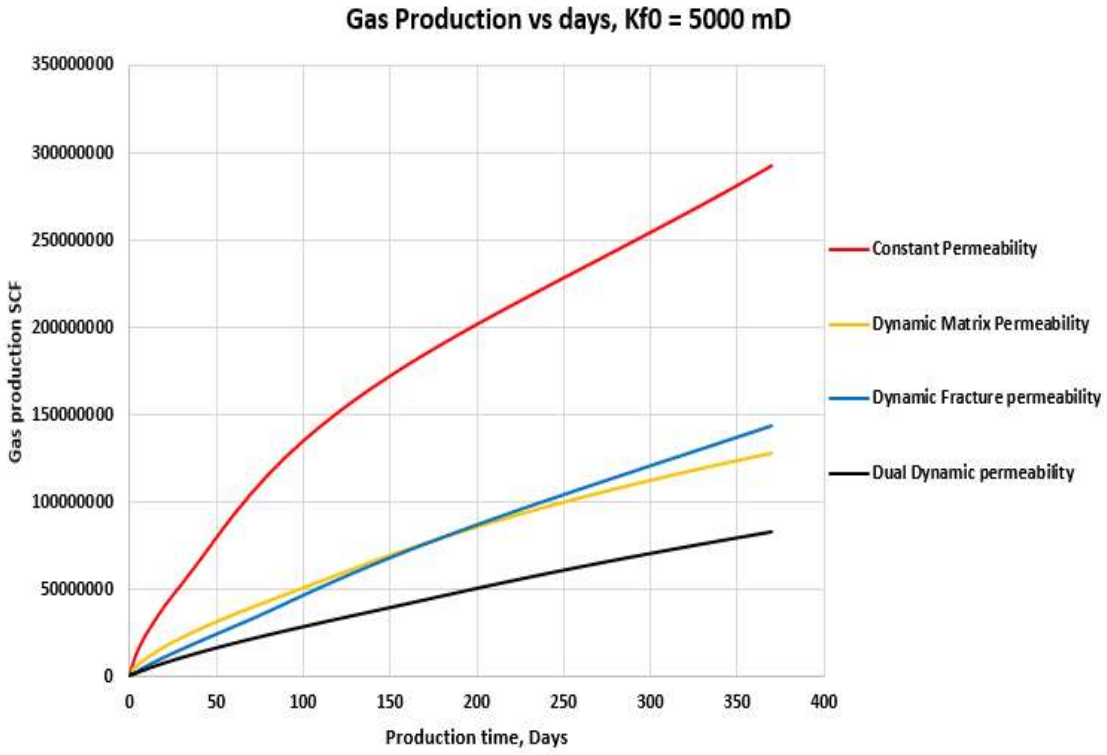

Figure 53. Gas production, anisotropic study, infinite conductivity

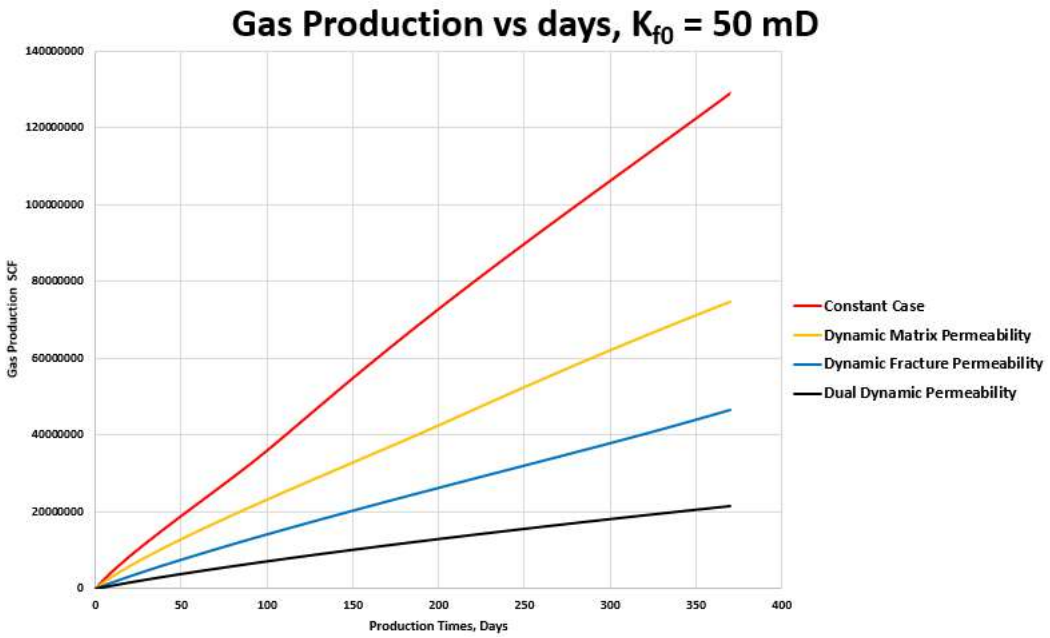

Figure 54. Gas production, anisotropic study, finite conductivity

Comparing the infinite and finite models' production trends reveals important information on the mobility of hydrocarbons in different situations. First to look at the GOR trends themselves, we can see that permeability reduction will cause a reduction in the GOR and make the trend flatter. This follows the same trend as the isotropic trial, so there is no surprise there.

The infinite conductivity case shows that only having the fracture permeability or matrix permeability be stress dependent will cause a significant drop in GOR, but because the fracture has infinite conductivity, it will not completely close from the stress, and the GOR will not be completely flat, **Figure 49**. The oil production data shows that when the matrix permeability is stress dependent and the fracture is not, the oil production goes down more than when the fracture is stress dependent, **Figure 51**. For gas production, stress dependency for the matrix and fracture permeability effects the system equally, **Figure 53**. This furthers the point that when the well experiences infinite flow, the fracture can experience some amount of closure and resist dropping in production.

When the fractures are finite in conductivity, the stress dependency in the fractures causes significant closure, and causes almost complete flatness in the GOR. Comparing the GOR trend when the permeability is held constant, and if there is stress dependency in the system, it shows that the GOR reduction is almost completely from stress dependency in the hydraulic fractures, **Figure 50**. From the production data, making the fracture stress dependent greatly reduces the flow both for oil and gas, while it doesn't for the matrix stress dependent case, **Figures 52 and 54**. This shows if the fractures have finite conductivity, then the fractures closing will prevent the gas from releasing and flowing through to the well.

This is an indication that more time and effort should go into mapping and understanding the nature of hydraulic fractures than the matrix in terms of permeability. The stress in the fractures constricts the mobility of the gas. This is caused by the initial hydraulic fracture being open and approaching pipe-like flow then being shut in, while the matrix permeability is already effectively constricting fluid flow because of its low permeability.

3.5 Pore Compressibility and Porosity effects on GOR trends

Now that the fundamental interaction between fractures and the matrix has been mapped out. This study done on pore compressibility is when the initial fracture permeability is 5 D, infinite conductivity.

The GOR's magnitude becomes smaller and the trend becomes flatter as the compressibility coefficient is taken larger, **Figure 55**. as I explained in the introduction, the nature of pore compressibility of shale is such that, at the beginning of production the compressibility is large, close to 1.0E-4 1/psi; as the production continues, the compressibility factor becomes much smaller, down to 1.0E-6 1/psi. This can lead to a situation where the GOR will slightly increase as

the compressibility factor changes. Unfortunately, in my simulation the compressibility is constant, but **Figure 55** shows the trends for the whole range of values.

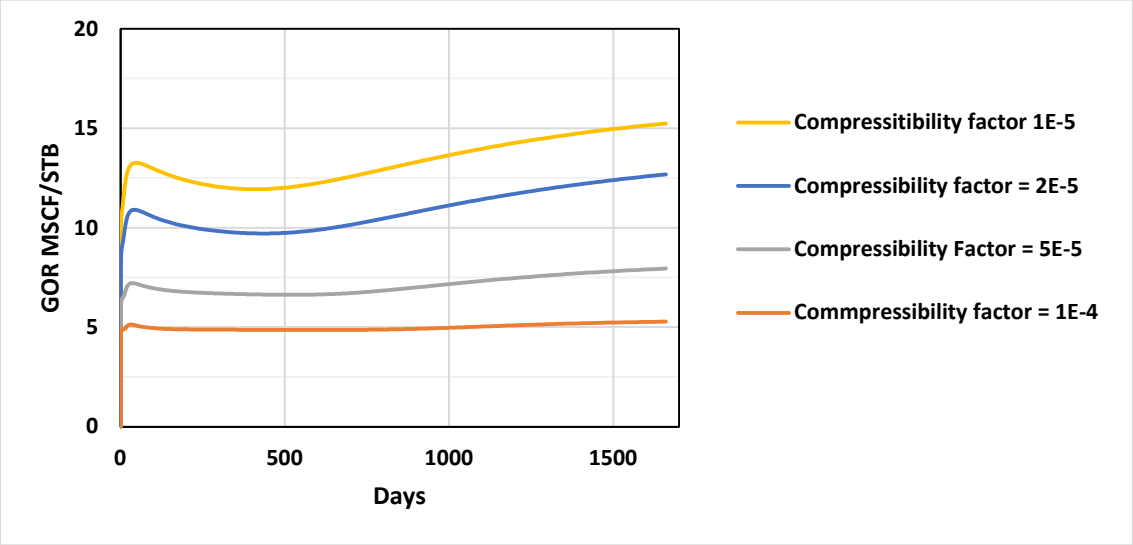

Figure 55. GOR vs time, Compressibility trials for the tight matrix case.

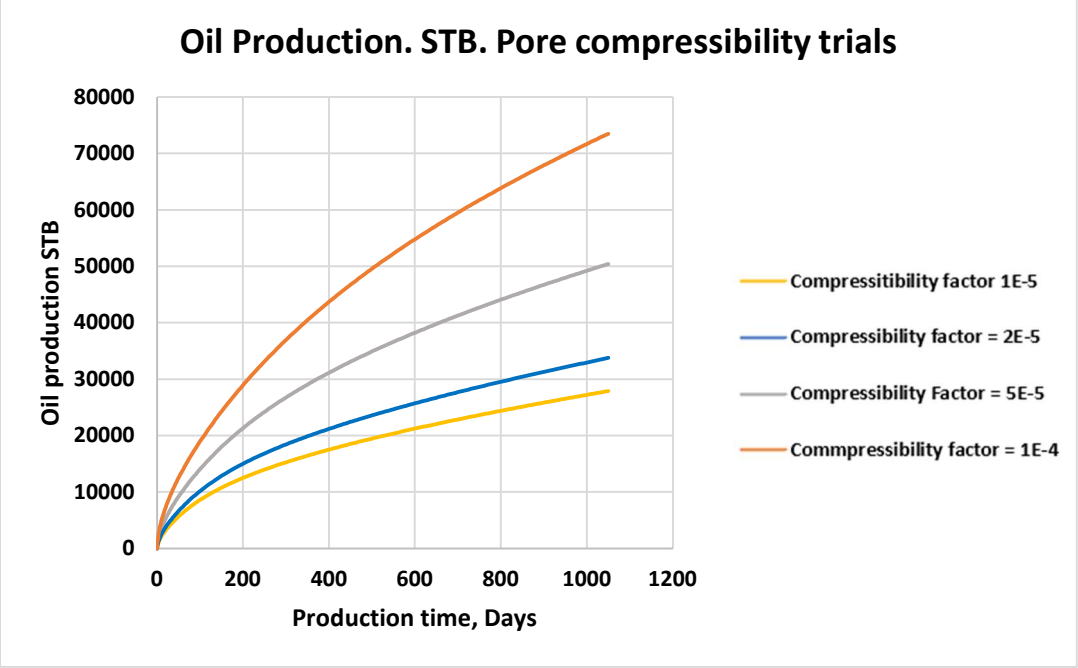

Figure 56. Oil production, compressibility trials for the tight matrix case

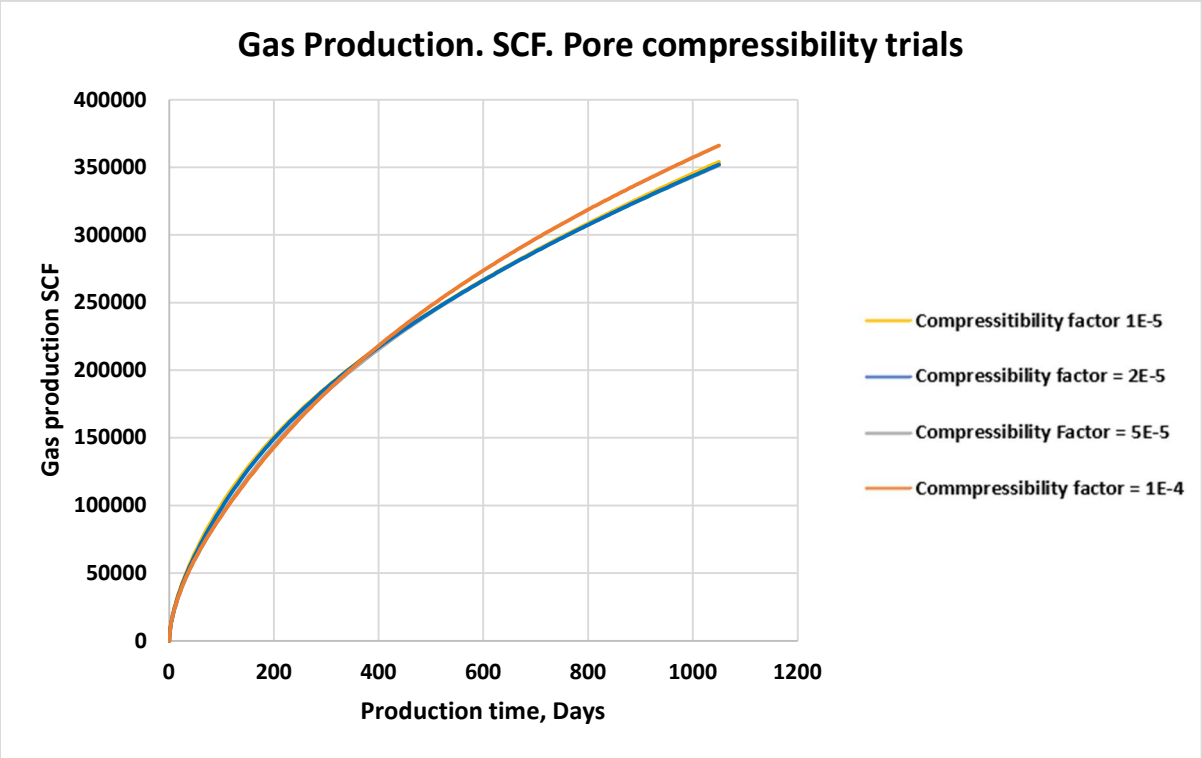

Figure 57. Gas production, compressibility trials for the tight matrix case

The reason for the GOR decrease with the compressibility increases is because with the increasing compressibility, the pore volume is reduced additionally during the depletion. Increasing the pore compressibility increases the oil rate without increasing the gas rate, **Figure. 56-57**. This is a stark difference between the pore compressibility trials and the permeability reduction trials, because the permeability trials reduced both the gas and oil rates. The larger pore space reduction means less space available for the release of gas from the oil and for the expansion of the free gas. It is basic application of the conservation of mass, if oil and water flow out of the rock unit due to production, then voidage created by the flowing out fluids must be filled up by the components of the reservoir system. In a rigid reservoir system, the voidage created by the flow would be taken up by the expansion of the oil and water phases and by the gas released from the oil. But, if the reservoir is not rigid, the rock compaction also participate into this effort and

pore volume will be reduced. This reduction in the pore space is adding energy to the system that is supporting fluid flow, which is typically supported by gas expansion. This consequently leads to less gas release. So, the compressibility increases causes pore volume reduction, and therefore reduction in gas released from oil. This is shown in Table. 6, where the gas saturation is 10-16% for the lower compressibility case, and 10-11% for the high compressibility case. This 5% difference in the value of the gas saturation is attributable solely to the change in the compressibility value. In the high compressibility case, the oil saturation actually increases from 59% saturation to 61%, during the production, while in the low compressibility case it decreases from 59% to 55% during the production. The effect of pore compressibility is somewhat less on the water saturation: in the high compressibility case decreases from 30% to 27%, and in the low compressibility case it decreases from 30% to 28%. This is due to low compressibility of the water. During the expansion of the reservoir system components the water expansion is almost negligible.

Table 8. Saturation data, max and minimum for the compressibility case and high compressibility case

• low compressibility case -------- High Compressibility Case

Saturation	Low	high
Oil	0.55	0.59
Water	0.28	0.3
Gas	0.1	0.16

Saturation	Low	high
Oil	0.59	0.61
Water	0.27	0.3
Gas	0.1	0.11

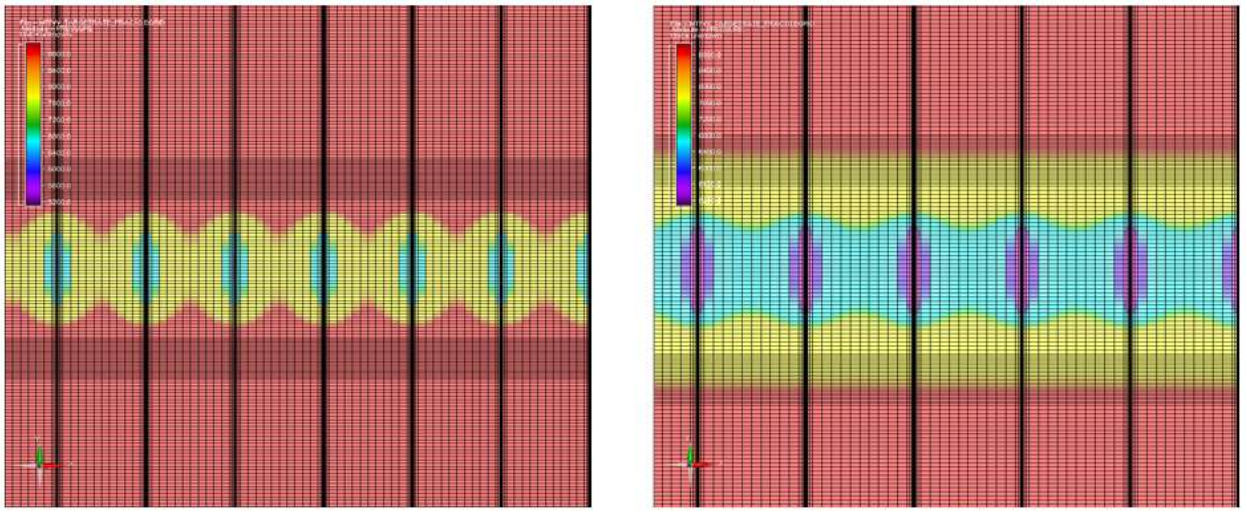

Figure 58. 15 days of production, pressure profile, High compressibility on the left, low compressibility on the right.

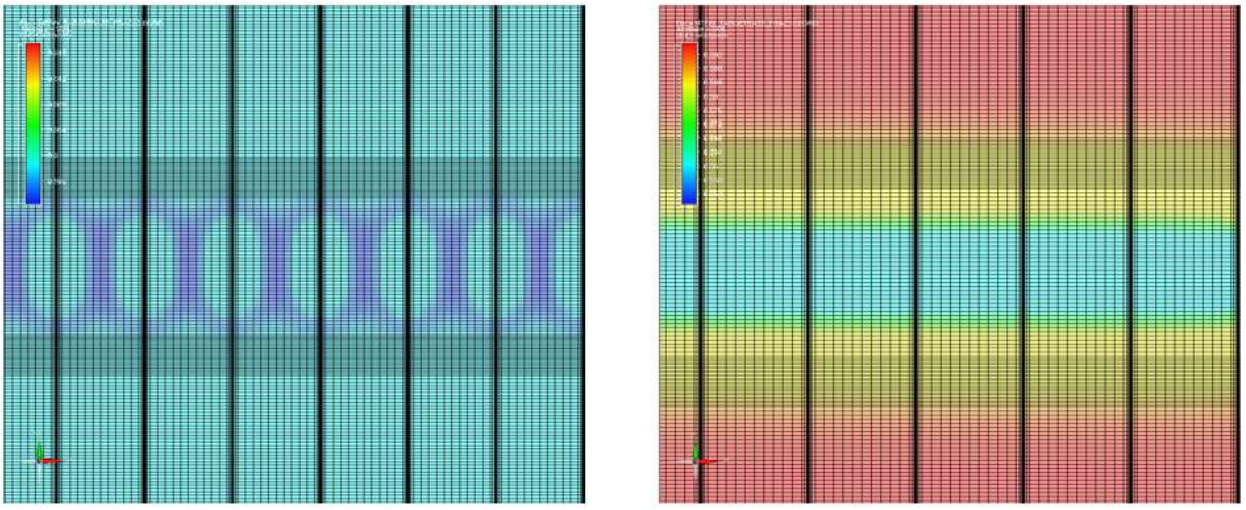

Figure 59. 15 days of production, oil saturation, high compressibility on the left, low compressibility on the right

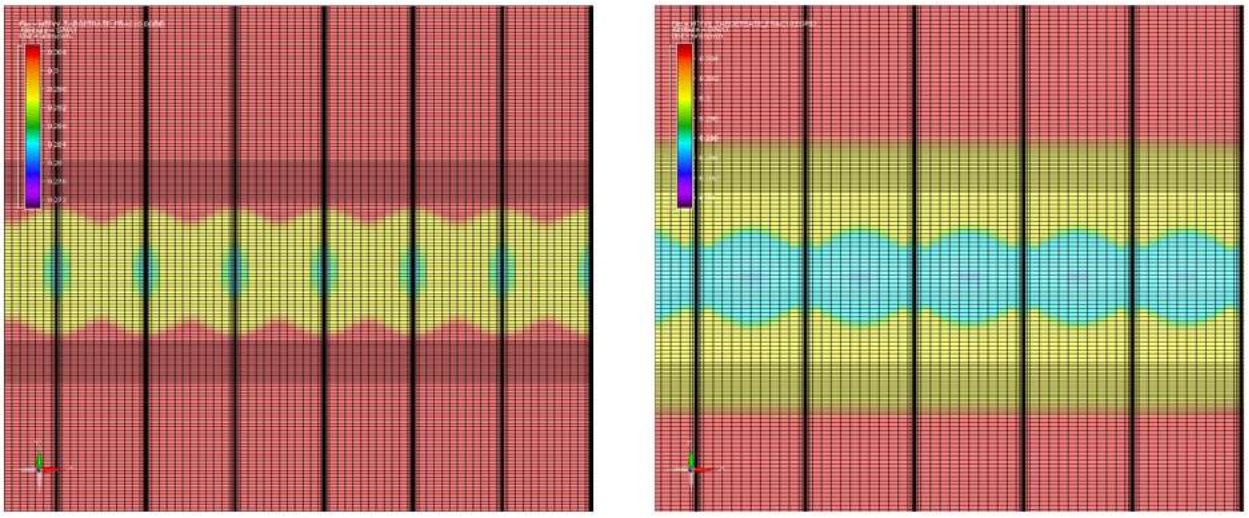

Figure 60. 15 days of production, water saturation, high compressibility on the left, low compressibility on the right

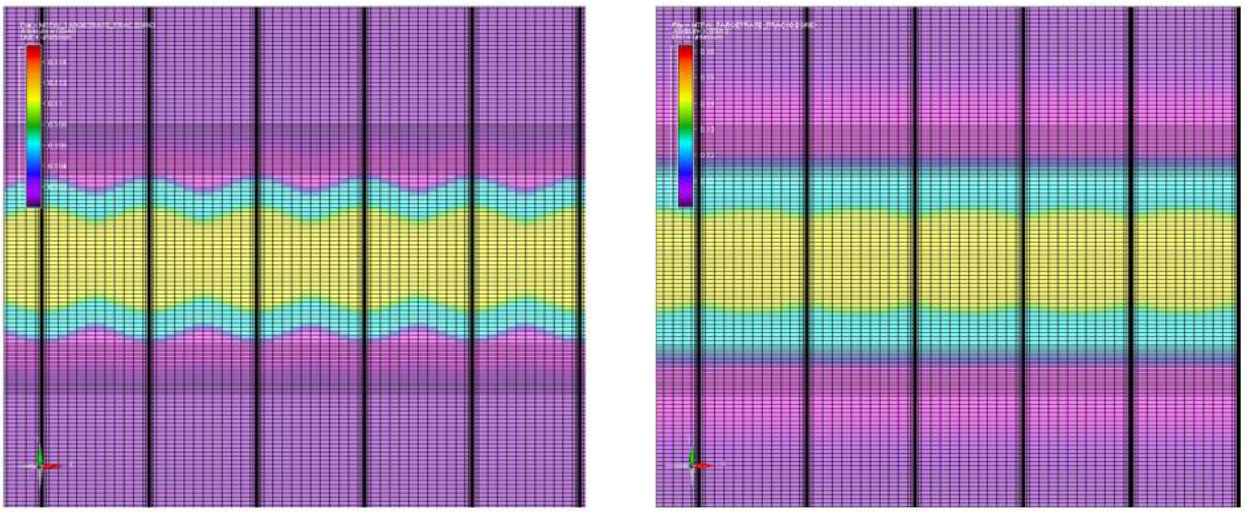

Figure 61. 15 days of production, water saturation, high compressibility on the left, low compressibility on the right

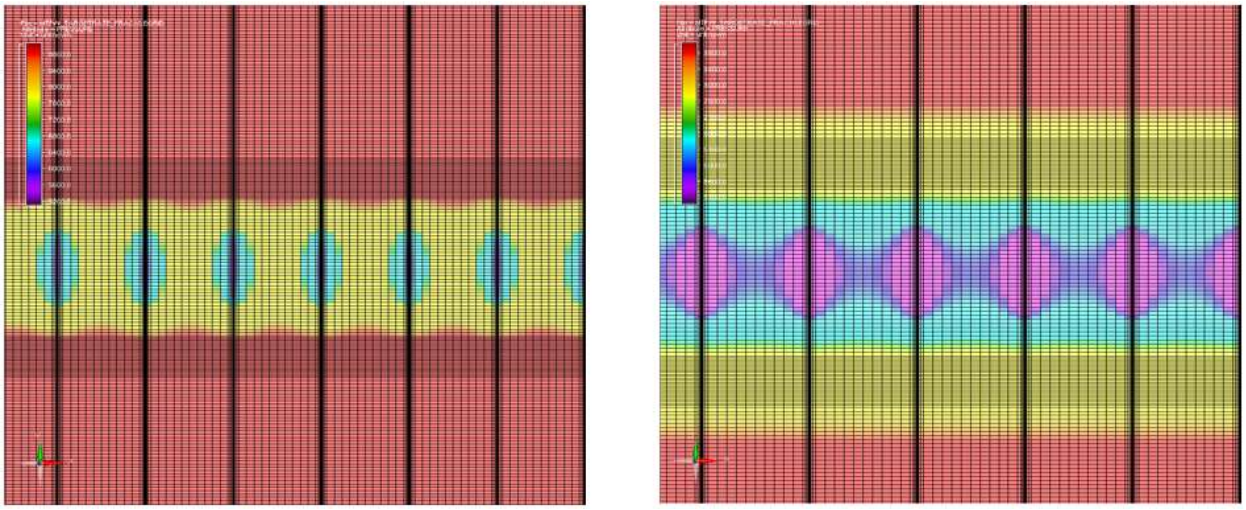

Figure 62. 28 days of production, pressure profile, High compressibility on the left, low compressibility on the right.

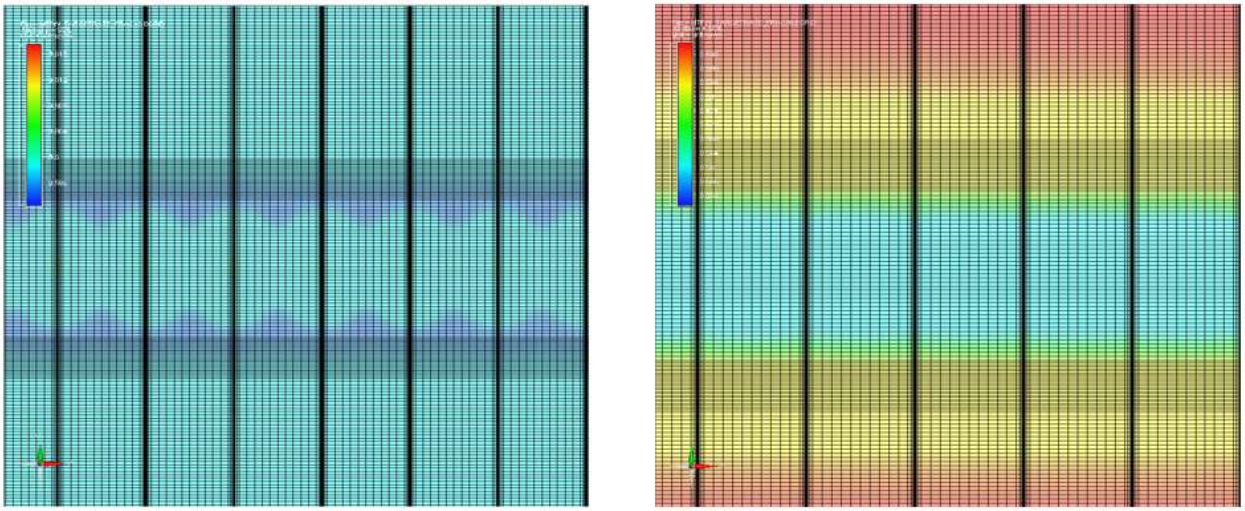

Figure 63. 28 days of production, oil saturation, high compressibility on the left, low compressibility on the right

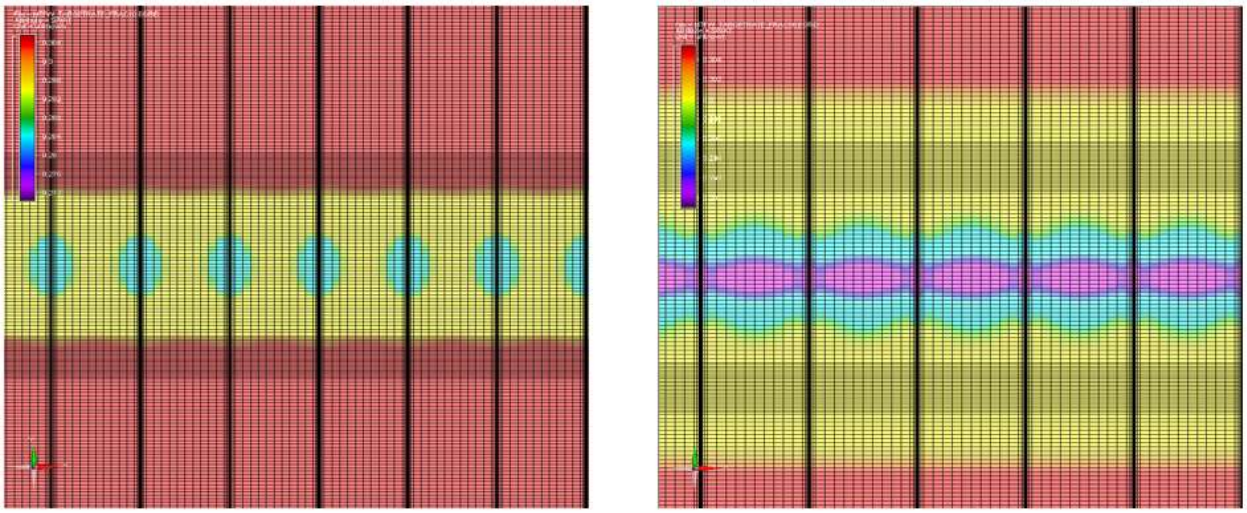

Figure 64. 28 days of production, water saturation, high compressibility on the left, low compressibility on the right

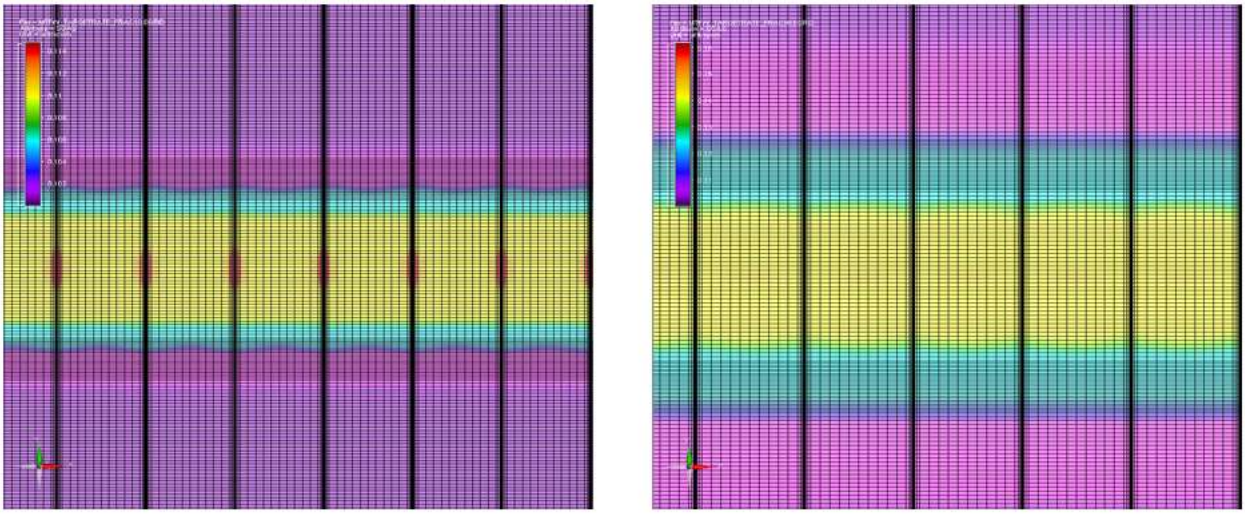

Figure 65. 15 days of production, water saturation, high compressibility on the left, low compressibility on the right

It is important when looking at **Figures 58-65**, that the color index does not match the same saturations value, but instead match the same production stage. The colors, however, do match for the pressure maps. The saturations maps and the pressure maps show that the saturations change farther than the pressure profile goes.

Between the high-compressibility and the low-compressibility cases, a cell with the same pore pressure will have different saturation data. the portion of the reservoir that is in the blue zone is at 6600 psi. However even though both reservoirs can be 6600 Psi in some spots, both reservoirs are in the yellow zone of gas saturation, which for the high compressibility model means it is at 11% gas saturation, and in the low saturation model it is at 14%, **Figure 58** and **61**. In the high compressibility case, there is a layer of low oil saturation near the outskirts of the pressure zone, and then the oil saturation increases near the fractures, **Figure 59** and **63**. So as the water is being produced, there is less water, but as the oil is being produced, it also causes a build up near the fractures, and this oil build up coupled with the pore volume reduction is preventing gas saturation from evolving out of the oil to increase the gas saturation.

Not only is there a restriction in the gas coming out of the oil, but as a consequence of the pore compressibility, I observe the free gas could also dissolve back into the oil phase, ie., exsolution. When the GOR trend shows its local maximum, the gas saturation inside the fractures also reaches its local maximum. When the gas saturation in the fracture goes back down due to exsolution, so does the GOR trend. The exsolution of the gas is caused by the fracture closure stress. In the low compressibility case the exsolution gas forms near the fracture and the entirety of the well bore, with this phenomenon being documented in other types of reservoirs, (Opperts paper). The reason for the low compressibility case has the gas exsolution follow the wellbore is twofold: the first being the rigidness of the rock allows the gas to move more freely, and secondly the well bore is producing at all parts in the simulation so there is a small amount of draw not based in the fracture.

An interesting comparison of the low and high compressibility cases is the length of time it takes for the exsolution to appear and then disappear. At 35 days of production, both cases are

starting to see their peak gas saturations but by day 70 the high compressibility case the high saturation zone is gone, while it takes over a year for the low compressibility case for the high saturation zone to disappear.

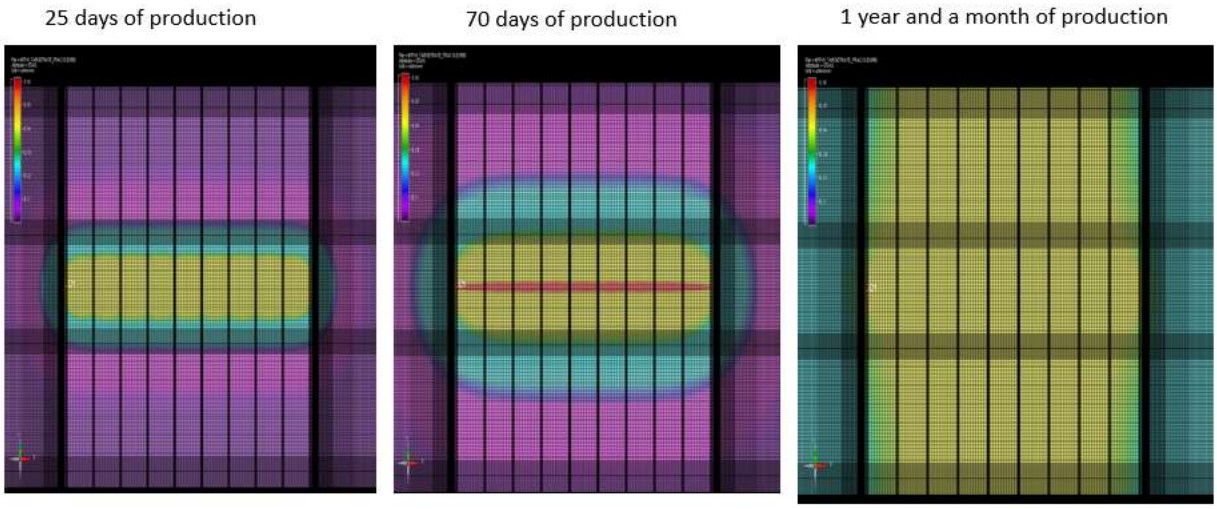

Figure 66. Saturation maps of low compressibility trials, at days 25, 70 and 395 days

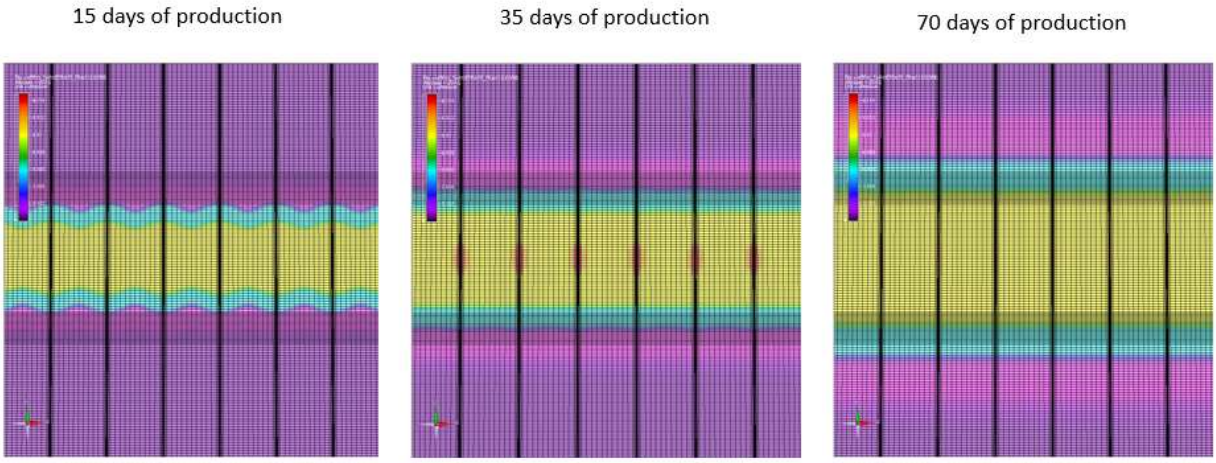

Figure 67. Saturation maps of High compressibility trials, at days 15, 35 and 70 days

The low compressibility case is not likely to develop because of the non-static nature of shale reservoirs, due to high-compressibility in the early stages of production and low-compressibility in the later stages.

the maximum gas saturation is observed during the first few months of production and eventually disappear, as the fractures close during the production, **Figure 66** and **67**. The higher compressibility case has less exsolution gas because high compressibility prevents gas from leaving the oil in the first place.

The pore volume compressibility has a large effect on the GOR, which is attributable to the change in saturation data. A series of trials testing different starting porosities, were conducted to make sure that the compressibility effect is present in reservoir with little porosity to begin with. The porosity trials can be seen in **Figures 68-69**. They were run for both the tight and ultra-tight models.

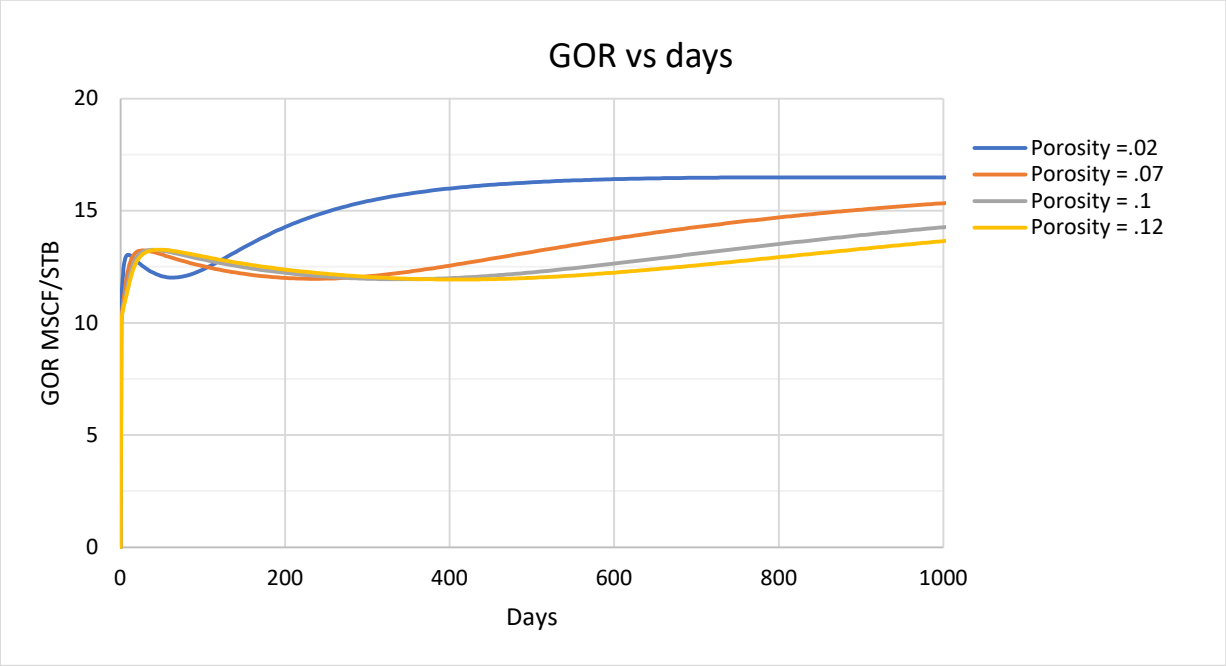

Figure 68. Porosity trials for the tight matrix, c_p = 1.0E^{-5} psi^{-1}

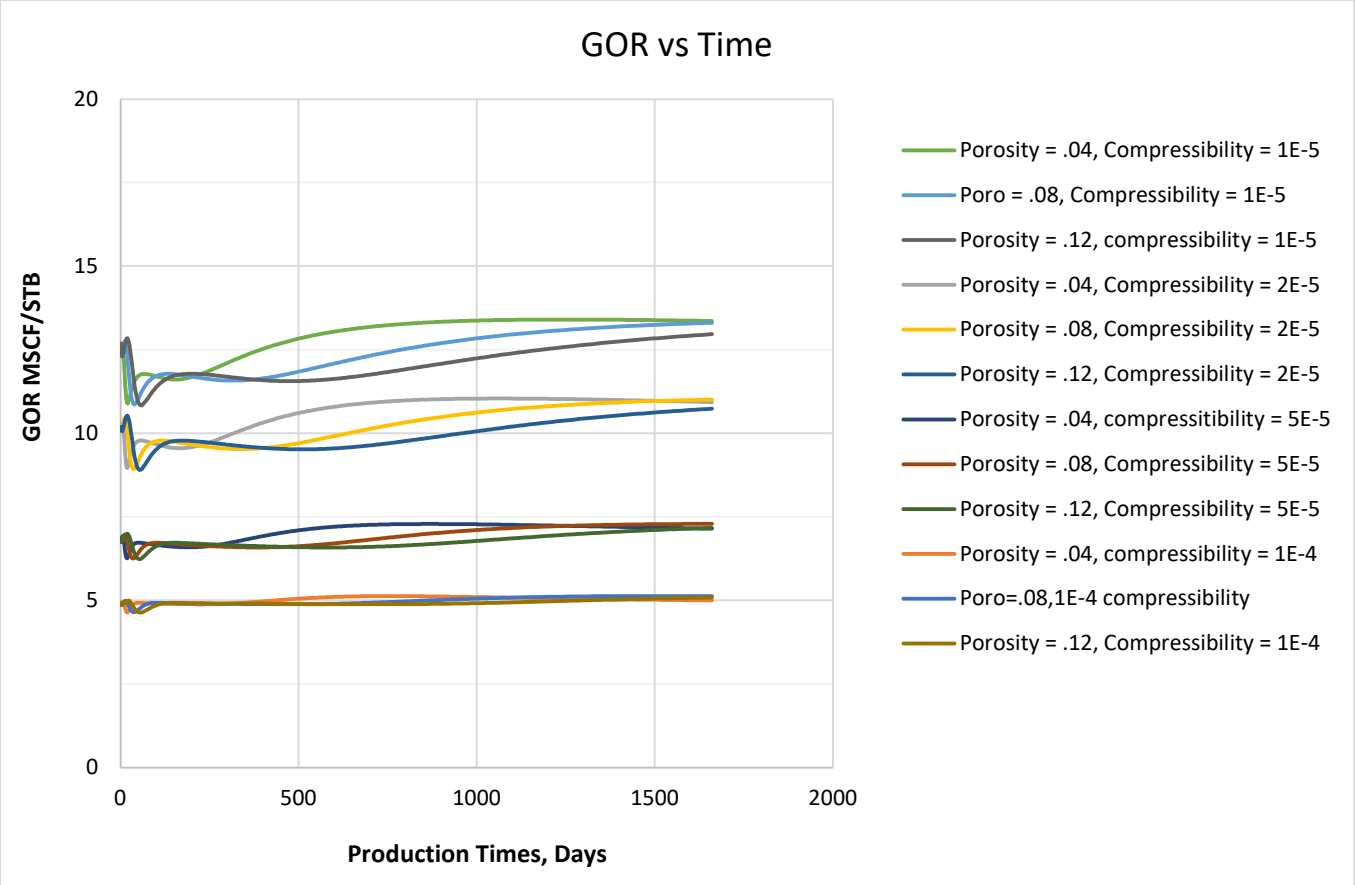

Figure 69. Porosity trials for ultra-tight matrix.

In both these trials, the lower porosity, the shorter the time it takes for production to reach the next stage. The porosity does not have a major effect on the plateau of the GOR just the time it takes to get to a GOR value; the tight matrix is more influenced by any porosity affects; the higher the compressibility the less the porosity affects the GOR, **Figures 68-69**.

3.5 Anisotropic Stress Field effects on GOR

The anisotropic nature between the hydraulic fractures and the matrix have been tested, and been shown to matter significantly. The anisotropic stress field of shale leads to the confinement stress for the hydraulic fractures to be different from matrix cracks, and this has not

been tested yet. Taking from Ankush (2019), when the vertical stress is 12000 psi, it is expected that the minimum horizontal stress will be at least 10000, for the shale stress field Ankush tested. NaSh was used to run both an isotropic case where both overburden stress and the σ_{hmin} where at 12000 psi, and an anisotropic case where the overburden was 12000 psi and the σ_{hmin} was 10000 psi. the results are in **Figure 70-71**.

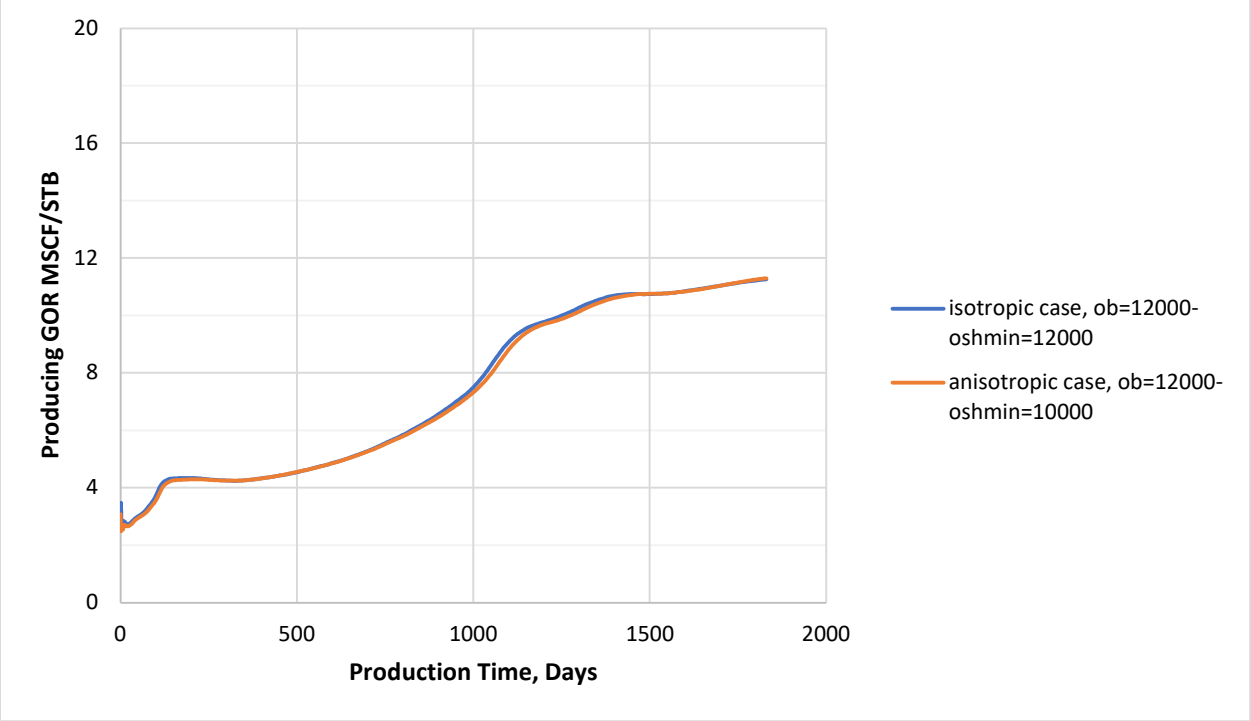

Figure 70. anisotropic effects on confinement stress

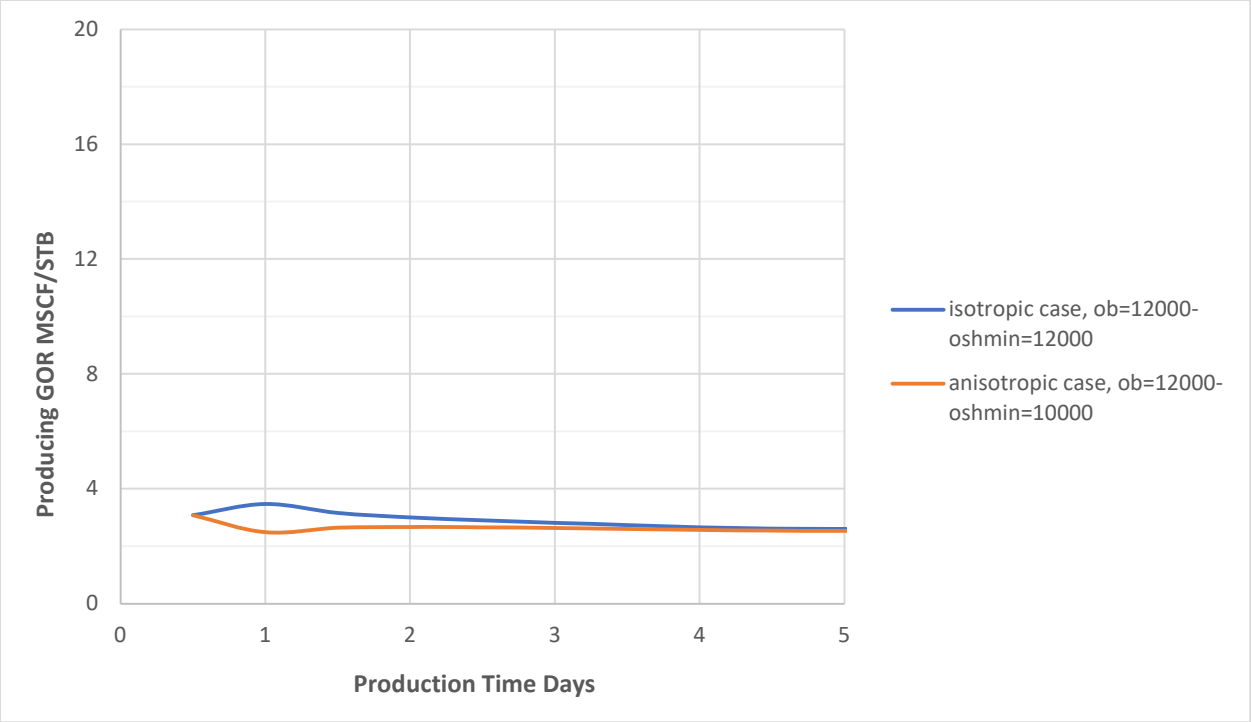

Figure 71. anisotropic effects on confinement stress for the first 5 days.

The biggest difference seen in is in the first day of production, where there is a 1000 SCF/STB difference in GOR, but by day 4, the difference in GOR is only 40 SCF/STB. The trend for the anisotropic case also is going downwards and not increasing from initial GOR, while isotropic case starts to increase and then decrease. This is the reason why in the **Figures 1-3**, there is nothing happening in the first few days of production.

The Anisotropic of the stress field is not to be a large consideration in the GOR forecasting past the first week of production. This doesn't mean that studying the σ_{hmin} is not important, it is possible that impact of the σ_{hmin} is not in the confining stress in terms of Gangi's permeability model but how it affects the initial propagation of the fracture during the hydraulic fracturing process. Overall it seems that just considering the anisotropic effects of the stress field on the permeability reduction during production is not significant.

4. CONCLUSIONS

The producing gas-oil-ratio of the unconventional horizontal wells in shale reservoirs have starkly different behavior compared to conventional reservoir systems. Conventional, tight and ultra-tight homogenous reservoirs where modeled with high conductivity fractures, and the tight/ultra-tight cases showed a flat GOR trends that lasted for extended periods of time even though the P_{wf} was below the bubble point pressure of the model oil. The reservoir simulator was modelled to test the following characteristics that affect the GOR: the pore volume compressibility; the stress dependent permeability; the anisotropic nature of the permeability between the matrix and the fracture; the dimensionless fracture conductivity; the effect of anisotropy in stress. The permeability of the system was modelled using the Gangi permeability equation, where the matrix permeability is assumed to be a function of closure of the cracks from stress and the hydraulic fractures as a function of the proppants resistance to stress.

On the most fundamental level, the reason the GOR is flat for an extended period of time in these horizontal shale wells is from the nature of the low matrix permeability interacting with the hydraulic fractures. In a reservoir flow model of a tight rock with hydraulic fractures, there will be a long period of a plateau. All the extra effects of shale listed by the literature: PVT suppression, dynamic permeability, capillary effects, etc., are not required for there to be a transient period of flat GOR. The flat period is caused by the nature of linear flow, where there is a large section of pressure propagation that is it at P_{wf} that sharply changes to initial pressure when the radius of investigation ends. Everything else is a secondary parameter.

The stress dependence of the permeability can lead to significant changes in GOR. The isotropic trials for the tight rock model, that has a matrix permeability of 50 micro-Darcy, were run with a constant multiplier showed that the lower the multiplier the flatter the trend, and if

the multiplier got low enough then there will be enough closure to reduce the plateau level of the GOR. The dynamic isotropic trials showed that a reservoir that's permeability follows Gangi's permeability model will have large reduction in the GOR in comparison to the same reservoir model but with a constant permeability. In the constant isotropic trials for the ultra-tight rock, that has a matrix permeability of 500 nano Darcy, the stress dependency was not significant in reducing the GOR.

When the fractures of a well are finite conductivity, then the biggest secondary factor for the GOR trend is the stress dependency in the fractures. The Anisotropy trials done on the permeability show that stress permeability effects on GOR are primarily on the fracture permeability compared to the matrix permeability stress effects. It's the fracture closure stress that is the driving force for the GOR reduction caused by the stress dependent permeability. The fractures closing is preventing gas from releasing in the system. The fracture mechanics are critical to understand.

For infinite conductivity fractures, the most important secondary parameter affecting the GOR is the pore compressibility. In shale systems, the pore compressibility can range from $1.8E^{-4}$ down to $2.0E^{-6}$ psi^{-1}. The higher compressibility range causes a pore volume reduction that prevents gas escaping from the oil. The lack of gas evolving from the oil leads to a reduction in the gas saturation. The change in compressibility leads to a change in the plateau level of the GOR, where a compressibility of $2E^{-5}$ has a GOR that is 20% less than the same reservoir with a compressibility $1E^{-5}$. The plateau level changes, but also the trend becomes flatter as well. The stress in and near the fracture will lead to the peak gas saturation to reduce, which is an indication that exsolution is forming in the hydraulic fractures. So, the closing of the fractures is causing gas to go back into the oil which is why the gas saturation is lower in

the high compressibility cases. This compressibility effect happened in both the tight rock and the ultra-tight rock model. The porosity of the system was found to have an effect on how long it takes to get to the next stage of production, but it doesn't change the GOR when that stage of production is met.

The anisotropy of confining pressure did not have that large of an impact on the GOR, and the effects that it did have were primarily in early stages of production where the pressure drop is primarily near the fracture. The Anisotropic trial showed why the GOR is flat in the early period as opposed to the isotropic trial that had a increasing period and then decreasing period in the first week.

The dimensionless fracture conductivity trials showed that when the fracture permeability is high enough to be considered infinite, when it is greater than 30, the GOR does not change. The GOR still had the same general trend when the F_{cD} was 3 and higher. If the GOR trend shows a flat plateau for an extended period, then this would mean the fracture permeability is at least high enough to be around 500 milli Darcy. When the fracture permeability gets low enough, the fracture starts to fail, and the gas mobility is reduced more compared to the oil mobility.

REFERENCES

Andersen, M.A. 1988. Predicting Reservoir-Condition PV Compressibility from Hydrostatic-Stress Laboratory Data. *SPE Res Eng* **3** (03): 1078–1082. SPE-14213-PA. https://doi.org/10.2118/14213-PA

Ankush, S., Zobackm, M.D. 2022. Predicting variations of the least principal stress with depth: Application to unconventional oil and gas reservoirs using a log-based viscoelastic stress relaxation model. *SEG J.* **87** (03). MR105-MR116. https://doi.org/10.1190/geo2021-0429.1

Didar, B.R., Akkutlu, I.Y. 2013. Pore-Size Dependence of Fluid Phase Behavior and Properties in Organic-Rich Shale Reservoirs. Paper presented at the SPE International Symposium on Oilfield Chemistry, The Woodlands, Texas, USA, 8-10 April. SPE-164099-MS. https://doi.org/10.2118/164099-MS

Gangi, A.F. 1978. Variation of Whole and Fractured Porous Rock Permeability with Confining Pressure. International J. *Rock Mechanics and Mining Sciences and Geomechanics Abstracts.* **15** (5): 249-257. https://doi.org/10.1016/0148-9062(78)90957-9

Honarpour, M.M., Nagarajan, N.R., Orangi, A., Arasteh, F., Yao, Z. 2012. Characterization of Critical Fluid, Rock, and Rock-Fluid Properties-Impact on Reservoir Performance of Liquid-rich Shales. Paper presented at the SPE Annual Technical Conference and Exhibition, San Antonio, Texas, USA, 8-10 October. SPE-158042-MS. https://doi.org/10.2118/158042-MS

Hough, E. V. and McClurg, T. 2011. Impact of Geological Variation and Completion Type in the US Bakken Oil Shale Play Using Decline Curve Analysis and Transient Flow Character. AAPG Search and Discovery Article No. 40857, adapted from oral presentation given at the AAPG International Conference and Exhibition, Milan, Italy, 23–26 October.

Jones , R. Steven. 2017. "Producing-Gas/Oil-Ratio Behavior of Multi-fractured Horizontal Wells in Tight Oil Reservoirs." *SPE Res Eval & Eng* **20** (03): 589–601. SPE-184397-PA. https://doi.org/10.2118/184397-PA

Khoshghadam, M., Khanal, A., Yu, C., Rabinejadganji, N., and Lee, W. J. 2017. Producing Gas-Oil Ratio Behavior of Unconventional Volatile-Oil Reservoirs, and Its Application in Production Diagnostics and Decline Curve Analysis. Paper presented at the SPE/AAPG/SEG Unconventional Resources Technology Conference, Austin, Texas, USA, 24-26 July. URTEC-2670925-MS. https://doi.org/10.15530/URTEC-2017-2670925

Khoshghadam, M., Khanal, A., and Lee, W. 2015. Numerical Study of Impact of Nano-Pores on Gas-Oil Ratio and Production Mechanisms in Liquid-Rich Shale Oil Reservoirs. Paper presented at the SPE/AAPG/SEG Unconventional Resources Technology Conference, San Antonio, Texas, USA, 20-22 July. URTEC-2154191-MS. https://doi.org/10.15530/URTEC-2015-2154191

Kim, B.Y., Akkutlu, I.Y., Martysevich, V., et al. 2019. Monolayer Microproppant-Placement Quality Using Split-Core-Plug Permeability Measurements Under Stress. *SPE J.* **24** (04): 1790–1808. SPE-189832-PA. https://doi.org/10.2118/189832-PA

Mahomad, B. 2014. *Evaluation of shale compressibility from NMR and MICP measurements*. MS Thesis. University of Oklahoma, Norman, Oklahoma

Makinde, I. 2017. A Simulation Study of the Factors that Impact Gas-Oil Ratio (GOR) Behavior in Liquid-Rich Shale (LRS) Reservoirs. *Global Journal of Research In Engineering* **17** (2): 27-43. http://doi.org/10.1051/e3sconf/202124802027

Oppert, S., Carley, S. 2021. Reservoir insights unlocked by multidisciplinary integration. Paper presented at the EAGE GeoTech 2021 Third EAGE Workshop on Practical Reservoir Monitoring, Virtual, 1-4 March. https://doi.org/10.3997/2214-4609.202131065

Pradhan, Y. 2020. Observed Gas-Oil Ratio Trends in Liquids Rich Shale Reservoirs. Paper presented at the SPE/AAPG/SEG Unconventional Resources Technology Conference, Virtual, 20 July. URTEC-2020-3229-MS. https://doi.org/10.15530/urtec-2020-3229

Tran, T., Sinurat, P. D. and Wattenbarger, B. A. 2011. Production Characteristics of the Bakken Shale Oil. Presented at the SPE Annual Technical Conference and Exhibition, Denver, 30 October–2 November. SPE-145684-MS. https://doi.org/10.2118/145684-MS.

Walsh, Mark P. and Lake, Larry W. 2003. Section 12-6, Solution-Gas Drive Reservoirs. In A Generalized Approach to Primary Hydrocarbon Recovery, first edition. Amsterdam, The Netherlands: Elsevier.

Wasaki, A., Akkutlu, I.Y. 2015. Permeability of Organic-Rich Shale. *SPE J.* **20** (06): 1384–1396. SPE-170830-PA. https://doi.org/10.2118/170830-PA

Whitson, C. H., Lei, G. and Cheng, N. 2014. Liquid-Rich Shale Versus Conventional Depletion Performance. Presented at the SPE/EAGE European Unconventional Resources Conference and Exhibition, Vienna, Austria, 25–27 February. SPE-167788-MS. https://doi.org/10.2118/ 167788-MS.

Whitson, C. H. and Sunjerga, S. 2012. PVT in Liquid-Rich Shale Reservoirs. Presented at the SPE Annual Technical Conference and Exhibition, San Antonio, Texas, 8–10 October. SPE-155499-MS. https:// doi.org/10.2118/155499-MS.

Zoback, M., Kohli, A. 2019. Strength and Ductility. In *Unconventional Reservoir Geomechanics: Shale Gas, Tight Oil, and Induced Seismicity* (pp. 65-90). Cambridge: Cambridge University Press. doi:10.1017/9781316091869.004

APPENDIX A

Table 9. Eclipse Trials

Trial #	Trial description
1	Prototypical conventional model with matrix permeability of 50 mD
2	Base Case
3	Constant permeability trials, transmissibility multiplier .54
4	Constant permeability trials, transmissibility multiplier .31
5	Constant permeability trials, transmissibility multiplier .17
6	Constant permeability trials, transmissibility multiplier .14
7	Constant permeability trials, transmissibility multiplier .09
8	Constant permeability trials, transmissibility multiplier .08
9	Constant permeability trials, transmissibility multiplier .04
10	Constant permeability trials, transmissibility multiplier .03
11	Constant permeability trials, transmissibility multiplier .01
12	Dynamic permeability trials, m = .3, pressure max = 13500 σ_{ob}= 9000
13	Dynamic permeability trials, m = .3, pressure max = 13500 σ_{ob} = 10000
14	Dynamic permeability trials, m = .3, pressure max = 13500 σ_{ob} = 11000
15	Dynamic permeability trials, m = .3, pressure max = 13500 σ_{ob} = 13000
16	Dynamic permeability trials, m = .6, pressure max = 13500 σ_{ob} = 9000
17	Dynamic permeability trials, m = .6, pressure max = 13500 σ_{ob} = 10000
18	Dynamic permeability trials, m = .6, pressure max = 13500 σ_{ob} = 11000
19	Dynamic permeability trials, m = .6, pressure max = 13500 σ_{ob} = 13000
20	Dynamic permeability trials, m = .9, pressure max = 13500 σ_{ob} = 9000
21	Dynamic permeability trials, m = .9, pressure max = 13500 σ_{ob} = 10000
22	Dynamic permeability trials, m = .9, pressure max = 13500 σ_{ob} = 11000
23	Dynamic permeability trials, m = .9, pressure max = 13500 σ_{ob} = 13000
24	Porosity trials, φ = .12
25	Porosity trials, φ = .1
26	Porosity trials, φ = .07
27	Porosity trials, φ = .02
28	compressibility trials. Pore compressibility = 1E-5
29	compressibility trials. Pore compressibility = 2E-5
30	compressibility trials. Pore compressibility = 5E-5
31	compressibility trials. Pore compressibility = 1E-4
32	dimensionless fracture conductivity trials, FCD = 381
33	dimensionless fracture conductivity trials, FCD = 38.1
34	dimensionless fracture conductivity trials, FCD = 3.81

Table 10. Eclipse Trials

Trial #	Trial description
35	dimensionless fracture conductivity trials, FCD = .381
36	Ultratight reservoir case, matrix permeability =.0005 mD
37	Ultratight reservoir case, compressibility trials. Pore compressibility = 1E-5
38	Ultratight reservoir case, compressibility trials. Pore compressibility = 2E-5
39	Ultratight reservoir case, compressibility trials. Pore compressibility = 5E-5
40	Ultratight reservoir case, compressibility trials. Pore compressibility = 1E-4
41	Ultratight reservoir case, compressibility trials. Pore compressibility = 1E-5, porosity = .08
42	Ultratight reservoir case, compressibility trials. Pore compressibility = 1E-5, porosity = .04
43	Ultratight reservoir case, compressibility trials. Pore compressibility = 2E-5, porosity = .08
44	Ultratight reservoir case, compressibility trials. Pore compressibility = 2E-5, porosity = .04
45	Ultratight reservoir case, compressibility trials. Pore compressibility = 5E-5, porosity = .08
46	Ultratight reservoir case, compressibility trials. Pore compressibility = 5E-5, porosity = .04
47	Ultratight reservoir case, compressibility trials. Pore compressibility = 1E-6, porosity = .08
48	Ultratight reservoir case, compressibility trials. Pore compressibility = 1E-6, porosity = .04
49	Ultratight reservoir case, Constant permeability trials, transmissibility multiplier .54
50	Ultratight reservoir case, Constant permeability trials, transmissibility multiplier .17
51	Ultratight reservoir case, Constant permeability trials, transmissibility multiplier .09
52	Ultratight reservoir case, Constant permeability trials, transmissibility multiplier .08
53	Ultratight reservoir case, Constant permeability trials, transmissibility multiplier .03
54	Ultratight reservoir case, Constant permeability trials, transmissibility multiplier .01
35	dimensionless fracture conductivity trials, FCD = .381
36	Ultratight reservoir case, matrix permeability =.0005 mD
37	Ultratight reservoir case, compressibility trials. Pore compressibility = 1E-5
38	Ultratight reservoir case, compressibility trials. Pore compressibility = 2E-5
39	Ultratight reservoir case, compressibility trials. Pore compressibility = 5E-5
40	Ultratight reservoir case, compressibility trials. Pore compressibility = 1E-4
41	Ultratight reservoir case, compressibility trials. Pore compressibility = 1E-5, porosity = .08
42	Ultratight reservoir case, compressibility trials. Pore compressibility = 1E-5, porosity = .04
43	Ultratight reservoir case, compressibility trials. Pore compressibility = 2E-5, porosity = .08
44	Ultratight reservoir case, compressibility trials. Pore compressibility = 2E-5, porosity = .04
45	Ultratight reservoir case, compressibility trials. Pore compressibility = 5E-5, porosity = .08
46	Ultratight reservoir case, compressibility trials. Pore compressibility = 5E-5, porosity = .04
47	Ultratight reservoir case, compressibility trials. Pore compressibility = 1E-6, porosity = .08
48	Ultratight reservoir case, compressibility trials. Pore compressibility = 1E-6, porosity = .04
49	Ultratight reservoir case, Constant permeability trials, transmissibility multiplier .54
50	Ultratight reservoir case, Constant permeability trials, transmissibility multiplier .17
51	Ultratight reservoir case, Constant permeability trials, transmissibility multiplier .09
52	Ultratight reservoir case, Constant permeability trials, transmissibility multiplier .08
53	Ultratight reservoir case, Constant permeability trials, transmissibility multiplier .03
54	Ultratight reservoir case, Constant permeability trials, transmissibility multiplier .01

Table 11. NaSh Trials

Trial #	Trial description
1	Pore compressibility trials: matrix and fracture compressibility = 3E-5
2	Pore compressibility trials: matrix and fracture compressibility = 6E-5
3	Pore compressibility trials: matrix and fracture compressibility = 1E-4
4	Pore compressibility trials: matrix and fracture compressibility = 1E-5
5	Pore compressibility trials: matrix and fracture compressibility = 1E-6
6	Pore compressibility trials: matrix compressibility = 6E-5 and fracture compressibility = 3E-5
7	Pore compressibility trials: matrix compressibility = 3E-5 and fracture compressibility = 6E-5
8	Pore compressibility trials: matrix compressibility = 1E-5 and fracture compressibility = 1E-4
9	Pore compressibility trials: matrix compressibility = 1E-4 and fracture compressibility = 1E-5
10	over burden trial, isotropic case, m = .3, porosity =.072, P1 = 27827, σ_{ob} = 15000
11	over burden trial, isotropic case, m = .3, porosity =.072, P1 = 27827, σ_{ob} = 20000
12	anisotropic trial, dynamic matrix and fracture
13	anisotropic trial, dynamic matrix and constant fracture
14	anisotropic trial, constant matrix and dynamic fracture
15	anisotropic trial, constant matrix and constant fracture